

**SLOVAK UNIVERSITY OF TECHNOLOGY IN
BRATISLAVA**
**FACULTY OF ELECTRICAL ENGINEERING
AND INFORMATION TECHNOLOGY**

Evidence number: FEI-104400-76956



**Three-dimensional electromagnetic modelling of
practical superconductors for power applications**

Dissertation thesis

Study Programme: Physical Engineering

Field of Study: 5.2.48 Physical Engineering

External Supervising Institution: Institute of Electrical
Engineering,

Slovak Academy of Sciences

Thesis Supervisor: Mgr. Enric Pardo, PhD

BRATISLAVA 2018

Ing. Milan Kapolka

Contents

1	Introduction	13
2	Background	15
2.1	Superconducting power applications	16
2.2	Type I and type II superconductors	17
2.3	Vortices and vortex pinning	18
2.4	Low- and high- temperature superconductors	19
2.5	$\mathbf{E}(\mathbf{J})$ relations	21
2.6	Critical State Model (CSM)	22
2.7	$\mathbf{E}(\mathbf{J})$ relation for anisotropic "force-free" effects	25
2.8	Applied vector potential	27
2.9	Eddy current problem	29
2.9.1	$\mathbf{A}-\phi-\mathbf{J}$ formulation	30
2.9.2	$\mathbf{T}-\psi$ formulation	31
2.9.3	\mathbf{H} formulation	32
2.9.4	Variational principles	33
3	Model and Numerical method	35
3.1	Mathematical model	36
3.2	Discretization	40
3.3	Thin film approximation and stacks of many tapes	42
3.4	Current lines	43
3.5	Minimization	44
3.5.1	Evaluation of \mathbf{J} and \mathbf{A}	44
3.5.2	Minimization algorithm	45
3.6	Sectors	46
3.7	Symmetry	49
3.8	Parallel programming	51
3.8.1	Structure of the code	51
3.8.2	Parallel programming in one computer by OpenMP	53
3.8.3	Parallel programming on a cluster by BoostMPI	54
3.8.4	Computation time	57
3.9	Elongated cells	59

4	Experimental method and samples	61
4.1	Sample of two tapes joined by normal metal for coupling effects measurements	62
4.2	Calibration free method for AC loss measurement	62
4.3	Cube sample for demagnetization by cross-field	63
4.4	Measurement of bulk demagnetization by cross-fields	64
5	Model tests and verification	69
5.1	Comparison of thin film model with analytical formulas.	69
5.2	Finite-length superconducting thin film with constant J_c	73
5.3	Finite superconducting thin film with $J_c(B)$ dependence	75
5.4	Coupling effects in multi-filamentary tapes	77
5.4.1	Coupling effects in two-tape conductor compared with FEM model	77
5.4.2	Coupling effects in two-filament tape and measurements	79
6	Results and discussion	83
6.1	Coupling loss in multi-filament tape	84
6.2	Magnetization of isotropic rectangular prisms	86
6.2.1	3D Magnetization currents with constant J_c	88
6.2.2	3D Magnetization currents with $J_c(B)$ dependence	97
6.2.3	Magnetization loops and penetration field of rectangular prisms with constant J_c	99
6.2.4	Benchmark of superconducting bulk with perpendicular applied magnetic field.	101
6.3	Magnetization of stacks of tapes and bulks in tilted applied field	103
6.3.1	Screening currents	103
6.3.2	AC loss, magnetization loops, and comparison with other methods	104
6.4	Cross-field demagnetization of cubes.	106
6.4.1	Modelling of cross-field demagnetization	108
6.4.2	Experiments and comparison to modelling	112
6.5	Anisotropic force-free effects	114
6.5.1	Finite superconducting thin film with anisotropic $\mathbf{E}(\mathbf{J})$ relation	116
6.5.2	Prism with various thicknesses and anisotropic $\mathbf{E}(\mathbf{J})$ relation	121
7	Conclusion	133
8	Appendix	137
8.1	Average vector potential of the self-point interaction.	137
8.2	Euler equations of the functional	139

CONTENTS

5

9 Parameters of the input file

143

Acknowledgments

I would like to express my gratitude to my supervisor Mgr. Enric Pardo, PhD. For leading, help, comments and remarks for this Thesis as well as during the whole PhD study. I also thank Jan Srpcic, Difan Zhou, Mark Ainslie, Anthony Dennis, Francesco Grilli, Victor Zermeno, Shengnan Zou, Antonio Morandi and Leonid Prigozhin for very important and constructive comments and helpful cooperation.

The Dissertation Thesis was financially supported by the use of computing resources provided by the project SIVVP, ITMS 26230120002 supported by the Research & Development Operational Programme funded by the ERDF, the financial support of the Grant Agency of the Ministry of Education of the Slovak Republic and the Slovak Academy of Sciences (VEGA) under contract No. 2/0126/15. and No.2/0097/18, and the support by the Slovak Research and Development Agency under the contract No. APVV-14-0438.

Abstrakt

Vývoj vysokoteplotných supravodičov umožnil nástup supravodivých výkonových aplikácií ako sú generátory, motory, transformátory a výkonové prenosové vedenia. Supravodiče umožňujú mnohonásobné zvýšenie prúdovej hustoty a generovanie magnetického poľa v porovnaní s normálnymi vodičmi ako je meď a hliník a preto sú supravodiče ich jediná alternatíva. Pre mnoho výkonových aplikácií ako sú "large-bore" magnety sú požadované vysoké výkony, viac než 10 MW pre veterné turbíny a viac než 1MW pre letecké pohonné motory. Keďže chladiaci systém musí chladiť supravodiče medzi teplotami kvapalného hélia a dusíka je jeho účinnosť nízka. Kryogénny systém spotrebúva 10 až 100 krát viac elektrickej energie ako je odvod tepla zo supravodivého materiálu. Supravodiče v striedavom (AC) režime generujú tepelné straty, preto úroveň AC strát je dôležitý parameter vo výkonných zariadeniach. AC straty závisia na mnohých faktoroch ako sú prúdové profily, magnetické polia, geometria supravodivého vnutia a magnetický materiál.

Počítačové modelovanie je dôležité, aby odhalilo všetky vlastnosti supravodivých zariadení, materiálové vlastnosti a ich optimalizáciu. Supravodiče sú vysoko nelineárne materiály komplikujúce modelovanie. Modelovací nástroj musí byť rýchly a presný, aby predvídal všetky efekty. 2D modely využívajú symetriu na zníženie stupňov voľnosti v prierezovej rovine. Avšak práve preto nemôžu zahrnúť efekty konečných rozmerov. Z tohto dôvodu sú potrebné plne 3-rozmerné (3D) modelovacie metódy, ktoré zvládnu obrovský počet elementov v 3D mriežke. Naša 3D modelovacia metóda môže modelovať ľubovoľnú závislosť elektrického poľa \mathbf{E} na prúdovej hustote \mathbf{J} , $\mathbf{E}(\mathbf{J})$, čo je obrovská výhoda.

Táto práca je zameraná na vývoj plne 3D modelovacieho nástroja. Modelovacia metóda je založená na novej variačnej metóde nazvanej "Minimum Electro Magnetic Entropy Production in 3D", MEMEP 3D, ktorá používa efektívnu magnetizáciu \mathbf{T} ako neznámu veličinu. Modelovací nástroj je naprogramovaný v jazyku C++ so štruktúrou paralelného programovania. Výpočtová metóda je overená 2D analytickými predpovedami a ďalšími 3D modelovacími metódami. Modelovacie prípady sú zamerané na tenký film a objemovú vzorku.

Efektivita paralelného programovania je 80% po otestovaní na počítačovom klastri. Výsledky modelovania na jednoduchých tvaroch potvrdili 2D an-

alytické predpovede prúdových profilov a hysteréznych slučiek. MEMEP 3D dosiahol len 3% odchýlku predpovedí AC strát na dvoch spájkovaných supravodivých páskach. Pomocou metódy sme našli 3D prúdové cesty v objemovej vzorke a objavili nenulovú z zložku prúdovej hustoty pri nesaturovanom stave. 3D krížový demagnetizačný proces predpovedal asymetriu zachyteného poľa, ktorú potvrdilo meranie. Možnosť ľubovoľnej $\mathbf{E}(\mathbf{J})$ závislosti dovolila študovať "force-free" efekty v tenkých filmoch a hranoloch pri natočenom externom magnetickom poli. Modelovanie tak odhalilo všetky efekty konečných rozmerov supravodiča a "force-free" efekty.

Celkovo, MEMEP 3D modelovanie potvrdilo užitočnosť celej metódy s vysokou účinnosťou a krátkym výpočtovým časom. Variačná metóda zvládla veľmi vysoký počet stupňov volnosti s overením až do 1 milióna a odhalila nové neznáme supravodivé efekty.

Abstract

The development of high temperature superconductors opens the road for superconducting power applications such as generators, motors, transformers and power transmission lines. Superconductors allow to drastically increase the current density and generated magnetic field compared to normal conductors like copper or aluminium, and hence they became the only alternative to them for many applications like large-bore magnets, >10 MW wind generators and >1MW airplane propulsion motors. Since the cryogenic system needs to cool down the superconductor between liquified helium and nitrogen temperature their efficiency is low. The cryogenic system consumes 10-100 times more energy as it removes heat from the superconducting material. Superconductors dissipate energy in AC regime, and hence dissipation of the entire power device is an important feature. The dissipation depends on many factors, such as current distribution, magnetic fields, geometry of the superconducting winding, magnetic materials and others.

Computer modelling predictions are necessary, in order to reveal all features of superconducting devices or the material properties and optimize them. Superconductors are highly non-linear materials, which complicates modelling. The modelling tool needs to be fast and accurate, in order to predict all effects. 2D models use symmetry, and thence they reduce the degrees of freedom to the cross-sectional planes. However, they cannot include finite size effects. Therefore, full 3D models are needed, which can handle a huge number of elements in the complete 3D mesh. Our 3D modelling method can model any relation between the electric field \mathbf{E} and current density \mathbf{J} , $\mathbf{E}(\mathbf{J})$, which is a big advantage.

This thesis aims to develop a full 3D modelling tool. The modelling method is based on a novel variational method called Minimum Electro Magnetic Entropy Production MEMEP 3D that uses the effective magnetization \mathbf{T} as state variable. The modelling tool is written in C++ programming language with parallel computing structure. The modelling method is verified by 2D analytical predictions and other 3D modelling methods. Modelling cases are focused on thin film and bulk samples.

The parallel computing efficiency is checked by a computer cluster and reached 80% efficiency. The modelling results on simple samples confirmed 2D analytical predictions of current profiles and hysteresis loops. The MEMEP

3D method presents only 3% error of AC loss prediction of two soldered superconducting tapes. The method finds 3D current paths of a cubic sample and reveals non-zero J_z component at non-saturated state. The full 3D cross-field demagnetization process predicts asymmetry of the trapped field, which measurements confirmed. The possibility of including any $\mathbf{E}(\mathbf{J})$ relation allows to study force-free effects in thin films and prisms with tilted applied field angles, which reveals all finite size and force-free effects.

In conclusion, MEMEP 3D proved usefulness of the entire method with high accuracy and low calculation time of the results. The variational method can handle huge number of degrees of freedom, checked up to 1 million, and reveals new unknown superconducting effects.

Chapter 1

Introduction

The continuous improvement of Low and High Temperature Superconductors (LTS and HTS) by increasing critical current density J_c for lower costs opens the room for superconducting power applications such as generators, motors, transformers, wind-turbines or power transmission lines. The superconductor in power applications needs to be cooled down below a certain critical temperature T_c , and hence the cryogenic system has to be well optimized. Superconductors present AC loss in AC regime, and thence they dissipate energy. Even small dissipation of energy at helium or nitrogen temperature is problematic, since cryocooling units are inefficient at such temperatures and can cause malfunction of the entire power device. In addition, the magnetization response is useful for material characterization.

Computer modelling can predict the current distribution in superconductors and AC loss. 2D cross-sectional models based on analytical solutions of the Critical State Model CSM or numerical calculations reached maturity. There are many models based on integral methods [1–7], Finite Element Method [8–10], variational method [11–21] or circuit method [22]. However, analytical solutions can predict current profiles only in simple samples without combinations of transport current and applied magnetic fields. Cross-sectional models cannot include finite size effects, which are important in power devices of finite size. Therefore, full 3D numerical models are required.

3D models include all finite size effects but 3D mesh requires a huge number of degrees of freedom. Therefore, the computation time needs to be low with accurate results. There are many 3D numerical methods like variational methods in H formulation [23–25] or finite element method by H formulation [26–29], \mathbf{A} - ϕ vector and scalar potential [30–32] and \mathbf{T} - Ω vector and scalar current potential [33] or cohomology [29].

This thesis is focused on the development of a novel 3D modelling tool based on an original variational method. The method is called the Minimum Electro Magnetic Entropy Production MEMEP 3D, which is suitable

for tasks of huge number of elements. The MEMEP 3D model is verified by analytical predictions of 2D cross-sectional models and comparison to measurements. The modelling results are focused on the study of thin films and bulk samples, regarding both fundamental and application research. The fundamental study is about the "force-free" effects [34, 35], since MEMEP 3D can include anisotropic power law for the case of parallel current density and local magnetic field. We also model isotropic rectangular prisms in applied magnetic fields, obtaining an unexpected behavior of the 3D current lines. The application study is of cross-field demagnetization for bulk superconductor magnets [36]. The estimation of AC loss in thin films is important for characterization of tapes.

Chapter 2

Background

The discovery of superconductivity by Kamerlingh Onnes, who liquified helium for the first time and reached temperatures of around 3K, leads to the beginning of a new research field. Later in decades, there have been investigated many superconducting materials, being the most interesting for applications NbTi, NbSn, MgB₂, YBCO, Bi2232 and Bi2212. Superconductors have many advantages compared to usual conductors, and hence superconductors are essential for magnets and superconducting power applications started to be promising for commercial use.

The large-bore magnets can only be made by superconductors. Most magnets are made of Low-Temperature superconductors like NbTi and Nb₃Sn, which need liquid helium temperatures to operate (4.2 K) but high-field magnets, generating more than 20 T, require High-Temperature superconductors like REBCO. The critical temperature of several type I and type II superconductors are in table 2.1. Nowadays, commercial tapes of type II and High-Temperature superconductors (with critical temperature above 77 K) are more promising for power applications like generators (such as wind turbines), motors, transformers, power transmission lines and fault-current limiters. However, type II superconductors dissipate energy in AC regime. The cryogenic system is less complex with better efficiency at nitrogen temperature (77 K) than liquid helium temperature (4.2 K).

In order to improve and explain superconductivity, many theories appeared. Microscopic theories explained the origin of superconducting phenomena. The BCS theory postulated that the electrons form Cooper pairs that condensate into the superconducting state, while the Ginzburg-Landau theory predicted type II superconductors and vortices [37]. The microscopic theories cannot explain phenomenological effects in real size superconductors, since the calculation time of such scale is not feasible. Therefore, macroscopic theories with many assumptions to simplify the calculation are required like the Critical State Model. Analytical predictions are not always possible to find, and hence numerical methods play a significant role to model super-

Type I	Hg	Pb	In	Mo	Al	Ga	Ta
T_c [K]	4.2	7.2	3.4	0.92	1.2	1.1	4.48
Type II	NbTi	Nb ₃ Sn	MgB ₂	YBCO	Bi2232	Bi2212	HBCCO
T_c [K]	9	18	39	90	110	85	134

Table 2.1: Critical temperatures of several type I and type II superconducting materials.

conducting power applications.

There are many numerical formulations, which have been proposed like Finite Element Methods. The variational method is another approach of numerical method. The 2D variational method showed accuracy and short calculation time. However, it needs improvement to the 3D case.

2.1 Superconducting power applications

Superconductors are an alternative to normal conductors with great potential for power applications. The big advantage of superconductors compared to copper is that they enable high current density. Nowadays, tapes can carry currents up to around 550 A for a tape width of 10 mm [38]. The width is in the range of 4-12 mm and thickness from 1 to 1.6 μm . High current density in windings can induce magnetic fields of several tesla [39–42], which is difficult to reach by copper conductor. However, the world record of the highest magnetic field of 45 T is by hybrid magnets (superconducting and resistive) with the copper winding cooled by pressurized water and power consumption around 30 MW [43].

Another aspect of the high current density is the possibility of reducing magnetic iron parts in power devices like motors and generators, and hence reducing the weight of the power device. The weight of the power device is crucial in mobile applications like ship [44, 45] or aircraft propulsion [46, 47], as well as for superconducting wind turbines for offshore applications [48–50], since they have to be as light as possible in order to reduce cost of the tower in the sea. Another area where weight is important are space applications like passive shielding or propulsion, where any additional weight highly increases the cost to bring any spacecraft to the Earth’s orbit.

Superconducting power applications reduce the dimensions of the devices. In order to increase the power in the power network in big metropolises, smaller power devices are necessary. Superconducting transformers [51–54] can increase the reliability and safety of the electric network and include fault current limiters [55–59], either as part of the transformers or as an independent device. Superconducting power lines can reduce the voltage by increasing the transport current. This can simplifying the power network by

reducing the number of the step-down transformers. Low-voltage cables can be placed with low distance between them in corridors, and hence increase power-line density even higher. Superconducting cables are also promising for High Voltage DC lines, enabling lower dissipation and higher power. There are many studies of power line cables, such as those in [60, 61].

Magnet applications like commercial Magnetic Resonance Imaging MRI magnets [62], particle accelerators like the LHC in CERN [63], or tokomaks for plasma and fusion research like ITER [64] put many requirements on superconducting tapes producers. The tapes have to have long length of several 100 m up to km with homogeneous critical current density along the tape and low cost, which for 2G HTS tapes it is in present around 200 EUR per kAm at self-field and 77 K. At present, there are many producers of 2G HTS tape [65–71].

The disadvantage of superconductors is that they need to be cooled below certain critical temperature T_c (section 2.4) to become superconducting, and even lower temperature to have useful properties. Low Temperature Superconductors (LTS) usually operate at liquefied helium temperature 4.2 K, while High Temperature Superconductors (HTS) can operate up to 77 K by liquid nitrogen. Middle Temperature Superconductors like MgB_2 operate up to 20 K. The cost of liquefied nitrogen is 10 times lower than liquefied helium, and hence HTS superconductors open the door for commercial use of superconducting power applications. Cryocoolers can cool down superconductors to any temperature down to 4 K, but the efficiency at such temperature is very low. In order to remove 1 W of heat at 70 K, cryocoolers need around 20 W of electricity. The efficiency at 4 K is even lower, for 1 W of heat cryocoolers have 100 W of electricity consumption. Therefore, the AC loss (section 5.4.2) have to be as low as possible. Superconducting power applications are promising for the near future but they still are complex systems.

2.2 Type I and type II superconductors

The first discovered type of superconductors (type I) has to accomplish three conditions, in order to reach the superconducting state. The superconductor needs to carry transport current or shielding current below a depairing current density J_d , the material has to be cooled down below certain critical temperature T_c , and the applied magnetic field needs to be below the critical current density H_c . Only under the previous three conditions, type I superconducting materials present superconductivity, as it is shown on figure 2.1(a). There are two signs of perfect superconductivity. The superconductor is a perfect diamagnetic with $\mu_r \approx -1$, and hence it shields completely any applied magnetic field below H_c . The Meissner shielding current penetrates only a few μm into the sample with London penetration depth λ . Measurements show that these Meissner currents are permanent. A super-

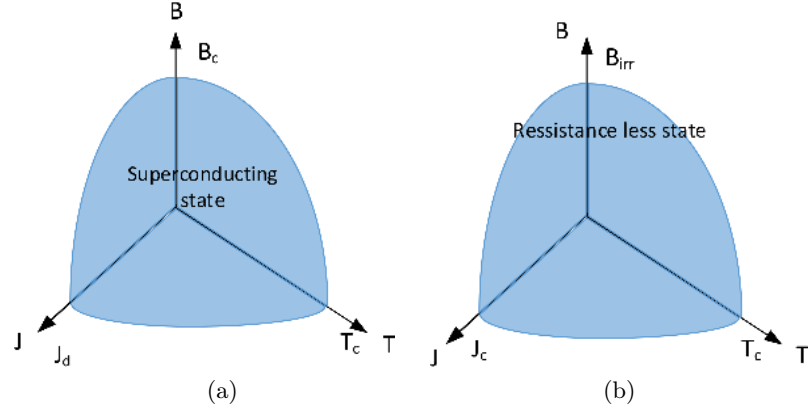


Figure 2.1: (a) Type I superconducting state conditions of depairing current density J_d , critical temperature T_c and critical magnetic field B_c . (b) Type II resistance-less conditions, where J_c is the critical-current density and B_{irr} is the irreversibility magnetic field.

conducting ring with induced shielding current shows no decrease of current density at least for 10^5 years [37].

Superconductors are divided among type I and type II superconductors. Another type of superconductors, type II superconductors, have two limits of magnetic field H_{c1} and H_{c2} . The applied field below H_{c1} induces Meissner screening current in λ penetration depth and the superconductors behave like type I. Applied fields H_a of value $H_{c1} < H_a < H_{c2}$ cause penetration of vortices into the superconductor. Vortices are predicted by Ginzburg-Landau theory inspired by quantum physics. Vortices enable to flow magnetic flux along the normal vortex zone, and hence type II superconductors are still superconducting even under high magnetic fields. The theoretical value of the upper limit of H_{c2} is around 120 T (for REBCO), which is far beyond H_c of typical the type I superconductors, being around 80 mT for Pb. An applied field higher than H_{c2} kills the Cooper pairs and the material loses superconductivity.

2.3 Vortices and vortex pinning

Superconducting vortices in superconductors are explained by the microscopic Ginzburg-Landau theory. The vortex structure consists mainly on a tube with central non-superconducting zone and superconducting current flowing around it. The applied or self magnetic field penetrates through the normal zone in the vortex with value of one fluxon $\theta_0 = hc/2e$, where h is Planck's constant, c is the speed of the light and e is the charge of the electron. The vortex line is parallel with the induced magnetic flux.

In the case when $H_a > H_{c1}$, where H_a is the applied field and H_{c1} is the

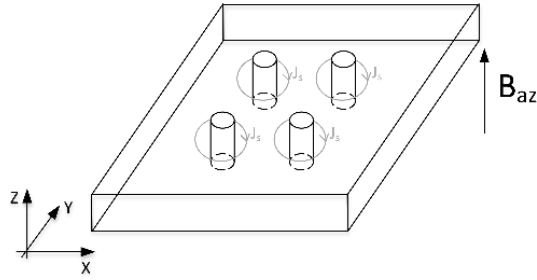


Figure 2.2: Vortices with normal zone of a tube structure with radius $r \approx \xi$, where ξ is the coherence length, and with superconducting shielding current around it.

first critical magnetic field, the vortices start to enter into the sample from the sides oriented parallel to the flux lines. The screening current density $|\mathbf{J}|$ creates a driving force on the vortices $\mathbf{F}_d = \mathbf{J} \times \mathbf{B}$, and hence the vortices start to move. The movement of the vortices induces electric field, which creates dissipation $P = \mathbf{J} \cdot \mathbf{E}$ [72].

Pinning centers with non-superconducting zone anchor or pin the vortices to a certain position, and hence pinning centers cancel dissipation. The pinning force F_p is against the driving force F_d . If the pinning force is $F_p > F_d$ the vortices do not move, and hence there is no dissipation. When the driving force is $F_d > F_p$ the vortices move and dissipate. The pinning centers improve the superconducting properties. Then, there is a big effort to increase the pinning force in tapes by various additives. The pinning centers come from voids, nano-particles, in-homogenities, and defects in crystal lattice like dislocations and twin planes.

The type II materials are still superconducting for $|\mathbf{J}| > J_c$, being J_c the critical current density. For $|\mathbf{J}| > J_c$, there is vortex flux flow, which causes AC loss and an effective resistance. The resistance-less conditions are on figure 2.1(b). However, the material is still internally superconducting. The irreversibility field, B_{irr} , is the maximum magnetic field where vortices are pinned. In LTS, and Mg_2B $B_{irr} = B_{c2}$. In type II superconductors, there is still superconductivity for $J_d > J > J_c$ and $B_{c2} > B > B_{irr}$ but vortices move for under transport current, creating an effective resistance.

2.4 Low- and high- temperature superconductors

Superconductors are classified as well according the critical temperature T_c . Low Temperature Superconductors (LTS) are metals and alloys with T_c below liquid hydrogen (20 K). Middle Temperature Superconductors (MTS) are Mg_2 or iron-based superconductors with T_c between 20 K and liquid nitrogen temperature (77 K). The last type is High Temperature Supercon-

ductors (HTS) with T_c above liquid nitrogen temperature (77 K), which are perovskites containing CuO planes.

After studying several LTS compounds, such as NbCr, NbMo, NbW, NbTa, VNb [73], in 1961 it was shown that the best two candidates were of NbTi and Nb₃Sn. Their critical temperatures are 9 K and 18 K. These LTS are the main workhorses of superconducting magnets up to date. The NbTi superconducting wires were embedded in Cu or Ni stabilization matrix. Further research on NbTi resulted in fine wires produced by Powder-in-Tube (PIT) method. The wires showed performance of $J_c = 5 \cdot 10^9$ A/m² at 5 T and 4.2 K, which were used for superconducting magnets up to 12 T. The second important LTS material, Nb₃Sn, reached high magnetic fields of 23 T at 4.2 K. The wires are prepared by the Internal Thin (IT) process and results in $J_c = 3 \cdot 10^9$ A/m² at 12 T and 4.2 K. The critical magnetic field increased to 26 T by addition of Ti. Although there have been discovered other LTS with T_c up to 25 K, NbTi and Nb₃Sn are still dominant due to their high performance at 4.2 K and ease of production.

In 1987, another important discovery was the superconducting material YBa₂Cu₃O₇ with $T_c=90$ K [74], which set the new group of High Temperature Superconductors (HTS). YBCO was prepared by the Oxide Powder in Tube (OPIT) method in bulk samples. Bednorz and Muller already found the first superconductor of the same family in 1986 [75] but it had a critical temperature of only around 35 K. Another HTS material is Bi₂Sr₂CaCu₂O₈ (Bi2212) found in 1989 with $T_c = 85$ K and up to 45 T [76]. Even higher $T_c = 110$ K reached (Bi,Pb)₂Sr₂Ca₂Cu₃O₁₀ (Bi2223), a material first presented in [77]. Bi(2212) round wires reached high performance at 4.2 K with $J_c = 1.5 \cdot 10^8$ A/m² at 26 T [78]. It is a promising material for high field magnets in the range of 30-50 T. Bi2212 wires and Bi2223 tapes are the first generation HTS conductors.

The second generation 2G tapes are coated conductors of REBCO, where RE is a rare-earth such as Y,Gd or Sm with the following structure: metallic substrate, multifunctional oxide barrier, buffer layer, superconducting layer and silver or copper stabilization. The production rate of growing layers is slow with a several meters per hour. Later improvement of REBCO structure increased the production rate to 816,4 m of 1 cm width tape with $I_c = 572$ A [73]. The production of superconducting tape is done by various growing methods, such as Pulse Laser Deposition (PLD), Atomic Laser Deposition (ALD), Metal Organic Chemical Vapour Deposition (MOCVD), Electron Beam Deposition (EBD) and others.

A more recent discovery was the MgB₂ superconductor in 2001 [79] with $T_c = 39$ K, which sets a new group of middle temperature superconductors. MgB₂ wires are prepared by ex-situ, in-situ and Internal Magnesium Diffusion (IMD) process. The ex-situ method mixes the powders of Mg and B and puts them into a metal tube. However, the in-situ method with not reacted powders has shown higher performance by $J_c = 10^8$ A/m² at 13,2 T

and 4.2 K [80]. The last production method is IMD. IMD puts boron powder around a magnesium rod and embeds it in an outer metal tube. This method shows the highest performance by $J_c = 1.3 \cdot 10^7$ A/m² at 3 T/10 K and $J_c = 5 \cdot 10^9$ A/m² at 10 T/4.2 K [81, 82]. The results led the MgB₂ as a potential material for power applications of low applied fields, since MgB₂ is easy to produce with fine wires and low cost.

At the end, there are many families of iron-based superconductors such as LaFeAsOF, SmFeAsOF, SrKFeAs and many more, which are promising. However, they did not reach the advantages of REBCO superconductors regarding high T_c and H_{c2} .

2.5 $\mathbf{E}(\mathbf{J})$ relations

The most typical $\mathbf{E}(\mathbf{J})$ relation of practical superconductors can be explained by the collective thermal flux creep [83, 84], which is a microscopic theory. This $\mathbf{E}(\mathbf{J})$ relation is

$$\mathbf{E}(\mathbf{J}) = E_c e^{-\frac{u(\mathbf{J})}{kT}} \quad (2.1)$$

and

$$u(\mathbf{J}) = u_0 \left[\left(\frac{J_c}{|\mathbf{J}|} \right)^\alpha - 1 \right]^{\frac{1}{\alpha}}, \quad (2.2)$$

where E_c is the critical electric field with usual value $1 \cdot 10^{-4}$ V/cm, k is the Boltzmann constant, T is the temperature, u is the activation energy, J_c is the critical current density, and u_0 and α are a constants. Experiments show that $\alpha \ll 1$ for many experimental situations, as is the case of technical superconductors for power and magnet applications [85], and hence $u(\mathbf{J})$ and $\mathbf{E}(\mathbf{J})$ become

$$u(\mathbf{J}) \approx u_0 \ln \left(\frac{J_c}{|\mathbf{J}|} \right) \quad (2.3)$$

and

$$\mathbf{E}(\mathbf{J}) = E_c \left(\frac{|\mathbf{J}|}{J_c} \right)^n \frac{\mathbf{J}}{|\mathbf{J}|}, \quad (2.4)$$

where J_c is the critical current density and $n = u_0/kT$, which depends on the superconducting material. The power law exponent n smoothly bends the $\mathbf{E}(\mathbf{J})$ curve from $E \approx 0$ at $|\mathbf{J}| < J_c$ to $E \gg E_c$ at $|\mathbf{J}| > J_c$. The $\mathbf{E}(\mathbf{J})$ relation above is an isotropic power law.

The smooth power law can include several dependences like $n = n(\mathbf{B})$, $J_c(\mathbf{r})$ and $J_c(\mathbf{B})$, where \mathbf{r} is a position within the superconductor. These dependencies are necessary in order to make accurate predictions compared to experiments. In the sample, J_c depends on the local magnetic field (see section 2.6), which is not constant along the sample. The superconducting material is not homogeneous, containing defects and cracks, and hence J_c changes with the position.

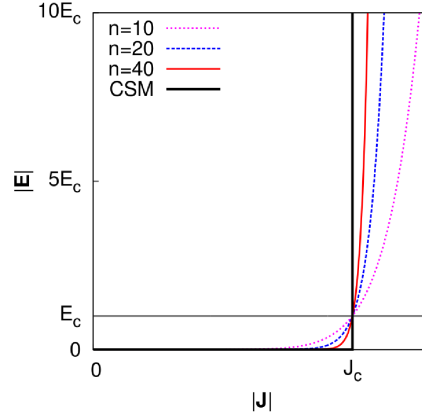


Figure 2.3: The isotropic power law with various n values and with limit $n \rightarrow \infty$, which is like Critical State model approximation.

The $\mathbf{E}(\mathbf{J})$ relation is on figure 2.3. The sharpness of the curve depends on the n -value, being between $n \rightarrow \infty$ and $n = 1$. The $\mathbf{E}(\mathbf{J})$ relation with $n \rightarrow \infty$ corresponds to the Critical-State Model CSM approximation (see section 2.6 below). The power law with $n = 1$ becomes Ohm's law $\mathbf{E}(\mathbf{J}) = (E_c/J_c)\mathbf{J}$, where $E_c/J_c = \rho$, which is the resistivity of the linear material. The superconductor models based on the power law are more realistic compared to the CSM model.

2.6 Critical State Model (CSM)

The Critical State Model CSM proposed by Bean [86] predicts the electromagnetic response of superconductors under uniform applied magnetic fields. This thesis is focused on a thin film and a bulk modelling sample, and therefore we outline the CSM on similar geometries such as infinite thin film and slab. The model proposes analytical solutions for current density and magnetic field profiles inside the sample. The modelling examples shown below are without transport current. However, there exist analytical formulas including transport current and more general geometries of the sample [87]. The case of finite size samples or the combination of the applied magnetic field and transport current requires numerical calculation.

The original CSM is a macroscopic theory with the statement that "Any electromagnetic force induces a current with constant critical current density J_c ". The $\mathbf{E}(\mathbf{J})$ relation (section 2.5) with $n \rightarrow \infty$ approaches to the CSM, being $n = 100$ often sufficient. The general CSM relation is

$$\begin{aligned} |\mathbf{J}| &= J_c, & \text{if } |\mathbf{E}| > 0 \\ &\leq J_c, & \text{if } |\mathbf{E}| = 0. \end{aligned} \quad (2.5)$$

As stated by Bossavit and Prigozhin [11, 88] the CSM enables $|\mathbf{J}| \leq J_c$ at

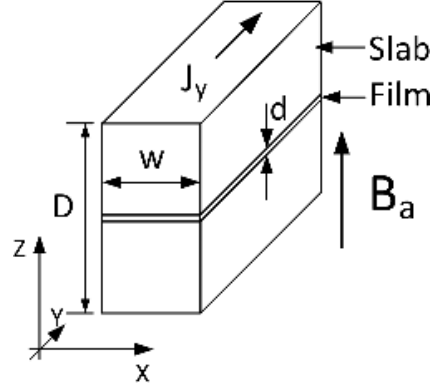


Figure 2.4: The geometry of the infinitely long thin film and slab with thickness d for thin film, thickness D for slab and width w . The applied field is along the z axes.

$|\mathbf{E}| = 0$, although in bulk samples of translation- or cylindrical-symmetry $|\mathbf{J}| = 0$ or J_c only. The cause is that long bulks, or cylinders can shield completely the applied magnetic field by currents with $|\mathbf{J}| = J_c$. The geometry of the slab and thin film is on figure 2.4, where D is the slab thickness, d is the film thickness and w is the width of both samples. The applied magnetic field is parallel to the z axis and samples are infinitely long along the y axes. The current density for a slab at the initial magnetization curve [86,87] is

$$\begin{aligned} J_y(x) &= J_c, & -w/2 < x < -a \\ &= 0, & |x| < a \\ &= -J_c, & a < x < w/2, \end{aligned} \quad (2.6)$$

where $a = w \left(1 - \frac{H_a}{H_p}\right)$, H_a is the applied magnetic field and H_p is the penetration field $H_p = J_c w / 2$. We use in this thesis terms as "magnetic flux density" and "magnetic field" indistinctively, since we do not take magnetic materials into account. We assume that the magnetic field \mathbf{B} created by superconductors is always only due to superconducting current, and hence $\mathbf{B} = \mu_0 \mathbf{H}$.

The current penetration to the slab under the applied magnetic field is on figure 2.5(a). The current density penetrates into the sample from the edges with positive sign on the left and negative on the right side. The reason is that the screening current shields the applied field following the "right hand rule" and opposing to the applied field. The screening current with $|\mathbf{J}| = J_c$ in the slab completely shields the applied field in the region with no current density, since the slab thickness allows to induce the necessary $|\mathbf{J}|$. Therefore, the penetration of the flux density [figure 2.5(c)] is in the same penetration depth as the screening current density [figure 2.5(a)]. The saturation field fully saturates the slab with the screening current and flux

density. Ramping down the applied field induces screening current density with opposite sign, which penetrates into the slab again from the edges. The penetration front rewrites the previous value of the screening current with current of the opposite sign, and hence at remanent state the penetration front reaches only half of the penetration depth. The cause is that the change in current density of the newly induced current is twice J_c instead of only J_c , as in the initial curve. The applied field has to reach minus saturation field, in order to fully saturate the slab with screening current and erase the previous current [figure 2.5(e)]. The same behaviour shows the penetration of flux density on figure 2.5(g).

The AC loss per cycle and sample length [89, 90] is

$$\begin{aligned}
 Q &= Dw \frac{2\mu_0 H_a^3}{3H_p}, & H_a < H_p \\
 &= Dw \frac{\mu_0 H_p}{3} (6H_a - 4H_p), & H_a < H_p \\
 &= Dw 2\mu_0 H_p H_a, & H_a \gg H_p.
 \end{aligned} \tag{2.7}$$

The current density of thin film [87, 91, 92] is

$$\begin{aligned}
 J_y(x) &= \frac{2J_c}{\pi} \arctan \frac{cx}{\sqrt{(b^2 - x^2)}}, & |x| < b, \\
 &= J_c \frac{x}{|x|}, & b < |x| < w/2,
 \end{aligned} \tag{2.8}$$

where

$$b = \frac{w/2}{\cosh \frac{H_a}{H_c}}, \tag{2.9}$$

$$c = \tanh \frac{H_a}{H_c}, \tag{2.10}$$

and

$$H_c = \frac{J_c d}{\pi}. \tag{2.11}$$

The thin film sample shows similar response to the applied magnetic field as the slab. The screening current penetrates into the sample under the applied magnetic field [figure 2.5(b)]. Since the film is very thin, inducing screening current of only value J_c does not generate a uniform magnetic field on the zone with $J = 0$. Therefore, there exists screening current density below J_c , which penetrates further into the center of the sample. In that zone, named sub-critical zone, the magnetic field is zero. Further increase of the applied field moves the penetration front with $|\mathbf{J}|$ around J_c deeper into the sample center. The thin film completely saturates with $|\mathbf{J}| = J_c$ with infinite applied field. The thin film penetrates with $|\mathbf{J}| = J_c$ in 90% of the width already with applied field $B_a = \mu_0 H_c \cdot \cosh^{-1}(10) = \mu_0 H_c \cdot 2.99$. The

2.7. $\mathbf{E}(\mathbf{J})$ RELATION FOR ANISOTROPIC "FORCE-FREE" EFFECTS 25

flux density penetrates into the sample with the same penetration depth as the screening current density with magnitude J_c [figure 2.5(d)]. The decrease of applied field creates penetration of new screening current with the opposite sign. The new penetration front reaches only half of the penetration depth at the remanent state and saturates the sample under minus saturation field [figure 2.5(f)]. The flux density presents the same penetration behaviour, such as erasing and rewriting the previous flux density, with the flux density of opposite sign [figure 2.5(h)].

The AC loss formula for the thin film per cycle is [91]

$$Q = \frac{8\mu_0 J_c^2 w^2}{\pi} \left[\ln \cosh \left(\frac{\pi H_{a,m}}{J_c} \right) - \frac{\pi H_{a,m}}{2J_c} \tanh \left(\frac{\pi H_{a,m}}{J_c} \right) \right], \quad (2.12)$$

where $H_{a,m}$ is the maximum applied magnetic field.

More realistic than the CSM is the Kim model, which introduces a $J_c(B)$ dependence. The critical current density J_c is not constant, but it is reduced by the local magnetic field \mathbf{B} , as it is in real superconductors. The Kim dependence [93, 94] is

$$J_c(B) = \frac{J_{c0}}{\left(1 + \frac{|\mathbf{B}|}{B_0}\right)^m}, \quad (2.13)$$

where J_{c0} is the critical current density at zero local magnetic field, m is a parameter and B_0 is a characteristic magnetic field. In this thesis, we choose the following arbitrary parameters as an example of dependence: $B_0 = 20$ mT, $m=0.5$ and $J_{c0} = 3.615 \cdot 10^{10}$ A/m². The reduction of J_c is more than 80% with the local magnetic field at 0.5 T [figure 2.6].

2.7 $\mathbf{E}(\mathbf{J})$ relation for anisotropic "force-free" effects

The Double Critical State Model DCSM assumes two different limits for the critical current density. In the case when \mathbf{J} is perpendicular to the local magnetic field \mathbf{B} , the critical current density becomes $J_{c\perp}$. In the second case with \mathbf{J} parallel to \mathbf{B} , the parallel critical current density, $J_{c\parallel}$, applies. Further development of the DCSM results in Elliptic Critical State Model introduced ECSM by Badia and Lopez. The anisotropic $\mathbf{E}(\mathbf{J})$ power law [95] based on ECSM is

$$\mathbf{E}(\mathbf{J}) = 2m_0 U_0 \left[\left(\frac{J_{\parallel}}{J_{c\parallel}} \right)^2 + \left(\frac{J_{\perp}}{J_{c\perp}} \right)^2 \right]^{m_0-1} \cdot \left(\frac{J_{\parallel}}{J_{c\parallel}^2} \mathbf{e}_{\parallel} + \frac{J_{\perp}}{J_{c\perp}^2} \mathbf{e}_{\perp} \right), \quad (2.14)$$

where $m_0 = (n+1)/2$, $U_0 = E_c J_{c\perp} / (n+1)$, $J_{\parallel} = \mathbf{J} \cdot \mathbf{B} / |\mathbf{B}|$ and $J_{\perp} = |\mathbf{J} \times \mathbf{B}| / |\mathbf{B}|$. \mathbf{e}_{\parallel} and \mathbf{e}_{\perp} are unit vectors, where $\mathbf{e}_{\parallel} = \mathbf{B} / |\mathbf{B}|$ and $\mathbf{e}_{\perp} = \mathbf{J}_{\perp} / |\mathbf{J}_{\perp}|$. The modelling method is able to include any anisotropic $\mathbf{E}(\mathbf{J})$ relation, and hence it can model the electromagnetic response of samples with force-free effects.

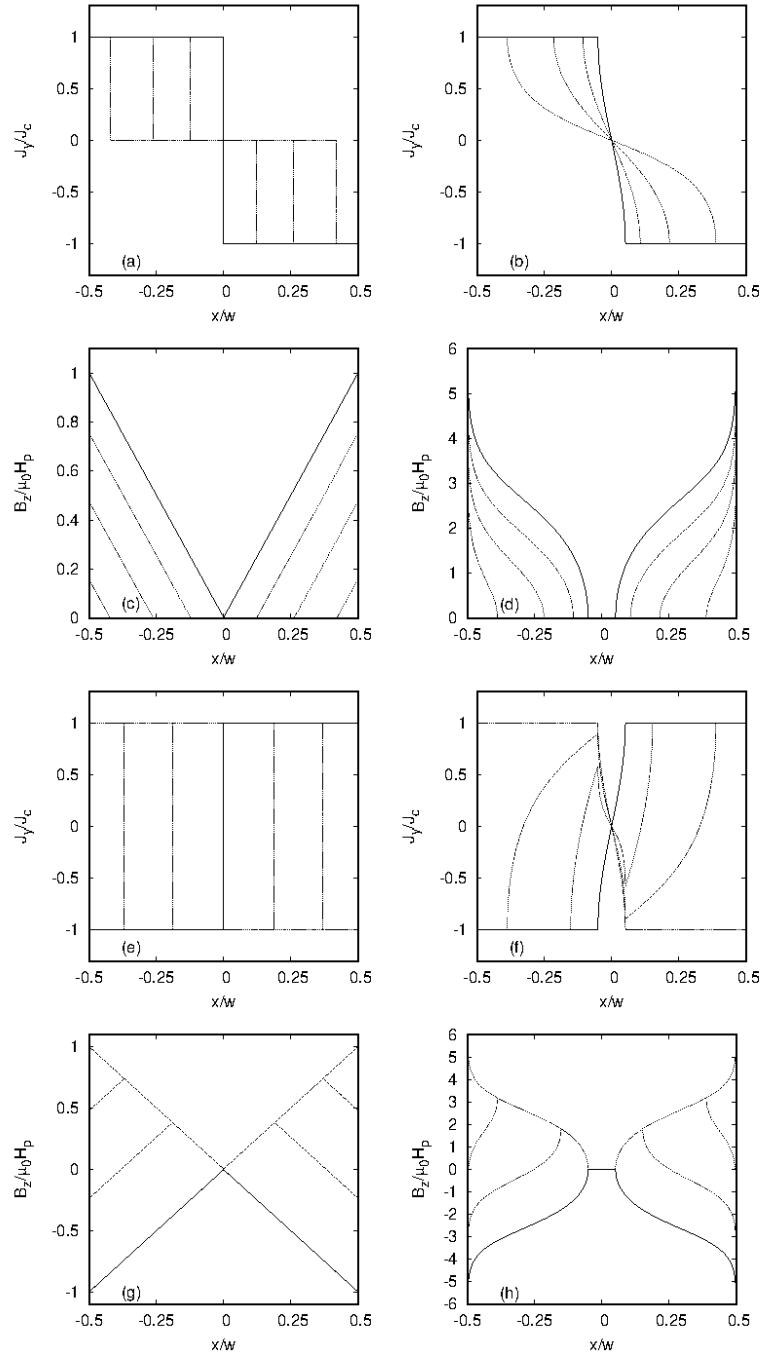


Figure 2.5: Critical State Model for a slab (a,c,e,g) and thin film (b,d,f,h). The penetration front of J_y current density (a) in the slab with applied field $B_z/\mu_0 H_p = 0.25, 0.5, 0.75, 1$ and (b) in the thin film with $B_z/\mu_0 H_p = 0.75, 1.5, 2.25, 3$. The penetration of the magnetic flux is with the same applied fields as for the current density for (c) slab and (d) film. The current (e,f) and magnetic field (g,h) penetration at the decreasing curve of the applied fields erase the previous penetrated front with the new front of opposite sign.

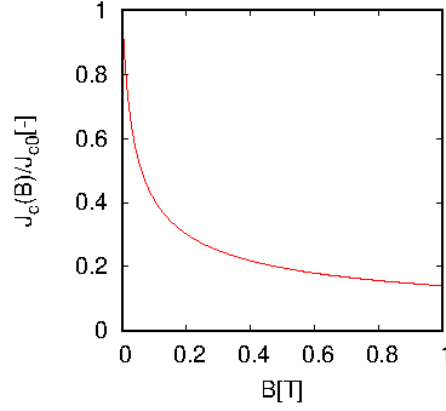


Figure 2.6: $J_c(B)$ Kim-like dependence on the local magnetic field with parameters $B_0 = 20$ mT, $m=0.5$ and $J_{c0} = 3.615 \cdot 10^{10}$ A/m².

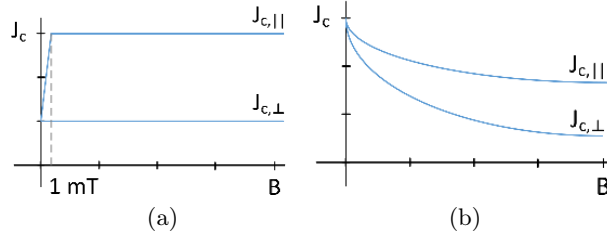


Figure 2.7: Double critical state model with $J_c(B)$ dependence (a) with linear drop of $J_{c||}$ to $J_{c\perp}$ and (b) including Kim model.

The problem of the anisotropic power law is the undefined unit vector $\mathbf{e}_{||}$ when the local magnetic field is very low or zero. We suggest the following solution, in order to remove the uncertainty of the anisotropic $\mathbf{E}(\mathbf{J})$ relation. The assumption is that when the local magnetic field is below a certain value B_{c0} (in our case we choose $B_{c0}=1$ mT), $J_{c||}$ is linearly going to $J_{c\perp}$ as it is shown on figure 2.7(a). The case with $B_{c0} \rightarrow 0$ exactly corresponds to the elliptic CSM.

Various electromagnetic modelling cases require $J_c(B)$ dependence, and hence we include Kim model for $J_{c\perp}(B)$, and $J_{c||}(B)$ as it is on figure 2.7(b).

2.8 Applied vector potential

The MEMEP 3D method (section 3.1) requires the evaluation of \mathbf{A} . Therefore, the applied vector potential, \mathbf{A}_a , has to be defined well in the modelling tool. The applied vector potential is generated from an external source like a coil or a permanent magnet. The tool uses the interpretation that the ap-

plied vector potential is created by an infinitely long external coil, in order to generate the applied vector potential. The model uses only one external coil per component of the vector potential [figure 2.9]. \mathbf{A}_a magnetizes the superconducting sample and induces screening current.

We can assume only one component of the applied magnetic field $\mathbf{B}_a = B_{az}\mathbf{e}_z$, which caused by the applied vector potential \mathbf{A}_a by one external coil with infinite Y direction [figure 2.9(c)]. The vector potential is defined by Coulomb's gauge $\nabla \cdot \mathbf{A}_a = 0$, and hence it follows the direction of the current. The vector potential becomes

$$\mathbf{A}[\mathbf{J}](\mathbf{r}) = \frac{\mu_0}{4\pi} \int_V dV' \frac{\mathbf{J}(\mathbf{r}')}{|\mathbf{r} - \mathbf{r}'|}. \quad (2.15)$$

Then, if $\mathbf{J}(\mathbf{r}) = J(\mathbf{r})\mathbf{u}$, where \mathbf{u} is a constant unit vector, $\mathbf{A}(\mathbf{r}) = A(\mathbf{r})\mathbf{u}$.

In general, we can consider \mathbf{A}_a corresponding to \mathbf{B}_a in any direction, $\mathbf{A}_a = A_{ax}\mathbf{e}_x + A_{ay}\mathbf{e}_y + A_{az}\mathbf{e}_z$. According to the definition of vector potential, $\nabla \times \mathbf{A}_a = \mathbf{B}_a$

$$\mathbf{B}_a = \begin{pmatrix} \mathbf{e}_x & \mathbf{e}_y & \mathbf{e}_z \\ \frac{\partial}{\partial x} & \frac{\partial}{\partial y} & \frac{\partial}{\partial z} \\ A_x & A_y & A_z \end{pmatrix}$$

$$\mathbf{B}_a = \mathbf{e}_x \left(\frac{\partial A_z}{\partial y} - \frac{\partial A_y}{\partial z} \right) + \mathbf{e}_y \left(\frac{\partial A_x}{\partial z} - \frac{\partial A_z}{\partial x} \right) + \mathbf{e}_z \left(\frac{\partial A_y}{\partial x} - \frac{\partial A_x}{\partial y} \right). \quad (2.16)$$

The second part of each magnetic field component $-\frac{\partial A_y}{\partial z}$, $-\frac{\partial A_z}{\partial x}$, $-\frac{\partial A_x}{\partial y}$ are set to zero, since they are generated by infinitely long coils in that direction. The magnetic field becomes $\mathbf{B}_a = \frac{\partial A_z}{\partial y}\mathbf{e}_x + \frac{\partial A_x}{\partial z}\mathbf{e}_y + \frac{\partial A_y}{\partial x}\mathbf{e}_z$, where the components can be rewritten as

$$B_{ax} = \frac{\partial A_z}{\partial y} \Rightarrow A_z = B_{ax}y,$$

$$B_{ay} = \frac{\partial A_x}{\partial z} \Rightarrow A_x = B_{ay}z,$$

$$B_{az} = \frac{\partial A_y}{\partial x} \Rightarrow A_y = B_{az}x. \quad (2.17)$$

Then, the vector potential results in $\mathbf{A}_a = B_{ay}z\mathbf{e}_x + B_{az}x\mathbf{e}_y + B_{ax}y\mathbf{e}_z$, and hence 3 split coils infinite in the x, y, z directions generate the vector potential in the x, y, z direction, respectively [figure 2.9].

The applied magnetic field for sinusoidal waveform is defined by

$$\mathbf{B}_a = B_{am} \sin(2\pi\omega f) \cdot \mathbf{a}, \quad (2.18)$$

where B_{am} is the amplitude of the applied field, f is the frequency and \mathbf{a} is a unit vector in the direction of the applied field. The applied field direction

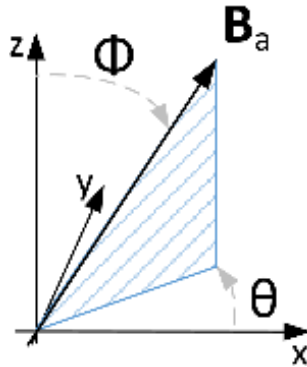


Figure 2.8: The applied magnetic field direction is defined by ϕ, θ in the spherical coordinate system.

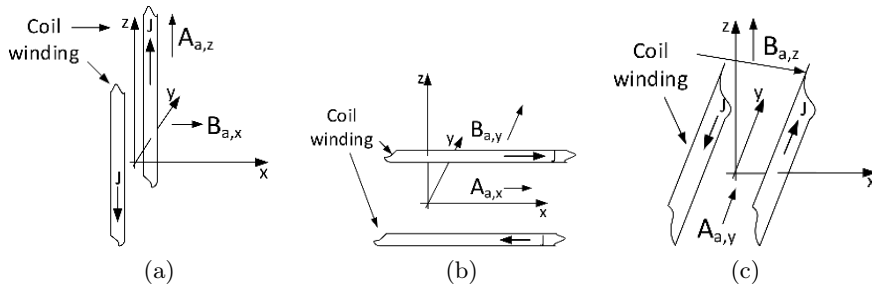


Figure 2.9: The orientation of infinitely long external coils generating uniform applied magnetic field in the direction parallel to (a) x axes, (b) y axes and (c) z axes.

is set by two angles (ϕ, θ) in spherical coordinate system [figure 2.8], where each component is calculated as follows

$$\begin{aligned} a_x &= \sin \phi \cos \theta, \\ a_y &= \sin \phi \sin \theta, \\ a_z &= \cos \phi \end{aligned} \quad (2.19)$$

The applied field parameters like B_{am}, ϕ, θ, f are set in the input file (section 9), and hence the modelling tool can model any applied magnetic field.

2.9 Eddy current problem

The main goal of electro dynamic modelling is to find electromagnetic variables like $\mathbf{E}, \mathbf{J}, \mathbf{B}, \mathbf{A}$ for any shape of chosen sample geometry with given initial conditions. Normal conductors, such as cooper or aluminium, are linear materials with constant conductivity. On the other hand, superconductors are highly non-linear, and hence to find the required electric variables is

problematic. In addition, ferromagnetic materials with non-linear magnetic permeability could also be present. The properties of any material are defined by μ , ε , ρ , where μ is the permeability, ε is the permittivity and ρ is the resistivity, so that $\mathbf{B} = \mu(\mathbf{H})\mathbf{H}$, $\mathbf{D} = \varepsilon(\mathbf{E})\mathbf{E}$, $\mathbf{E} = \rho(\mathbf{J})\mathbf{J}$. The magnetic field created by the superconductor always assumes permittivity of vacuum μ_0 , $\mathbf{B} = \mu_0\mathbf{H}$.

Analytical solutions for arbitrary shapes and resistivities do not exist. However, there exist several formulations of Maxwell differential equations, which can find the electromagnetic response of any sample, such as those in the following sections. Several formulations are based on the Finite Element Method [96]. Later, we also outline variational principles.

2.9.1 \mathbf{A} - ϕ - \mathbf{J} formulation

The eddy current problem can be solved by many kinds of formulations. A common one is the \mathbf{A} - ϕ - \mathbf{J} formulation. The formulation is based on \mathbf{A} vector potential, ϕ scalar potential and \mathbf{J} current density. The two main differential equations are derived from Maxwell equations. The formulation starts with the magnetic field, \mathbf{B} ,

$$\mathbf{B} = \nabla \times \mathbf{A}, \quad (2.20)$$

in order to derive the first equation. The Faraday's law is

$$\nabla \times \mathbf{E} = -\dot{\mathbf{B}} \quad (2.21)$$

and by substitution of magnetic field it becomes

$$\nabla \times \mathbf{E} = -(\nabla \times \dot{\mathbf{A}}). \quad (2.22)$$

The solution of the differential equation is

$$\mathbf{E} = -\dot{\mathbf{A}} - \nabla\phi, \quad (2.23)$$

which is the general equation of the electric field equation, \mathbf{E} . This is the first equation of the formulation, where $\nabla \times (\nabla\phi) = 0$ for any function ϕ .

The second equation definition starts from Ampere's law

$$\nabla \times \mathbf{H} = \mathbf{J} + \dot{\mathbf{D}}. \quad (2.24)$$

The displacement current is neglected for quasi static model, resulting in

$$\nabla \times \mathbf{H} = \mathbf{J}. \quad (2.25)$$

The magnetic field for non linear magnetic materials is

$$\mathbf{H} = \mu^{-1}(\mathbf{B})\mathbf{B}, \quad (2.26)$$

where μ is the anisotropic tensor of the magnetic material. The Ampere's law can be rewritten as

$$\mathbf{J} = \nabla \times [\mu^{-1}(\mathbf{B})\mathbf{B}] \quad (2.27)$$

and by substituting (2.20) it becomes

$$\mathbf{J} = \nabla \times ((\nabla \times \mathbf{A})\mu^{-1}(\nabla \times \mathbf{A})). \quad (2.28)$$

The current density defined by the vector potential (2.28) is the second equation for the \mathbf{A} - ϕ - \mathbf{J} formulation. For no magnetic materials and Coulomb's gauge, joining equation (2.23) and (2.28) becomes

$$\mathbf{E}(-\nabla^2 \mathbf{A}) = -\dot{\mathbf{A}} - \nabla\phi, \quad (2.29)$$

where $\mathbf{E}(\mathbf{J})$ follows the constitutive relation of the material. The transport current density is defined in the cross-section surface of each superconducting domain like

$$\int_{D_i} \mathbf{J} \cdot d\mathbf{S} = I_i, \quad (2.30)$$

where D_i is the domain of i index and $d\mathbf{S}$ is the differential area of the surface. The formulation has to discretize the air around the sample and solve it. However, the air is assumed as a non-conductive space. The main two differential equations (2.23) and (2.28) are defined for each unknown variable \mathbf{X} . The differential algebraic equation is combined to the single matrix equation

$$M\dot{\mathbf{X}} = \mathbf{f}(t, \mathbf{X}), \quad (2.31)$$

where M is the mass matrix of the problem at time t and function f depends on both t and \mathbf{X} .

The solutions are the vector and scalar potentials. The matrix is solved in the time domain by a Partial Differential Equation (PDE) solver. These could be either in commercial software or self-programmed.

2.9.2 \mathbf{T} - ψ formulation

Another type of eddy-current problem-formulation is \mathbf{T} - ψ , where \mathbf{T} is the vector current potential and ψ is the scalar current potential. The formulation is based on the \mathbf{T} variable, which is defined as

$$\mathbf{J} = \nabla \times \mathbf{T}. \quad (2.32)$$

When we substitute (2.32) into $\nabla \cdot \mathbf{J} = 0$, then the function is always satisfied, since $\nabla \cdot (\nabla \times \mathbf{X}) = 0$ is valid for any function \mathbf{X} . As a result of Ampere's law with neglected displacement current (2.25) and (2.32),

$$\mathbf{H} = \mathbf{T} - \nabla\psi. \quad (2.33)$$

These two equations (2.32) and (2.33) serve as base for solving the Maxwell equations.

The Faraday's law with implemented $\mathbf{B} = \mu\mathbf{H}$ and $\mathbf{E} = \rho\mathbf{J}$ relations results in

$$\nabla \times (\rho(\mathbf{J})\mathbf{J}) = -\partial_t[\mu(\mathbf{H}) \cdot \mathbf{H}]. \quad (2.34)$$

The $\nabla \cdot \mathbf{B} = 0$ can be rewritten in the same way into

$$\nabla \cdot [\mu(\mathbf{H})\mathbf{H}] = 0. \quad (2.35)$$

The substitution of (2.32) and (2.33) into (2.34) and (2.35) we get

$$\nabla \times [\rho(\nabla \times \mathbf{T})(\nabla \times \mathbf{T})] = -\partial_t[\mu(\mathbf{T} - \nabla\psi) \cdot (\mathbf{T} - \nabla\psi)] \quad (2.36)$$

and

$$\nabla \cdot [\mu(\mathbf{T} - \nabla\psi)(\mathbf{T} - \nabla\psi)] = 0. \quad (2.37)$$

The previous two differential equations are the main formulation equations. The total current in a certain cross-section Ω is edge defined as

$$\int_{\partial\Omega} \mathbf{T} \cdot d\mathbf{l} = I, \quad (2.38)$$

where $d\mathbf{l}$ is the differential length of the edge. The formulation creates the matrix M of all equations for chosen geometry in the space and time t . The similar matrix equation (2.31) have to be solved by the solver in the Finite element method.

2.9.3 H formulation

The next formulation is the H formulation [95], which is based on a magnetic field. There is no gauge for vector and scalar potential. The H formulation becomes popular and widely used, since commercial software like Comsol allows to enter differential equations directly into the PDE solver.

The formulation is based on Ohm's law

$$\mathbf{E} = \rho(\mathbf{J})\mathbf{J} + E_c, \quad (2.39)$$

where E_c is a critical voltage in the sub-domains. The substitution of Ampere's law with neglected displacement current rewrites Ohm's law into

$$\mathbf{E} = \rho(\nabla \times \mathbf{H})\nabla \times \mathbf{H} + E_c. \quad (2.40)$$

After another substitution by Faraday's law and (2.26) the equation becomes

$$-\partial_t[\mu(\mathbf{H})\mathbf{H}] = \nabla \times [\rho(\nabla \times \mathbf{H}) \cdot \nabla \times \mathbf{H} + E_c]. \quad (2.41)$$

The previous equation is the core of the H formulation. The current is defined in the cross-section of the Ω domain as

$$\int_{\partial\Omega} \mathbf{H} \cdot d\mathbf{l} = I. \quad (2.42)$$

The differential equations are defined in space for any geometry and solved by the solver via Finite Element Method FEM.

2.9.4 Variational principles

A completely different way of solving the eddy current problem is by the variational method. Any variational method is based on a certain functional. The Euler differential equations of the functional should correspond to the master equation of the electromagnetic quantity derived from Maxwell equations, such as the master equations of the $\mathbf{A} - \phi - \mathbf{J}$, $\mathbf{T} - \psi$ and \mathbf{H} above. There has to exist first and second functional derivatives of the functional. The first derivative obtains the differential equations at the extreme of the functional and the second derivative proves the uniqueness of the minimum, and hence uniqueness of the solution. If both conditions are satisfied, the solution of the functional is the same as the solution of the equivalent formulation by the differential equation.

The functional is solved by a minimization algorithm, such as the maximum gradient method, Golden section search, Downhill simplex method or Powell's method [97]. The variational method is written by a certain state variable; which can be defined around or only inside the sample, depending on the formulation and on the physical meaning of the functional. The minimization finds the solution of the unknown variable inside the sample in given boundaries and initial conditions. More details on Variational principles are in section 3.5.

Chapter 3

Model and Numerical method

3D modelling tools are necessary, since 2D cross-sectional models cannot include all finite size effects, and hence the models predictions are not accurate in difficult geometries of the sample. There are many 3D variational formulations like the \mathbf{H} one suggested by Bossavit [23]. Further development of the \mathbf{H} formulation was presented by Elliott [24] and Kashima [25]. A 2D- \mathbf{J} formulation was introduced Prigozhin [11–13] either for infinitely long problems or thin films. Badia and Lopez introduced the Euler-Lagrange formalism for the \mathbf{H} formulation [98, 99].

The modelling method needs to handle a huge number of degrees of freedom, in order to solve the full 3D model with all finite size effects. Therefore, the calculation time has to be relatively fast even though there are a lot of elements in the mesh.

Therefore, we focused on the development of a new modelling tool based on the variational method of the Minimum Electro-Magnetic Entropy Production in 3D (MEMEP 3D), which is a fast method. The MEMEP 3D method is based on a new formulation of \mathbf{T} . It is proved by the Euler-equations of the 3D functional that the minimum of the functional is the solution of the Maxwell differential equations. The solution is a minimum and it is unique. This method is valid for any $\mathbf{E}(\mathbf{J})$ relation, including anisotropic force-free effects.

Any geometry of the sample is discretized and variables are set into the elements in the grid. The minimization solves the functional and finds the solution of the current modelling situation with initial conditions. Since the 3D object contains a huge number of degrees of freedom, the numerical method uses several strategies to speed up calculations, such as parallel computing, sectors and symmetry. Parallel computing uses OpenMP and BoostMPI protocols. The sector method decreases the computing time by reducing the minimized elements into sectors and solve them separately, which is faster than minimizing entire sample at once. Symmetry speeds up the calculation time of the solution, and hence only one quarter or one eight

needs to be solved.

3.1 Mathematical model

The Minimum Electro-Magnetic Entropy Production in 3D (MEMEP 3D) method is based on the variational method. The main core of the method is a 3D functional (3.25), which is solved by minimization. The minimum of the functional is the same as the solution of the general differential equation of the potential (3.1). The general electric field, \mathbf{E} , equation is

$$\mathbf{E}(\mathbf{J}) + \dot{\mathbf{A}} + \nabla\phi = 0, \quad (3.1)$$

where \mathbf{A} is the vector potential, ϕ is the scalar potential and \mathbf{J} is the current density. The general potential equation can be rewritten by Maxwell equations to different forms, and hence there are many formulations such as $\mathbf{A} - \phi - \mathbf{J}$, $\mathbf{T} - \psi$ or \mathbf{H} (section 2.9). The MEMEP 3D uses Coulomb's gauge $\nabla \cdot \mathbf{A} = 0$. Since there are no magnetic materials, the magnetic field follows $\mathbf{B} = \mu_0 \mathbf{H}$. Since $\nabla \times \mathbf{A} = \mathbf{B}$, the Ampere's law (2.24) becomes

$$\nabla \times \frac{\nabla \times \mathbf{A}}{\mu_0} = \mathbf{J}. \quad (3.2)$$

From vector calculus the equation with the double rotor of \mathbf{A} becomes

$$\frac{\nabla(\nabla \cdot \mathbf{A}) - \nabla^2 \mathbf{A}}{\mu_0} = \mathbf{J}. \quad (3.3)$$

The first term vanishes with Coulomb's gauge ($\nabla \cdot \mathbf{A} = 0$),

$$\frac{-\nabla^2 \mathbf{A}}{\mu_0} = \mathbf{J}. \quad (3.4)$$

The vector potential from the differential equation above can be found as the following volume integral of the current density

$$\mathbf{A}[\mathbf{J}](\mathbf{r}) = \frac{\mu_0}{4\pi} \int_V dV' \frac{\mathbf{J}(\mathbf{r}')}{|\mathbf{r} - \mathbf{r}'|}. \quad (3.5)$$

The general electric field equation can be rewritten by vector potential as

$$\mathbf{E} \left(\frac{-\nabla^2 \mathbf{A}}{\mu_0} \right) + \dot{\mathbf{A}} + \nabla\phi = 0. \quad (3.6)$$

The time derivative of the vector potential is $\dot{\mathbf{A}} \equiv \frac{\partial \mathbf{A}}{\partial t} \approx \frac{\Delta \mathbf{A}}{\Delta t}$. We assume that the electric field is time-independent between two time steps. The total vector potential is $\mathbf{A} = \mathbf{A}_0 + \Delta \mathbf{A}$, where \mathbf{A}_0 is the vector potential at the previous time step and $\Delta \mathbf{A}$ is the change between two time steps. The

present time is $t = t_0 + \Delta t$, where t_0 is the time at the previous time step and Δt is the change in time between two time steps. The final form of the general electric field equation is

$$\mathbf{E} \left(\frac{-\nabla^2 (\mathbf{A}_0 + \Delta \mathbf{A})}{\mu_0} \right) + \frac{\Delta \mathbf{A}}{\Delta t} + \nabla \phi = 0, \quad (3.7)$$

and Coulomb's gauge is

$$\nabla \cdot (\mathbf{A}_0 + \Delta \mathbf{A}) = 0, \quad (3.8)$$

which are differential equations. Equation (3.7) corresponds to the general equation to the Eddy current problem in \mathbf{A} formulation (section 2.9.1).

The functional is simplified and later proved that the minimization of the functional is the same as the solution of (3.7,3.8). The functional is defined at each time step as

$$\begin{aligned} L[\Delta \mathbf{J}] &= \int_V dV \left(\frac{1}{2} \Delta \mathbf{J} \cdot \frac{\mathbf{A}[\Delta \mathbf{J}]}{\Delta t} \right. \\ &\quad \left. + \Delta \mathbf{J} \cdot \frac{\Delta \mathbf{A}_a}{\Delta t} + U(\mathbf{J}_0 + \Delta \mathbf{J}) + \nabla \phi \cdot (\mathbf{J}_0 + \Delta \mathbf{J}) \right) \\ &= \int_V dV \int_V dV' \frac{\mu_0}{8\pi \Delta t} \frac{\Delta \mathbf{J} \cdot \Delta \mathbf{J}'}{|\mathbf{r} - \mathbf{r}'|} \\ &\quad + \int_V dV \left(\Delta \mathbf{J} \cdot \frac{\Delta \mathbf{A}_a}{\Delta t} + U(\mathbf{J}_0 + \Delta \mathbf{J}) + \nabla \phi \cdot (\mathbf{J}_0 + \Delta \mathbf{J}) \right), \end{aligned} \quad (3.9)$$

where \mathbf{A}_a is the applied vector potential, \mathbf{J}_0 is the current density at t_0 , and the total current density at time $t = t_0 + \Delta t$ is $\mathbf{J} = \mathbf{J}_0 + \Delta \mathbf{J}$. The dissipation factor is defined as

$$U(\mathbf{J}) \equiv \int_0^{\mathbf{J}} d\mathbf{J}' \cdot \mathbf{E}(\mathbf{J}'), \quad (3.10)$$

and the solution for the isotropic power law of (2.4) is

$$U(\mathbf{J}) = \frac{E_c J_c}{n+1} \left(\frac{|\mathbf{J}|}{J_c} \right)^{n+1}, \quad (3.11)$$

while for the force-free anisotropic $\mathbf{E}(\mathbf{J})$ relation of (2.14), the dissipation factor is

$$U(\mathbf{J}, \mathbf{B}) = U_0 \left[\left(\frac{J_{\parallel}}{J_{c\parallel}} \right)^2 + \left(\frac{J_{\perp}}{J_{c\perp}} \right)^2 \right]^{m_0}. \quad (3.12)$$

The electric field created by the current density is well defined, since $\nabla_{\mathbf{J}} \times \mathbf{E}(\mathbf{J}) = 0$, and hence the line integral of (3.10) does not depend on the integration path. Any physical $\mathbf{E}(\mathbf{J})$ relation follows $\nabla_{\mathbf{J}} \times \mathbf{E}(\mathbf{J}) = 0$ due to irreversible thermodynamical principles [99]. According to the Onsager relations, the differential resistivity matrix should be symmetric, which causes $\nabla_{\mathbf{J}} \times \mathbf{E} = 0$. In addition $\nabla_{\mathbf{J}} U = \mathbf{E}(\mathbf{J})$.

The extreme of the functional is when the first functional derivative is zero $\delta L[\Delta \mathbf{J}] = 0$. The first variation is

$$\delta L[\Delta \mathbf{J}] = \epsilon \left(\frac{d}{d\epsilon} L[\Delta \mathbf{J} + \epsilon \mathbf{g}] \right)_{\epsilon=0}, \quad (3.13)$$

where ϵ is an arbitrary small parameter and \mathbf{g} is an arbitrary function with continuous second derivatives except at the sample surface and equal zero outside the sample. The first variation of the functional becomes (8.7)

$$\begin{aligned} \delta L[\Delta \mathbf{J}] &= \epsilon \int_V dV \mathbf{g} \cdot \int_V dV' \frac{\mu_0}{4\pi \Delta t} \frac{\Delta \mathbf{J}'}{|\mathbf{r} - \mathbf{r}'|} \\ &+ \epsilon \int_V dV \mathbf{g} \cdot \left(\frac{\Delta \mathbf{A}_a}{\Delta t} + \mathbf{E}(\mathbf{J}_0 + \Delta \mathbf{J}) + \nabla \phi \right) \\ &= \epsilon \int_V dV \mathbf{g} \cdot \left(\frac{\mathbf{A}[\Delta \mathbf{J}] + \Delta \mathbf{A}_a}{\Delta t} + \mathbf{E}(\mathbf{J}_0 + \Delta \mathbf{J}) + \nabla \phi \right). \end{aligned} \quad (3.14)$$

The Euler equation (appendix 8.2) applies on the functional. Then,

$$\mathbf{E}(\mathbf{J}_0 + \Delta \mathbf{J}) + \frac{(\mathbf{A}[\Delta \mathbf{J}] + \Delta \mathbf{A}_a)}{\Delta t} + \nabla \phi = 0, \quad (3.15)$$

which corresponds to the extreme $\delta L[\Delta \mathbf{J}] = 0$. The functional is the same as the general potential equation (3.7). Therefore, the minimization of (3.9) is the same as solving the differential equation (3.7). The extreme of the functional is minimum and the minimum is unique when the second derivative is always positive, $\delta^2 L[\Delta \mathbf{J}] > 0$. The second variation of the functional is defined as

$$\delta^2 L \equiv \frac{1}{2} \epsilon^2 \left(\frac{d^2}{d\epsilon^2} L[\Delta \mathbf{J} + \epsilon \mathbf{g}] \right)_{\epsilon=0}, \quad (3.16)$$

and following the formulas in appendix 8.2 it becomes

$$\begin{aligned} \delta^2 L[\Delta \mathbf{J}] &= \frac{1}{2} \epsilon^2 \int_V dV \int_V dV' \frac{\mu_0}{4\pi \Delta t} \frac{\mathbf{g}(\mathbf{r}) \cdot \mathbf{g}(\mathbf{r}')}{|\mathbf{r} - \mathbf{r}'|} \\ &+ \frac{1}{2} \epsilon^2 \int_V dV \mathbf{g}(\mathbf{r}) \bar{\rho}(\mathbf{J}_0 + \Delta \mathbf{J}) \mathbf{g}(\mathbf{r}). \end{aligned} \quad (3.17)$$

The first term is the magnetic interaction energy, which is always positive, and $\bar{\rho}$ is the differential resistivity matrix, which is always positive definite due to thermodynamical principles. A matrix is \bar{M} positive definite if $v^T \bar{M} v$ is always positive, where v is a vector. Then, $\delta^2 L > 0$ always.

The functional contains the scalar potential, which is unknown during the minimization of $L[\Delta \mathbf{J}]$. The possible solution is to use a second functional of the scalar potential and proof the extreme of it. The functional is

$$L[\Delta \mathbf{J}] = \int_V dV \nabla \phi \cdot (\mathbf{J}_0 + \Delta \mathbf{J}). \quad (3.18)$$

The first functional derivative of the scalar potential functional is

$$\delta L[\phi] = \epsilon \frac{d}{d\epsilon} L[\phi + \epsilon g] = \int_V dV g \nabla \cdot (\mathbf{J}_0 + \Delta \mathbf{J}). \quad (3.19)$$

The Euler equation of this functional is $\nabla \cdot \mathbf{J} = 0$. Then, the extreme of the functional imposes current conservation. The problem of the scalar potential functional is that the second derivative is zero, and hence the extreme of functional is not a minimum. Therefore, the functional cannot be split and solved by minimization separately.

Another approach to solve this problem is to use a different formulation. \mathbf{T} is defined as the effective magnetization, so that

$$\mathbf{J} = \nabla \times \mathbf{T}. \quad (3.20)$$

Since there are no surface currents, the tangential components of \mathbf{T} on the surface needs to be continuous. Since the effective magnetization vanishes outside the sample, the tangential component of \mathbf{T} vanishes on the surface. The total current density inside the sample is the current from magnetization and transport current density \mathbf{J}_t ,

$$\mathbf{J} = \nabla \times \mathbf{T} + \mathbf{J}_t. \quad (3.21)$$

The total current crossing the outer surface of the sample is due to transport current, since the effective magnetization creates no net current

$$I = \int_S d\mathbf{s} \cdot \mathbf{J} = \int_S d\mathbf{s} \cdot \mathbf{J}_t. \quad (3.22)$$

The functional with \mathbf{T} formulation becomes

$$\begin{aligned} L[\Delta \mathbf{T}] &= \int_V dV \left(\frac{1}{2} \nabla \times \Delta \mathbf{T} \cdot \frac{\mathbf{A}[\nabla \times \Delta \mathbf{T}]}{\Delta t} + \nabla \times \Delta \mathbf{T} \cdot \frac{(\Delta \mathbf{A}_a + \Delta \mathbf{A}_t)}{\Delta t} \right. \\ &\quad \left. + U(\mathbf{J}_0 + \Delta \mathbf{J}_t + \nabla \times \Delta \mathbf{T}) + \nabla \phi \cdot (\mathbf{J}_0 + \Delta \mathbf{J}_t + \nabla \times \Delta \mathbf{T}) \right) \end{aligned} \quad (3.23)$$

where \mathbf{A}_t is the vector potential created by $\Delta \mathbf{J}_t$. The last term contains the scalar potential, which according to vector calculus follows

$$\begin{aligned} \int_V dV \nabla \phi \cdot (\mathbf{J}_0 + \Delta \mathbf{J}_t + \nabla \times \Delta \mathbf{T}) &= \int_V dV \nabla \phi \cdot (\mathbf{J}_t + \nabla \times \mathbf{T}) \\ &= \int_{S_i} d\mathbf{s} \cdot (\phi \mathbf{J}_t) + \int_{S_o} d\mathbf{s} \cdot (\phi \mathbf{J}_t). \end{aligned} \quad (3.24)$$

The integral domains are S_i, S_o , which are the surfaces of input and output of \mathbf{J}_t . This term does not depend on the effective magnetization, and hence it can be dropped out from the functional. If we choose S_i and S_o as equipotentials, this integral turns into $\Delta \phi I_t$, where $\Delta \phi$ is the voltage drop between

the sample ends. In conclusion, the complete functional with \mathbf{T} formulation is

$$\begin{aligned}
L[\Delta\mathbf{T}] &= \int_V dV \left(\nabla \times \Delta\mathbf{T} \cdot \frac{\mathbf{A}[\nabla \times \Delta\mathbf{T}]}{2\Delta t} \right. \\
&\quad \left. + \nabla \times \Delta\mathbf{T} \cdot \frac{(\Delta\mathbf{A}_a + \Delta\mathbf{A}_t)}{\Delta t} + U(\mathbf{J}_0 + \Delta\mathbf{J}_t + \nabla \times \Delta\mathbf{T}) \right) \\
&= \int_V dV \left(\nabla \times \Delta\mathbf{T} \cdot \frac{(\Delta\mathbf{A}_a + \Delta\mathbf{A}_t)}{\Delta t} + U(\mathbf{J}_0 + \Delta\mathbf{J}_t + \nabla \times \Delta\mathbf{T}) \right) \\
&\quad + \int_V dV \int_V dV' \frac{\mu_0}{8\pi\Delta t} \frac{(\nabla \times \Delta\mathbf{T}) \cdot (\nabla' \times \Delta\mathbf{T}')}{|\mathbf{r} - \mathbf{r}'|}, \tag{3.25}
\end{aligned}$$

which is the main core of the entire MEMEP 3D method with \mathbf{T} as unknown variable. The minimum of the functional corresponds to the physical entropy production. Then, the minimum of the functional corresponds to the minimum of the entropy production. This gives the name of the method, as Minimum Electro-Magnetic Entropy Production [17, 98].

3.2 Discretization

The modelling tool needs to create mesh according to the sample size specifications in the input file. The discretization process creates an orthogonal mesh in the x, y, z directions and saves the variables into the data structures. In this thesis, we consider only uniform mesh but the program is also prepared for non-uniform mesh. The MEMEP 3D method avoids taking variables in the air around the modelling sample, and hence the discretization creates a mesh only inside the sample. The functional (section 3.1) contains a lot of variables, which have to be dedicated in the correct positions inside the mesh, in order to evaluate properly $\nabla \times \mathbf{T}$ and other quantities. The sample is split into a lot of small elements [figure 3.1(a)]. The current state of the modelling tool uses rectangular or square prisms, called cells [figure 3.1(b)]. The code uses many types of elements such as cells, three kinds of surfaces (X, Y, Z) and three kinds of edges (X, Y, Z) [figure 3.1(b)]. The normal of each kind of surface is parallel to the axis of its label (X surfaces are perpendicular to the x axis, Y to y , and Z to z) [figure 3.2(a)]. Each kind of edge is parallel to the axis of its label (X edges are parallel to x axis, Y to y , and Z to z) [figure 3.2(b)].

Each type of element contains many parameters and variables saved in the RAM memory during the calculation time. Apart from geometrical variables, the cells contain the dissipation factor U , power law value n , critical current densities $J_c, J_{c\perp}, J_{c\parallel}$, magnetic field \mathbf{B} , electric field \mathbf{E} , and interpolated current density \mathbf{J}_{int} and effective magnetization \mathbf{T}_{int} . Each surface

Elements	Variables
Cell	$\mathbf{r}_c, V, \text{address } (i, j, k), (a, b, c), U, n, J_{c\perp}, J_{c\parallel}, \mathbf{B}, \mathbf{E}, \mathbf{J}_{\text{int}}, \mathbf{T}_{\text{int}}$
Surface	$\mathbf{r}_c, \text{address } (i, j, k), (a, b), S, J, \Delta J, J_0, V_i, A, \Delta A, A_0$
Edge	$\mathbf{r}_c, l, \text{address } (i, j, k), T, \Delta T, T_0$

Table 3.1: Variables in the elements stored in the memory during the minimization process, where \mathbf{r}_c is the central position vector, V is the volume, (i, j, k) is the address in the mesh, (a, b, c) are the sizes of the edges, U is the dissipation factor, n is the power law exponent, $J_{c\perp}$ is the perpendicular critical current density, $J_{c\parallel}$ is the parallel current density, \mathbf{B} is the magnetic field, \mathbf{E} is the electric field, \mathbf{J}_{int} interpolated current density from surfaces, \mathbf{T}_{int} interpolated effective magnetization from the edges, S is the surface area, J, J_0 are the current density at the time t, t_0 , respectively, $\Delta J = J - J_0$, V_i is the volume of influence, A, A_0 are the vector potentials at appropriate time, $\Delta A = A - A_0$, l is the length of edge, T, T_0 are the effective magnetization at appropriate time, and $\Delta T = T - T_0$.

contains the address of the 4 neighbour edges, addresses of 8 equivalent surfaces for symmetry, $(J_0, \Delta J, J)$, and vector potential perpendicular to the surface $(A_0, \Delta A, A)$. Each type of edge contains the address of the 4 neighbour surfaces, address of 4 neighbour cells, address of 8 equivalent edges for symmetry, and effective magnetization along the edge $(T_0, \Delta T, T)$. All variables are listed in table 3.1.

There are two types of addresses for each type of elements, in order to access the variable values faster and easier. The first type of address is on figure 3.3 (a); where the elements are cells. This cell address is by sequence order. The second type of the address is according the (i, j, k) coordinate system figure 3.3(b). The sequence address is suitable for code loops with all elements of one type. The coordinate address is suitable in the case of filtering any elements by any restrictions, as well as to easily determine neighbour elements.

The functional in integral form (3.25) is changed by the discretization to the following form with \mathbf{J} as variable

$$\begin{aligned}
L[\Delta \mathbf{J}] &= \frac{1}{2\Delta t} \sum_{s \in \{x, y, z\}} \sum_{i, j=1}^{n_s} V_{si} V_{sj} \Delta J_{si} \Delta J_{sj} a_{sij} \\
&+ \sum_{s \in \{x, y, z\}} \sum_{i=1}^{n_s} V_{si} \Delta J_{si} \Delta A_{a, si} + \sum_{c=1}^{n_c} V_c U_c, \quad (3.26)
\end{aligned}$$

where s is the type of the surface, i, j are the surface indexes, c is the cell, n_c the total number of cells, a_{sij} is the average vector potential and $A_{a, si}$ is

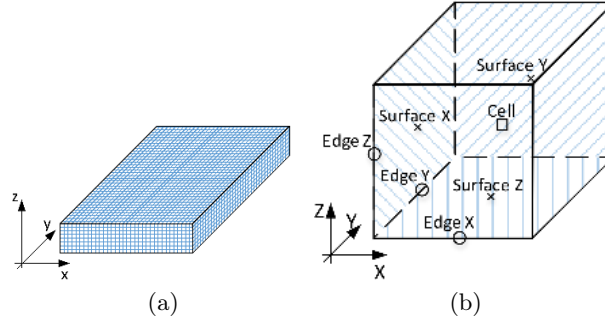


Figure 3.1: (a) The mesh inside the modelling sample after discretization. (b) The cell with all elements such as surfaces and edges of type (X, Y, Z) . J_x , J_y and J_z are assumed constant in surface X, Y, Z , respectively. The same applies for T_x , T_y and T_z for edges X, Y, Z .

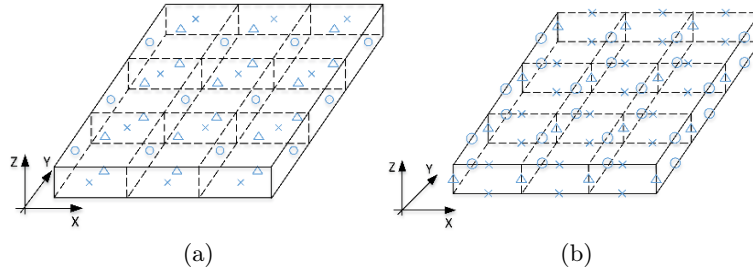


Figure 3.2: The mesh elements inside the sample volume. The discretization creates (a) 3 kinds of surfaces (X, Y, Z) and (b) 3 kinds of the edges (X, Y, Z) .

the applied vector potential at surface type s and index i . We can set all components of the average vector potential, a_{sij} , as the interaction matrix.

3.3 Thin film approximation and stacks of many tapes

Second generation HTS superconducting tapes are produced as thin films. In addition, thin films such as REBCO are used in RF cavities and electronics, in order to drastically improve their properties. Therefore, a thin film model is very useful and necessary to explain all effects. The thin film model contains only one layer of cells in the thickness, and hence the current can flow only in the z plane with J_x and J_y components. The missing J_z component and the fact that no current crosses the sample surface reduces $\mathbf{T} = (T_x, T_y, T_z)$ to only the T_z component, since the tangential component of \mathbf{T} at the sample boundary vanishes. The reduced number of state variables speeds up the calculation time.

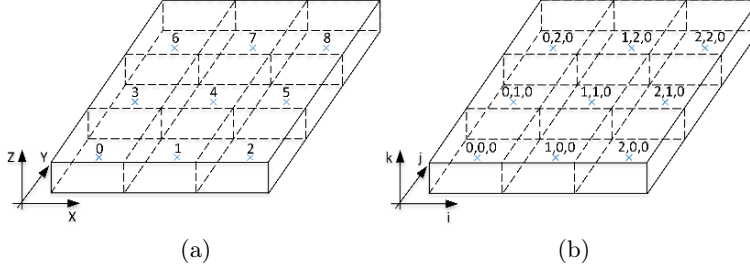


Figure 3.3: The cells address by (a) sequence order and by (b) coordinate system with (i, j, k) indexes.

The stack of tapes is a potential alternative to superconducting bulks. The screening current path is still not clear, since a non-insulated stack could contain coupling current in the metal stabilization or solder connecting tapes. For stacks of insulated tape, we can assume the approximation that the model contains only J_x and J_y components like the uncoupled case, which is a homogeneous bulk approximation. The homogeneous bulk approximation contains only the T_z component, and hence the calculation time is again reduced by reduction of the unknown variables.

3.4 Current lines

The current lines are important, in order to see the current direction in any geometry of the sample. The current lines by definition, follow the direction of \mathbf{J} and the separation between lines is inversely proportional to $|\mathbf{J}|$. The colour maps in this thesis contain current lines calculated by two ways: for 2D and 3D case.

The 2D model is the thin film approximation, and hence it contains only a T_z non-zero component (section 3.3). The effective magnetization is defined as $\nabla \times \mathbf{T} = \mathbf{J}$ and for thin film case it becomes $\mathbf{J} = \frac{\partial T_z}{\partial y} \mathbf{e}_x - \frac{\partial T_z}{\partial x} \mathbf{e}_y$.

In thin films, the level curves of T_z , are the current lines. This can be seen as follows. ∇T_z is perpendicular to the level curves of T_z . The $\nabla T_z \times \mathbf{e}_z$ is tangent to the level curves of T_z and it follows the level curve line. Since $T_z \times \mathbf{e}_z = \mathbf{J}$ the level curves of T_z follow the current density direction. The separation between level curves of T_z is inversely proportional to $|\nabla T_z|$. Since $|\nabla T_z| = |\mathbf{J}|$, the separation between level curves is inversely proportional to $|\mathbf{J}|$.

The 3D case cannot assume level curves of \mathbf{T} , since \mathbf{T} contains all three components in the 3D space, and hence the numerical method is used. The 3D numerical method for plotting current lines set the initial point in the space and calculates the unit vector of the current density at that point. Other points follows the current direction separated by a small distance

and make a line until they close the loop. This method is more general, but requires a small separation between points. The reason is that a large separation can create a current line loop that does not close due to imprecise unit vector.

3.5 Minimization

Minimization is the main part of the solver. The minimization algorithm is developed especially for this kind of problem. The minimization solves the functional (section 3.1) by looking for its minimum value through the variables in the mesh (section 3.2).

Before the minimization starts, other sub-routines calculate the applied vector potential \mathbf{A}_a (section 2.8) on the surfaces according to the applied magnetic field B_a , instant time t and time step i_t . The change in one time step of the variables inside the mesh, such as effective magnetization $\Delta\mathbf{T}$ at edges, current density $\Delta\mathbf{J}$ and vector potential $\Delta\mathbf{A}$ at the surfaces, are initialized to zero.

3.5.1 Evaluation of \mathbf{J} and \mathbf{A}

Once ΔT is known at all edges, we evaluate the current density \mathbf{J} , vector potential \mathbf{A} in the surfaces and dissipation factor U in the cells (figure 3.6). The current density is calculated via

$$\Delta J_z = \oint \frac{\Delta\mathbf{T} \cdot d\mathbf{l}}{S_z}, \quad (3.27)$$

where the integral is done on the edge of the elementary surface where ΔJ_z is evaluated. The sum of the close loop integral is then

$$\begin{aligned} S_{z,i,j,k} J_{z,(i,j,k)} &= l_{x,(i,j,k)} T_{x,(i,j,k)} + l_{y,(i+1,j,k)} T_{y,(i+1,j,k)} \\ &- l_{x,(i,j+1,k)} T_{x,(i,j+1,k)} - l_{y,(i,j,k)} T_{y,(i,j,k)}, \end{aligned} \quad (3.28)$$

where i, j, k are the indexes of the elements [figure 3.4]. The components ΔJ_x and ΔJ_y are found in the same way.

The vector potential is calculated by

$$\Delta\mathbf{A}(\mathbf{r}) = \frac{\mu_0}{4\pi} \int \frac{\Delta\mathbf{J}(\mathbf{r}')}{|\mathbf{r} - \mathbf{r}'|} d\mathbf{r}'. \quad (3.29)$$

Then, one component of the vector potential is

$$\Delta A_{xi}(\mathbf{r}) = \frac{\mu_0}{4\pi} \int \frac{\Delta J_{xi}(\mathbf{r}')}{|\mathbf{r} - \mathbf{r}'|} d\mathbf{r}', \quad (3.30)$$

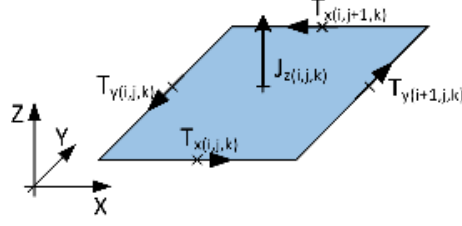


Figure 3.4: A Z -surface with uniform current density component J_z with index address (i, j, k) and neighbour edges with appropriate index addresses. T along the edge is assumed uniform.

The numerical evaluation of the s component of the vector potential due to ΔJ_s is

$$\Delta A_{si} = \int dV A_s(\mathbf{r}) h_{si}(\mathbf{r}) = \sum_{j=1}^{n_s} V_{sj} \Delta J_{sj} \Delta a_{sij}. \quad (3.31)$$

The average vector potential for the interaction matrix is [see section 3.9 and equation (3.26)]

$$a_{sij} = \frac{\mu_0}{4\pi V_{si} V_{sj}} \int_V d^3 r \int_V d^3 r' \frac{h_{si}(r) h_{sj}(r')}{|\mathbf{r} - \mathbf{r}'|}, \quad (3.32)$$

where V_{si}, V_{sj} is volume of influence of surface s with index i and j [equation (3.35)], \mathbf{r} and \mathbf{r}' are vector positions of the surfaces i, j , and $h_{si}(\mathbf{r}), h_{sj}(\mathbf{r})$ are the interpolation functions of figure 3.17.

3.5.2 Minimization algorithm

The following minimization algorithm explains the whole method on the 2D film case, which contains only the T_z component. The minimization block diagram is on figure 3.5. However, the same algorithm applies for all 3 components (T_x, T_y, T_z) in the 3D case.

The program calculates the change in the functional due to a change of δT and $-\delta T$ at the first edge of type Z , Z_1 . At the beginning, we start with a δT value according to the current density J_c and the dimensions of the elements

$$\delta T = J_c \frac{S_x}{l_z}, \quad (3.33)$$

where S_x is the surface area of the surface X and l_z is the length of the edge Z . For uniform mesh, δT creates current density equal the J_c value. The other variables are not updated due to change of δT in the edge Z_1 . The sub-routine takes the second edge Z_2 and finds the value of the functional for it. The algorithm continues until all edges Z are tested. Next, the program chooses the edge Z_m that minimizes the functional the most. The algorithm

sets the new value at the edge Z_m and updates all variables inside the whole mesh. The minimization restarts again looking for the other edge Z_m in the mesh, which minimizes the most the functional. The procedure repeats until there is no edge Z_m that reduces the value of the functional.

The solution of \mathbf{T} distribution in the sample is coarse. For this reason, δT is divided by factor 10, in order to find a finer \mathbf{T} solution. The minimization algorithm starts again looking for all edges Z , which minimizes the functional. The sub-sequent decrease of δT and minimization is repeated up to the tolerance of J , which is set in the input file (section 9).

The final solution of \mathbf{T} distribution and all variables are saved into the output files for the present time step i_t and variables $\Delta\mathbf{T}, \Delta\mathbf{J}, \Delta\mathbf{A}$ are added to the values of the ones at the previous time step, $\mathbf{T}_0, \mathbf{J}_0, \mathbf{A}_0$. Then, the values $\Delta\mathbf{T}, \Delta\mathbf{J}, \Delta\mathbf{A}$ are set to zero and the applied vector potential \mathbf{A}_a is recalculated to the values according to the next time step i_t . The minimization looks for a solution for each time step i_t one by one. The minimization algorithm uses the same sub-routines for the mesh splits into sectors (section 3.6). However, each sector contains a relatively small number of elements, and hence the minimization is very fast.

3.6 Sectors

The 3D modelling tool has to handle a huge number of elements, and hence a fast calculation method is necessary. The minimization with sectors [100,101] speeds up the computation time (see the end of this section). The computing time for minimization increases with the second power of the total numbers elements (section 3.8.4).

The entire sample is split into many smaller sectors [figure 3.8(a)] that contain a relatively small number of elements, and hence the minimization of each sector is very fast. The minimization is looking for \mathbf{T} values at the cell's edges (section 3.5). Therefore, the boundaries between sectors are set at the edges. One sector with all boundary conditions is on figure 3.7. The thin film model is with one cell in thickness and hence only T_z component is with non-zero value. The sector in this example contains 3×3 cells and 4×4 edges. However, we found that the optimum value for the calculations is $12 \times 12 \times 1$ cells in each sector in the 2D case and $9 \times 9 \times 9$ cells in the 3D case. There are three conditions for T_z edges in blue on figure 3.7. The current density outside the sample is zero and there is no surface current density, and therefore T_z at the edges on the sample surface is zero. The boundary edges on the sample surface are with triangles. The edges at the border between the sectors are with circles. The minimization does not minimize the sector border's edges and keeps them with the same values as before minimization. The edges with a cross change values during the minimization. There are 3 sets of sectors, in order to solve the edges at

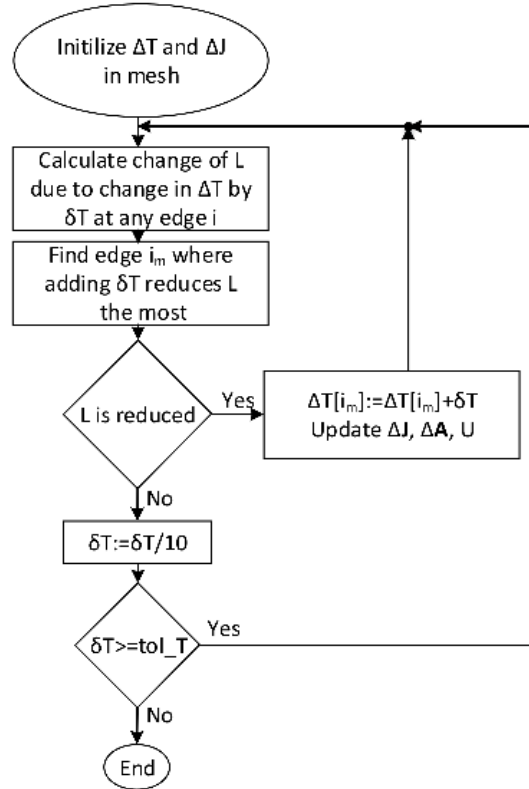


Figure 3.5: The simplified minimization block diagram for a thin film with only T_z component. For a bulk as a full 3D object, the minimization diagram is the same with all \mathbf{T} components. The minimization routine is developed for MEMEP 3D modelling tool.

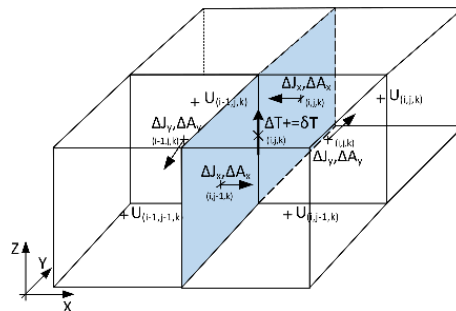


Figure 3.6: The change of variable ΔT in Z -edge $Z_{(i,j,k)}$ creates a change in the variables $\Delta \mathbf{J}, U, \Delta \mathbf{A}$ in the shown neighbour surfaces and cells.

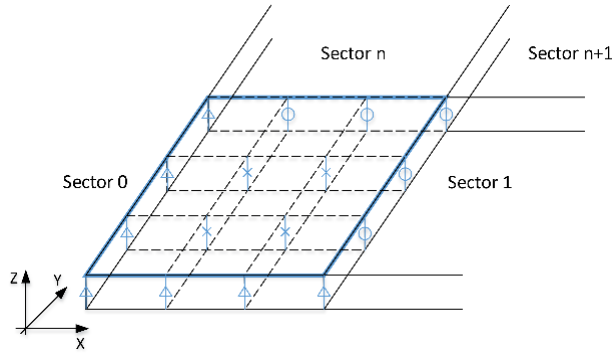


Figure 3.7: The boundary conditions at the edges inside a sector on the sample boundary. The edges on the sample surface are with triangles, edges at the sector border are with circles, and edges inside the sector without any restrictions are with crosses.

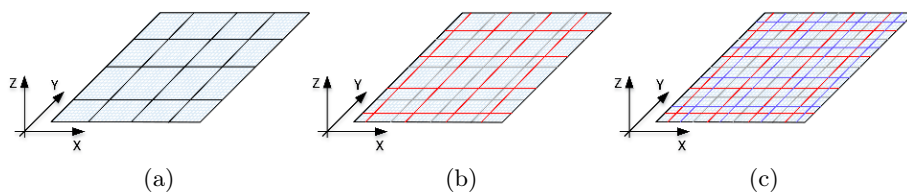


Figure 3.8: The sectors distribution in the sample. (a) The first set of sectors (black lines). (b) The second set of sectors (red lines) is with $1/3$ diagonal shift compared to Sector set 1. (c) The third set of sectors (blue lines) is with $2/3$ diagonal shift compared to the Sector set 1. The sets of sectors drastically reduce the minimization time.

all the borders, which the minimization sub-routine keeps as constant. The second set of sectors contains sectors with the same boundary conditions as the first set, but the sectors position is shifted by $1/3$ of the sector size [figure 3.8(b)]. The third set of sectors shift all sector positions by $2/3$ of sector size [figure 3.8(c)]. Therefore, the border edges from the first set of sectors are solved in the second or third set of sectors, and opposite.

The three sets of sectors speed up minimization time compared to the minimization without the sectors (section 3.8.4). The total computing time of one iteration without any speed up method is $t = a \cdot n_{cx}^6$, where a is certain constant factor and n_{cx} is the number of cells along one side of the 3D cube sample. Then, the total computing time t_s of one iteration by sectors is $t_s = a \cdot n_{cx}^6 \cdot 3/n_s^3$, where n_s is the number of sectors per one edge of the cube and multiplied by factor 3, since the mesh contains 3 sets of the sectors. The reduction factor can be defined as t/t_s and is equal to $n_s^3/3$. Therefore, the total theoretical speed up factor by sectors is $S/3$, where S is the total number of sectors n_s^3 .

One disadvantage of the sector method is that each set of sectors increase the usage of the memory RAM, since the minimization requires all interaction matrices. However the total memory usage is small, a few Gbs, and hence an increase of 3 times is still low compared to the available RAM memory (64 GB) in the computer cluster. The required RAM memory is low thanks to the uniform mesh. For this case, the independent entries of the interaction matrix can be drastically reduced, since it only depends on the difference of the addresses between two surfaces $(i_1 - i_2, j_1 - j_2, k_1 - k_2)$, where (i_1, j_1, k_1) and (i_2, j_2, k_2) are the addresses of two arbitrary surfaces.

3.7 Symmetry

The symmetry method reduces calculation time further. The simple modelling example of \mathbf{T} in magnetizing a thin film is on figure 3.9. The modelling case contains homogeneous distribution of critical current density J_c and power law n value, and hence there exist symmetry in the \mathbf{T} solution. The solution presents mirror symmetry with respect to the x and y axis with origin at the sample center. The independent fourth of the sample is set as the quadrant at the left-bottom corner [figure 3.11(a)]. The solution at the other quadrants is found from the independent quadrant by mirror symmetry. The same method applies for the 3D case. The cube mesh is split into 8 octants and the independent one mirrors the \mathbf{T} values into the remaining octants according to the x, y, z axes lines [figure 3.11(b)]. The symmetry can be exploited only when the applied magnetic field is perpendicular to any of sample surfaces.

The code implements symmetry only in case of an applied field angle of $\theta = 0^\circ$. The sub-routines in the code minimize \mathbf{T} in the sectors of the inde-

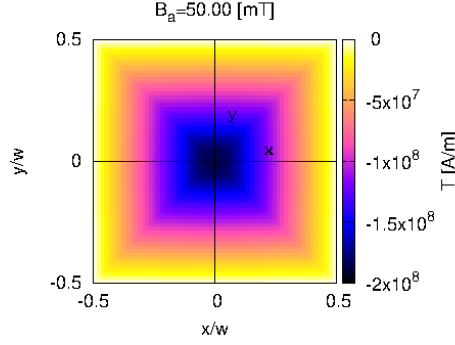


Figure 3.9: The \mathbf{T} distribution in the thin film with 50 mT perpendicular applied field and critical current density $3 \cdot 10^{10}$ A/m² and n value 30. The $x - y$ mirror lines are with origin at 0,0. Ideally, symmetry reduces the minimization time to 1/4.

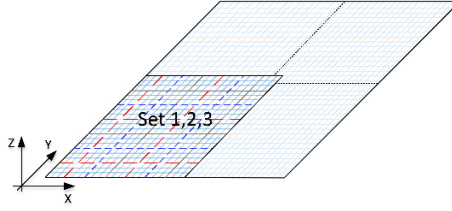


Figure 3.10: The three Sets of sectors in the first quadrant overlap the mirror lines x, y , and hence it does not reach ideal speed up time.

pendent quadrant and the symmetry reduces the number of sectors 4 times in 2D case and 8 times in 3D case. The sectors in the independent quadrant have to be with full size, and hence sectors in various sets overlap the mirror planes (figure 3.10). Therefore, the number of sectors is not reduced as much as factor 4 (2D case) or 8 (3D case), and hence the minimization time speeds up only 3-3.5 times (2D) and 6-7.5 times (3D). The speed up factor increases with the number of sectors. The \mathbf{T} solution after each iteration of the independent quadrant is copied into the other quadrants. The sub-routines are in the recalculation block in the code structure diagram (figure 3.12), in order to evaluate $\mathbf{J}, U, \mathbf{A}, \mathbf{B}$ in the entire sample (block "Recalc. $\mathbf{J}, U, \mathbf{A}, \mathbf{B}$ " in figure 3.12). The evaluation of current density and dissipation factor is fast. The evaluation of \mathbf{A} and \mathbf{B} is time consuming, scaling as the square of the total number of cells. However, constant J_c requires the evaluation of \mathbf{B} only at the end of each time step i_t . The minimization requires evaluation of \mathbf{A} in the independent quadrant only, and hence further speed up of the calculation time is possible. The code contains all possible combinations of input options (section 9).

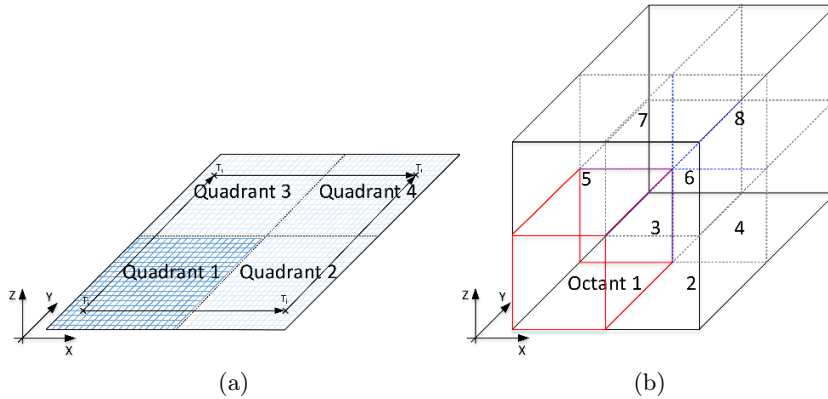


Figure 3.11: The symmetry in (a) thin film and (b) cube reduces sectors into the first quadrant in 2D case and octant in the 3D case.

3.8 Parallel programming

The 3D modelling tool is dealing with a huge number of degrees of freedom, and hence calculation time is an important feature for any calculation method. The calculation tool of any physical case with computing time of a several weeks is not feasible. The modelling case often needs to adapt according to the requirements with a slight change in an input parameters, and hence the final results will take several months if not optimized. The tool can be sped up numerically as it is explained in previous sections 3.5, 3.6, 3.7 or by parallel programming in the code itself. The modelling tool is written in C++ [102] and parallel programming is implemented by OpenMP [103] (on a single computer CPU) and BoostMPI [104] (on cluster nodes) standards.

3.8.1 Structure of the code

The MEMEP 3D modelling tool has a lot of input options, reflecting the complex code structure. This section explains the calculation steps written on around 7000 lines in C++ code. The big advantage of C++ is the possibility to organize the code by classes and objects, which are used in the program. The code is split into several main blocks. The simplified block diagram is on figure 3.12.

The user friendly input file contains all input parameters (chapter 9). The program loads the input file, calculates the mesh and creates all variables for cells, surfaces and edges. Then, it also sets the values of critical current density J_c and power law exponent n in the cells.

The most optimization complex calculation are the interaction matrices for the vector potential \mathbf{A} , and magnetic field \mathbf{H} . The non-uniform mesh with total number of cells 70000 requires full interaction matrix of size around 117

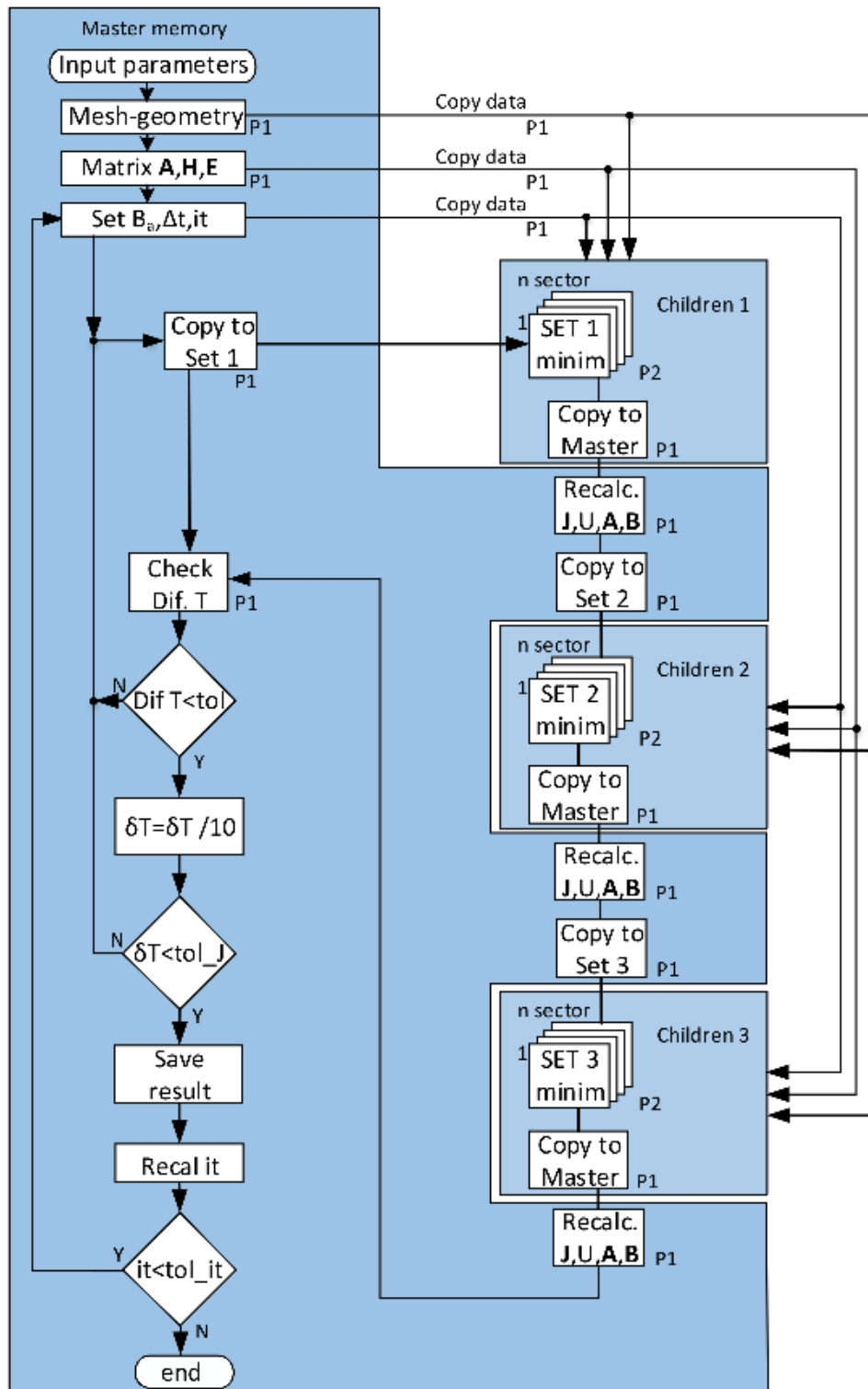


Figure 3.12: The simplified block diagram of the code structure. The highly parallelized code structure exploits the C++ object-based properties to create “children” object from a “parent”. P_1 and P_2 is the type of parallel calculation (section 3.8.2) and n is the number of sector.

GB RAM memory. The interaction matrix for uniform mesh depends on the relative distance, and hence the matrix can be reduced to a few MB of RAM.

The initialization sub-routine sets the applied magnetic field with angle θ , the current time t , time step Δt and number of time steps. All the previous data is saved in the memory in a "parent" object. Later, the program copies all mesh and parameter data to "children" objects, where the minimization is done. The flow of data is shown on figure 3.12. Each "children" object contains one of the 3 sets of sectors (section 3.6). Next, follows the main minimization part of the code. \mathbf{T} is solved in the first set of sectors by minimizing the functional in each sector in parallel. Then, the solution of \mathbf{T} is copied to the "parent" object, where all side variables are re-calculated, such as the dissipation factor U , the vector potential \mathbf{A} , the magnetic field \mathbf{B} , the current density \mathbf{J} or the critical current density J_c ; according to the chosen dependence in the input file.

Afterwards, the data moves into the second "children" object, where minimization finds the new solution for the second set of sectors. The sub-routines again copy the solution into the "parent" object and recalculate the side variables. Next, the third set of sectors receives the data from the "parent" and finds the solution for the last time. The data moves into the "parent" and recalculates all necessary variables.

The solution from all 3 sets is compared with the solution of the previous iteration step by finding the maximum difference in \mathbf{T} at each edge. If the difference is higher than the chosen tolerance, the entire iteration procedure is repeated. If the difference is lower than δT (explained in section 3.5), δT is divided by factor 10 and the iteration starts again. The iterations stop only if δT is below the certain input current density of tolerance d_J . The final solution of the present time is saved into output files. Finally, a new time step and applied field is set. The new time step starts the entire minimization process in order to find a new solution. The code calculates all time steps and saves them into the output files.

3.8.2 Parallel programming in one computer by OpenMP

Parallel programming by OpenMP speeds up the calculation time by using all cores or threads in the computer. Nowadays, computers have several threads (for instance, 8 threads in affordable Intel i7 4000 series processors), reaching 40-60 or more threads in powerful workstations. Then, parallel programming could be speed up as many times as the number of threads.

There are two ways of parallel computing, which are used in the code. The first way can be used in each loop "for" with a lot of iterations. The simple loop example is

```
#pragma omp parallel for private(n) num-threads(i)
for(n=0;n<x;n++) {a[n]=n;}
```

puts the n value to the vector a of size x . The OpenMP commands starts with “`#pragma omp parallel for`”, which is dedicated for loop “`for`”. The private variables means that each thread will create its own variable and it does not override the value between threads. Num-threads sets the number of required threads. The previous simple example will split a single master thread into many threads. The single master thread is performing calculation in series and many threads will perform the calculation in parallel and faster than with only one thread. The second way is used in the short loop with complex calculation such as minimization of a sector. The code example is

```
#pragma omp parallel for private(n) num-threads(i)
for(n=0;n<set1;n++) {minimization-sector(n);}
```

However, all calculation in sub-routines [below `minimization-sector(n)`] cannot contain any pragma commands. Variables cannot depend on an other sector, since the master thread is already split into many threads, each tread minimizing its own sector. If the thread finishes, the calculation on the current sector will continue with another free sector, which is not calculated.

The simplified block diagram of the code (figure 3.12) is marked with “P1” and “P2”. P1 is parallelization by the first way and P2 by the second way. The sub-routines in P2 blocks are parallelized in top level, and hence the efficiency of the parallel programming is very high. The high efficiency is because the master thread is split into many threads only once, and hence each thread is calculating its own part of the code for a relatively long time. This avoids time-consuming creation of new threads. In the code, there still exist parts calculated in series, and hence parallel programming efficiency decreases a bit. However, the code reaches very high parallel efficiency, more than 90%.

3.8.3 Parallel programming on a cluster by BoostMPI

Further speeding up the modelling tool is possible by computing on a computer cluster. Parallel programming on a computer cluster is more complex than on a single computer. The used a computer cluster in the Slovak Academy of Sciences (picture 3.14) that contains 52 nodes of IBM dx 360 M3 and each node contains 12 cores (12 threads). Parallel programming in clusters using C++ language is only supported by BoostMPI protocol. The program is written with both OpenMP and BoostMPI protocols, and hence it can use all nodes in the cluster and all cores available per node.

The simplified block diagram of the code for three nodes is on figure 3.13. The compiler file contains all input parameters for the cluster, such as number of nodes, number of cores per node and the code file. The cluster terminal loads the code into the nodes and each node performs the same code. The structure of the code is similar to that on figure 3.12. Each node

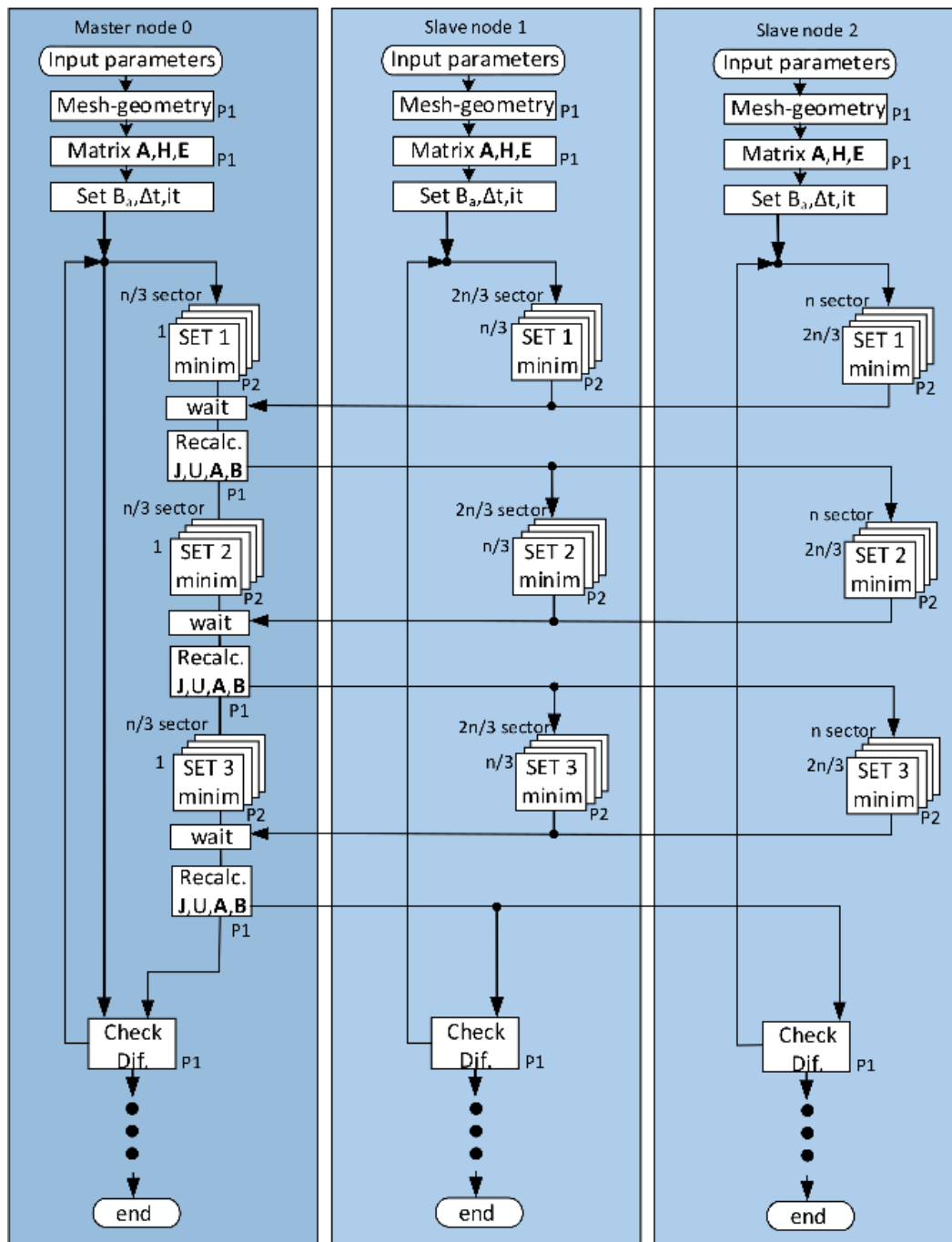


Figure 3.13: The simplified block diagram of the code structure with Boost-MPI hierarchy for 3 nodes, where n is the number of sectors. Time consuming data transfer between nodes is minimized, and hence parallel code efficiency is high.



Figure 3.14: Slovak Academy of Science - Institute of informatics HPC Cluster with 52 x nodes of IBM dx360 M3.

loads an identical input file and calculates the mesh and interaction matrices, in order to avoid unnecessary data exchange between nodes, which reduces parallel computing efficiency. One node is dedicated as “master” node and the remaining nodes are “slaves”. The calculation is performed by all cores in each node separately. The parallel computing by OpenMP commands is marked by “P1” and “P2” as it is explained in previous section 3.8.2. Each node contains the appropriate $1/n_n$ number of sectors for each set of sectors, where n_n is the number of nodes. The minimization sub-routines of the sectors calculate for each node in parallel and separately. The result of \mathbf{T} is copied into the master node by BoostMPI commands (send, received). The master node waits until all data is received from all nodes and then it evaluates variables $\mathbf{J}, U, \mathbf{A}, \mathbf{B}$. The evaluated variables in the master node are sent back to the other nodes, and then minimization of the second set of sectors continues. The same process of the exchange of data between master node and other nodes continues until all 3 sets are solved. The master node collects, evaluates, and finally broadcasts all data for the last time. Each node decides to either continue with another iteration or not as it is explained in section 3.8.1

The example on figure 3.13 uses 3 nodes, and hence the theoretical speed up of the calculation time is 3 times. The process of the exchange of data decreases parallel efficiency of the code, because the nodes are not calculating until all data are completely received or sent. The symmetric distribution of calculation tasks on each node is very important, in order to secure the synchronicity of the redistribution of the data and decrease time of not calculating nodes. However, the parallel programming efficiency is very high, around 90%. The block diagram (figure 3.13) is simplified. Actually, the evaluation of variables such as \mathbf{B} and \mathbf{A} is calculated by all nodes, in order to speed up calculation time further. The entire code contains around 7000

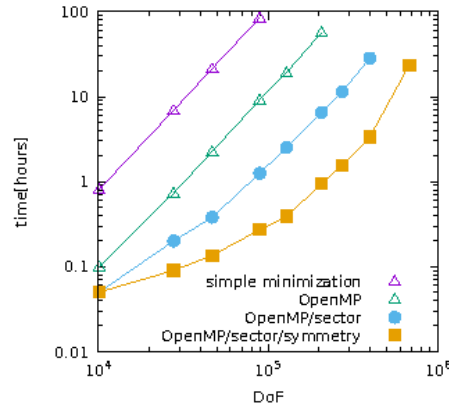


Figure 3.15: The calculation time of the MEMEP 3D modelling tool with increasing number of degrees of freedom and various sped up methods on a single standard computer. The model case is a cube with perpendicular applied field parallel to z axis and 10 time steps, in order to reach the peak of the applied field of 200 mT. The DoF for symmetry corresponds to the full sample.

lines and more than 250 sub-routines.

3.8.4 Computation time

In conclusion, the modelling tool reaches fast calculation time. All the methods to speed up the calculation time according to the previous sections are implemented in the C++ code. The example case with various number of degrees of freedom shows the calculation time dependence of the modelling tool. The modelling situation is a simple cube magnetization with the applied magnetic field of 200 mT parallel to the z axes and critical current density $1 \cdot 10^8$ A/m². The current density tolerance is $1 \cdot 10^{-3} J_c$. The MEMEP 3D method calculates 10 time steps until the model reaches the peak of applied field.

We study the effect on the computing time by increasing the total number of cells after each code improvement (3.15). The mesh starts with $15 \times 15 \times 15$ (3375) cells and raises up to $61 \times 61 \times 61$ (226981) cells, which is around 680000 Degrees of Freedom DoF. The calculations are performed on one node of the computer cluster, which is similar to a desk-top computer with Intel core i7-4771 CPU@8x3.5Ghz. The pure minimization without any speed up method can calculate 90000 degrees of freedom (30000) cells in less than 100 hours. The parallel programming by OpenMP protocol speeds up the calculation time around 10 times, since the cluster node contains 12 cores and parallel efficiency is around 90%. The other method improvement is by using sectors (section 3.6). The sectors speed up the calculation time by almost

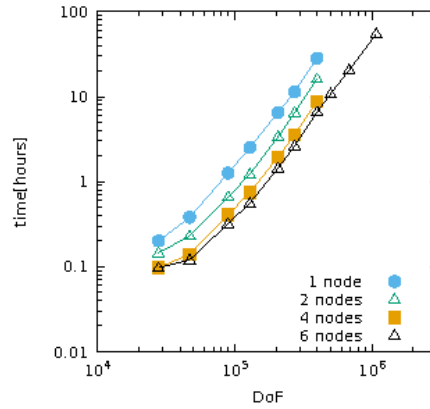


Figure 3.16: The computing time of MEMEP 3D method on the computer cluster. The reduction of the computing time increases with number of nodes. However, the efficiency of parallelization decreases by many nodes.

8.5 times. The sectors efficiency increase with the number of sectors and with the number of elements. The other method to decrease the calculation time is symmetry (section 3.7). The symmetry reduces computation time 7.5 times and its efficiency increases with the number of elements. For symmetry, the ideal theoretical speed factor for the 3D case is 8 times. In conclusion, we are able to reduce the entire computing time by two and three orders of magnitude on one computer for the routines without and with symmetry, respectively. The calculation time of $31 \times 31 \times 31$ (29791) cells (90000 DoF) reduces from 90 hours to less than 20 minutes with symmetry.

Parallel programming by BoostMPI protocol on the computer cluster reduces the calculation time further. The previous methods speed up the calculation time many times, and hence the computing tasks for the cluster are not heavy and parallel programming efficiency on the cluster is low. In order to use the cluster effectively, we did not use symmetry, which cannot be used for all modelling cases. The same modelling example as for one computer is used for the study of the computing time on a cluster. The calculation time as a function of the degrees of freedom is on figure 3.16. The increase of the total number of elements (or DoF) increases the efficiency of the parallel computing. For very low total number of cells, the dominant calculation time is data transfer between nodes, which is negligible for high numbers of cells. The calculation time speeds up on 2 nodes by factor 1.75, on 4 nodes by factor 3.23 and be 6 nodes 4.31 times for 397953 DoF. However, the 6 nodes of the cluster allows us to model the sample with more than 1 million of DoF in less than 55 hours (figure 3.16). The reason for low efficiency with increased number of the nodes is that the computing load of each node is small and data transfer between nodes starts to be dominant. The efficiency can be improved by further increase of the total number of

cells. The efficiency, of the parallel computing on the cluster is more than 80% for the present range of the number of cells in the mesh. Further advanced modelling by MEMEP 3D method will require higher number of cells in the mesh, and hence the parallel computing efficiency will increase.

3.9 Elongated cells

Elongated cells in the mesh enables to model long samples without any further increase in the total number of elements or reduction of the number of elements. The reduction of the number of elements speeds up the computation time of the modelling tool. The modelling sample geometry with elongated cells plays an important role for long thin films (2D) and long bars (3D).

The interaction matrix for non-elongated cells is calculated by two formulas. The vector potential is evaluated in the surface elements (section 3.2). Therefore, the criterion to choose between formulas is according to the surface positions. The general definition of vector-potential interaction matrix is

$$a_{sij} = \frac{\mu_0}{4\pi V_{si} V_{sj}} \int_V d^3r \int_V d^3r' \frac{h_{si}(r) h_{sj}(r')}{|\mathbf{r} - \mathbf{r}'|}, \quad (3.34)$$

where s is the type of surface $s \in (x, y, z)$; i, j are surface indexes; V_{si}, V_{sj} are volumes of influence; $h_{si}(r), h_{sj}(r')$ are interpolation functions; and r, r' are vector positions of the surfaces. The interaction matrix element of (3.34) is the average vector potential created by the s -surface j on surface i per unit current density in the j surface. The volume of influence is calculated as

$$V_{si} \equiv \int_{V_{si}} d^3r h_{si}(r), \quad (3.35)$$

where the linear interpolation function of first-order is on figure 3.17(b). The self-interaction of two surfaces $i = j$ uses the following approximation, which is analytical

$$a_{sii} = \frac{\mu_0}{4\pi V_{si}^2} \int_{V_{si}} d^3r \int_{V_{si}} d^3r' \frac{1}{|\mathbf{r} - \mathbf{r}'|}. \quad (3.36)$$

The full length of the analytical expressions is in appendix 8.1. For cubic or 2D square cells and $i \neq j$ we can use the approximation

$$a_{sij} \approx \frac{\mu_0}{4\pi |\mathbf{r} - \mathbf{r}'|}. \quad (3.37)$$

For elongated cells, we need to use sub-elements, as it is shown on figure 3.17(a-bottom). The number of sub-elements increases until the sub-elements are as square as possible, in order to increase the accuracy of the

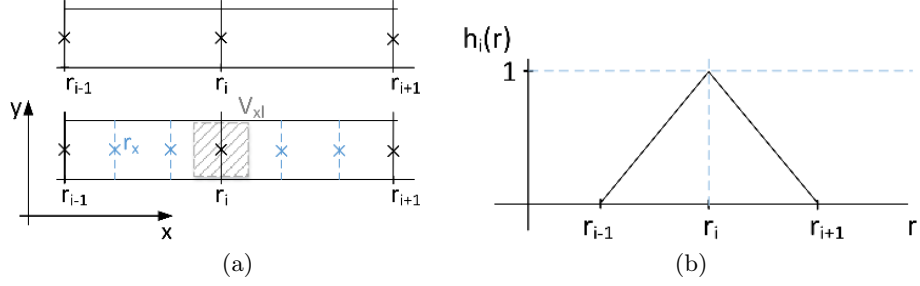


Figure 3.17: (a) Elongated cells (top) with surface positions r_{i-1}, r_i, r_{i+1} . The elongated cells are divided into sub-elements (bottom). (b) $h_i(r)$ is a linear interpolation function with value 1 at surface r_i and 0 at the surrounding surfaces r_{i-1}, r_{i+1} .

numerical calculation of the average vector potential. The general equation for two sub-elements l, m of surfaces i, j is

$$a_{sijlm} = \frac{\mu_0}{4\pi V_{sl} V_{sm}} \int_{V_{sl}} d^3 r \int_{V_{sm}} d^3 r' \frac{h_{si}(r_{sl}) h_{sj}(r'_{sm})}{|\mathbf{r}_{sl} - \mathbf{r}'_{sm}|}. \quad (3.38)$$

where V_{sl}, V_{sm} are the volume of influence of sub-elements l and m , as defined in figure 3.17 (a-bottom). The case of overlapping sub-elements $l = m$ uses the analytical formula

$$a_{sijll} = \frac{\mu_0 h_{si}(r_{sl}) h_{sj}(r_{sl})}{4\pi V_{sl}^2} \int_{V_{sl}} d^3 r \int_{V_{sl}} d^3 r' \frac{1}{|\mathbf{r}_{sl} - \mathbf{r}'_{sl}|} \quad (3.39)$$

with full expression in appendix 8.1. The sub-elements with position $l \neq m$ use the approximated formula

$$a_{sijlm} \approx \frac{\mu_0 h_{si}(r_{sl}) h_{sj}(r_{sm})}{4\pi |\mathbf{r}_{sl} - \mathbf{r}'_{sm}|}. \quad (3.40)$$

Chapter 4

Experimental method and samples

The experimental measurements of AC loss further verify the modelling method. The discussion of comparison between measurements and model is in section 5.4.2. In addition, the measurements are important by themselves, since they provide information on the real samples. Here, the measurement set-up is introduced with a following part about preparation of samples.

The AC loss is an important parameter in any superconducting tape or wire. Since AC loss increases with the tape width, the AC loss in HTS tapes under perpendicular applied field is large, because of the relatively large tape width. The striations [105] reduce hysteresis loss, since the screening current closes in narrower loops in the thinner filaments. These striations cut the superconducting layer into thinner tapes to the substrate, with or without resistive coupling. The coupled case introduces AC coupling loss, because of the present resistive material between the filaments. The coupling AC loss can be reduced by increasing the coupling resistivity up to the uncoupled case. However, the fully uncoupled case reduces the thermal stabilization of the tape, since the filaments do not share current in case of a fault in one filament. A modelling tool that can predict the AC loss with high accuracy is very demanding. The following section is dedicated to the very convenient case of AC loss measurement of two superconducting tapes soldered together and comparison with modelling results of the MEMEP 3D method.

The cross-field demagnetization of a superconducting bulk sample with a cube geometry is still not well understood. Therefore, an accurate 3D model with all finite size effects is required. We performed the same experiments as the calculation in section 6.4 with collaboration of the University of Cambridge. The measurements validate the whole method and confirms new findings of MEMEP 3D method. The test sample is prepared by the colleagues in the Superconducting Bulk Group in the University of Cam-

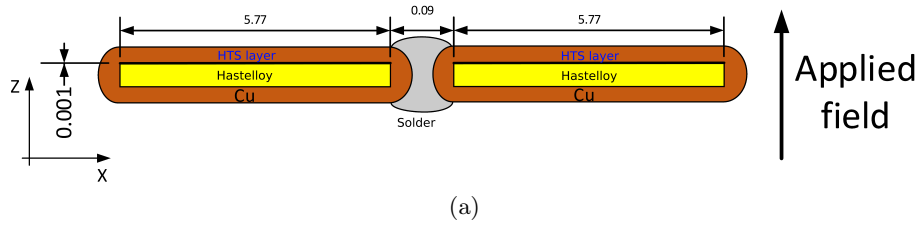


Figure 4.1: Sketch of the cross-section of the soldered sample. Dimensions are in mm.

bridge and I performed the measurement of the sample during my stay in Cambridge.

4.1 Sample of two tapes joined by normal metal for coupling effects measurements

The experimental sample consists on two superconducting tapes soldered together by indium. The superconducting commercial tape is 6 mm wide with 20 μm cooper stabilization from SuperOx [65]. The tapes are soldered side by side (figure 4.1). First, we prepared a sample of 50 mm length, and after measuring, we cut it to 22 mm length. The resistance between tapes in the sample is measured at the liquid nitrogen temperature (77 K) by electric measurements. The resistance of the 50 mm sample is 710 n Ω , while the 22 mm sample has the same conductance per unit tape length. In order to compare to the uncoupled situation, we made a second sample made of two superconducting tapes of 50 mm length placed side by side and insulated by Kapton tape.

4.2 Calibration free method for AC loss measurement

The AC loss is measured by the calibration-free method [106]. The calibration free method is a direct technique to measure AC loss. The method is based on AC power evaluation of the system by measuring voltage. The measurement method is based on series connection of two identical field coils, where the first coil is the measurement coil for inserting the sample and induce the magnetic field. The second coil is a compensation coil. The pick-up coils are identical and wound parallel and isolated within both field coil windings. The anti-series connection of pick-up coils result in no voltage signal without inserted sample. The measured voltage by pick-up coils is completely due to the sample flux $V = -\frac{d\psi}{dt}$, where ψ is the sample magnetic flux. Since the pick-up coils follow the field coils winding, the measured flux in the pick-up

4.3. CUBE SAMPLE FOR DEMAGNETIZATION BY CROSS-FIELD 63

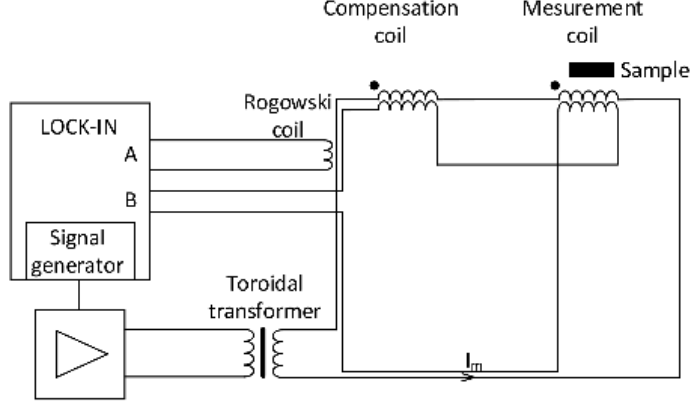


Figure 4.2: The electric scheme of the measurement set-up of the calibration free method [106].

coil is the same as in the field coil. The power provided to the field coils, in order to compensate the sample dissipation is $P = -I \frac{d\psi}{dt}$. By energy conservation, the power integrated over one cycle is the power loss of the sample.

The electric scheme is on figure 4.2. The frequency generator creates the AC signal, which is amplified in the AC amplifier and galvanically separated from the AC magnets by a toroidal transformer. The lock-in measures the voltage on the Rogowski coil induced by the magnet current I , $V_{rog} = -\omega k_{rog} \sqrt{2} I_{rms} \sin \omega t$, where k_{rog} is the Rogowsky coil constant, $I_m = \sqrt{2} I_{rms} \cos \omega t$ (channel A) and the voltage generated by the sample $V = \sqrt{2} V_{R,rms} \cos \omega t + \sqrt{2} V_{I,rms} \sin \omega t$ (channel B), and hence the AC power loss of one cycle is $Q = I_{rms} V_{I,rms} f$.

The coils are race-track coils with size of bore 140×22 mm and height 23 mm. The measurement set-up picture is on figure 4.3. There is an unbalance between coils, since they are not completely identical. The unbalance is corrected by small pick up coils. Compensation is done by position adjustment of wire until different voltage signal of both coils is zero without measurement sample [107].

The set-up provides applied field in the range of 0.1-100 mT amplitude for frequencies 72 and 144 Hz and up to 18 mT for a wider frequency range, between 2.3-1152 Hz. A double stage cryocooler allows to reach temperatures below 20 K.

4.3 Cube sample for demagnetization by cross-field

A superconducting sample pellet with diameter of 12 mm and thickness 10 mm was grown by the Top Seeded Melted Grown TSGM method [109]. The GdBCO pellet contains 10wt% of Ag. A cube was cut down from the center

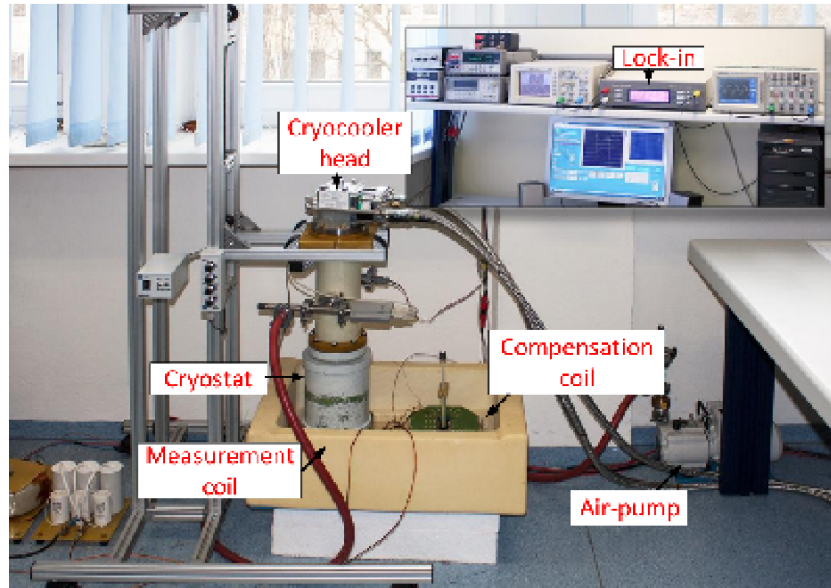


Figure 4.3: Picture of the calibration-free measurement set-up [107, 108].

of the pellet, in order to have more homogeneous sample without any cracks or inhomogeneities coming from the growth method close to the edges [109]. The cube size is $6.08 \times 6.04 \times 5.98 \text{ mm}^3$ (figure 4.4, the cube sample is inside the cylinder holder).

4.4 Measurement of bulk demagnetization by cross-fields

The measurement contains two operations. The first operation is to magnetize the sample and the second is to apply an alternating cross-field and measure demagnetization.

The cube is magnetized by the Field Cool method FC instead of the Zero Field Cool [110] or pulse method [111]. The magnetization process with resulting trapped field by ZFC (left column) and FC (right column) is on figure 4.5. The applied field is along the z axes. The ZFC method starts the magnetization process with already cooled superconducting sample and zero applied field [figure 4.5(a)]. The applied field of B_p partially [figure 4.5(b)] and with $2B_p$ fully saturates the sample [figure 4.5(c)]. At the end of the magnetization process, ramping down the field to zero, there is trapped field [figure 4.5(d)]. The FC method starts with the sample at room temperature and zero applied field [figure 4.5(a)]. The applied field is ramped up to the penetration field [figure 4.5(b)], which is followed by cooling down the sample. The sample is fully magnetized after ramping down the applied field, as shown at the profiles for $0.5B_p$ [figure 4.5(c)] and for $0B_p$ [figure 4.5(d)].

4.4. MEASUREMENT OF BULK DEMAGNETIZATION BY CROSS-FIELDS⁶⁵



Figure 4.4: The GdBCO cube sample inside a cylindrical holder.

For our case, the magnetization operation contains the following steps:

1. Ramp up the split coil electromagnet up to 1.3 T in 10 s with already inserted the bulk sample at room temperature.
2. Cool down the sample by liquid nitrogen over 15 minutes.
3. Ramp down the electromagnet with ramp rate 13 mT/s

The sample is fully magnetized along the c plane and the demagnetizing operation starts after 900 seconds of the relaxation time, with these steps:

1. Move the sample into the second coil with transverse applied field $B_{ax,max}$ up to 170 mT.
2. Apply the transverse field of various amplitudes $B_{ax,max} = B_t/2, B_t/4, B_t/8$ and frequencies 0.1, 1.0 Hz, where B_t is trapped field 100 μm above the sample surface [figure 4.7(a)].
3. Measure reduction of the trapped field by transverse field in the following 10 minutes by Hall-probe sensors.

The measuring set up is based on a lock-in amplifier that generates AC signal and measures the voltage drop on a 0.5 m Ω shunt. The lock-in output AC signal is amplified by two parallel amplifiers, to generate AC current for the coil and also the required AC magnetic field. The set up is on figure 4.6(b) and the electrical scheme is on figure 4.6(a). The Hall probe array with 7 sensors Multi-7U [112] measure the magnetic field 100 μm above the sample along the x axes (figure 4.7). The sensor array is 3.5 mm long only while the sample side is around 6 mm. Therefore, the magnetic field is not measured close to the edges of the sample.

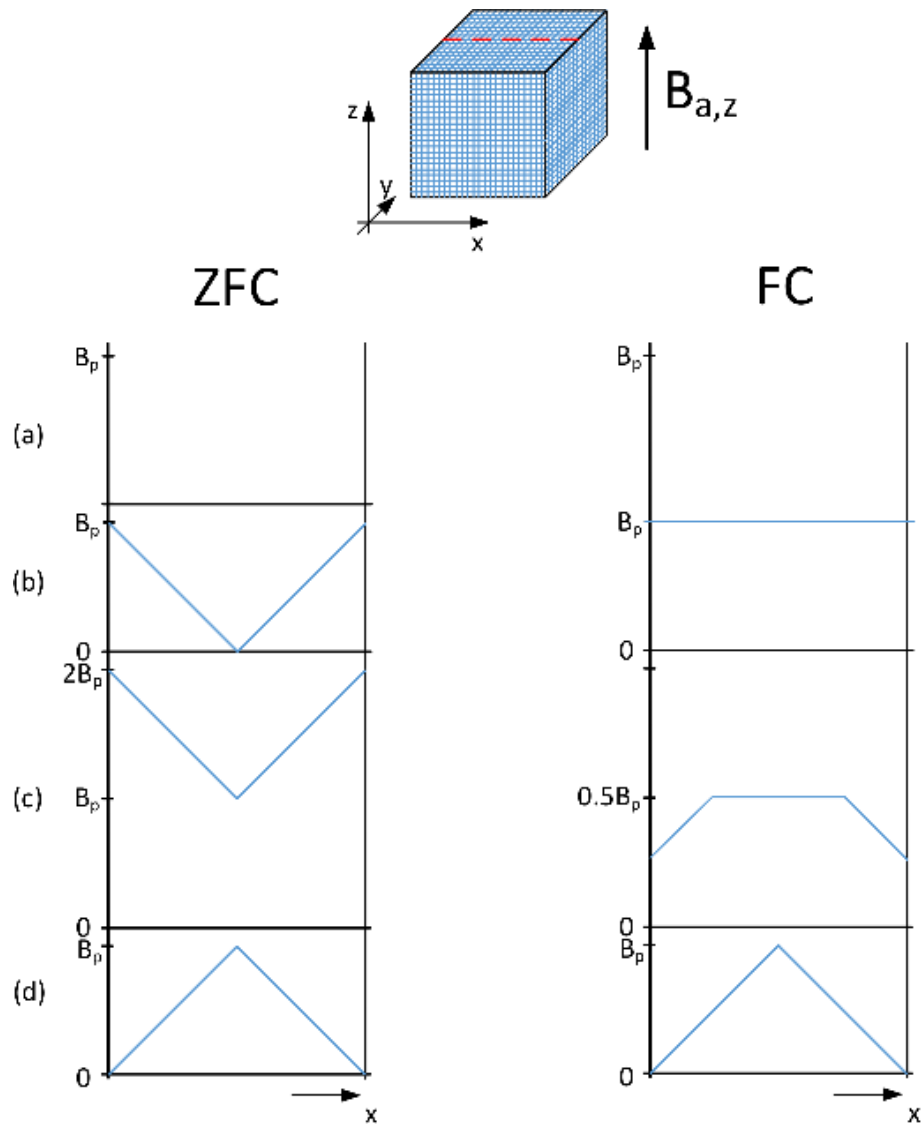


Figure 4.5: The Zero Field Cool (ZFC) and Field Cool (FC) method to magnetize a superconducting bulk sample in three steps from top to down with three applied fields of value B_p , $2B_p$ and $0B_p$ for ZFC and B_p , $0.5B_p$ and $0B_p$ for FC. B_p is the penetration field of the sample.

4.4. MEASUREMENT OF BULK DEMAGNETIZATION BY CROSS-FIELDS⁶⁷

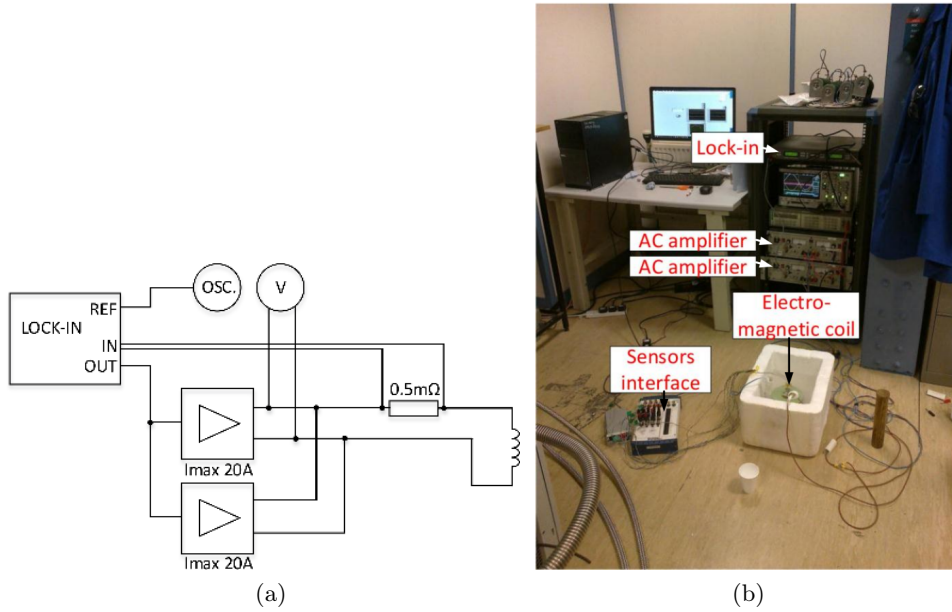


Figure 4.6: (a) The electric scheme of demagnetization measurements by cross-field. (b) The set-up measurement with electromagnetic coil.

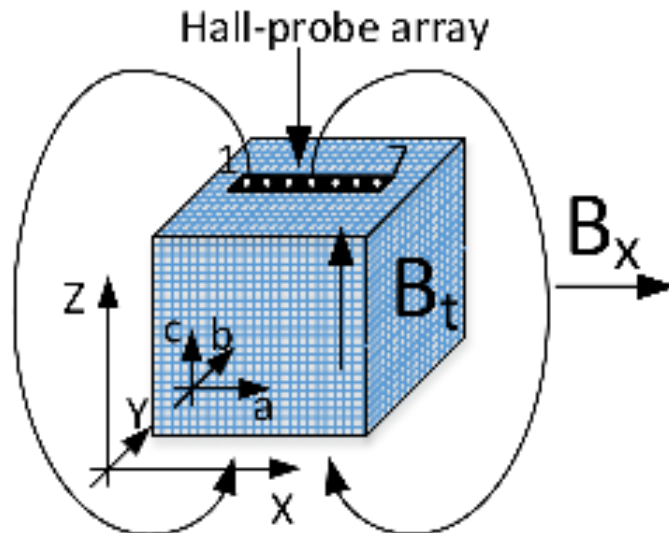


Figure 4.7: The sketch of the cross-field orientation to the sample and to the Hall probe array.

Chapter 5

Model tests and verification

Superconductors are non-linear materials. This complicates the calculation of non-linear eddy currents, resulting in high computing times (section 3.8.4). Therefore, new faster methods of calculation are required. Any new theoretical way of calculation must be validated by other methods or measurements in order to be reliable. There have been many studies of thin film models. The solution of infinite prisms by the CSM is in [113]. Analytical thin film studies of the CSM are in [1, 2, 91, 114, 115] and with isotropic power law in [13, 116]. Thin film sample with a hole and $\mathbf{E}(\mathbf{J})$ power law is [117].

The following sections contain a validation of the MEMEP 3D method. The model tests use a "thin film" geometry like a an infinitely thin sheet approximation (section 5.1) and a thin disk. We also qualitatively compare our results for a square thin film with those in [1]. The AC coupling loss of filaments joined by a normal metal are compared with measurements in the section 5.4.2.

5.1 Comparison of thin film model with analytical formulas.

The Critical State Model (CSM) is well defined for simple geometries like infinitely long thin strips and thin disks. Therefore, we model both situations in order to validate our numerical method. We have found a very good agreement for both cases, and hence we have successfully validated the method.

The first case of the long thin strip is with dimensions $4 \times 12 \times 0.001$ mm and sinusoidal perpendicular applied magnetic field with frequency 50 Hz. The sketch of the geometry is on the figure 5.1(a). The mesh is created by square elements with $107 \times 321 \times 1$ cells, which results in more than 34000 degrees of the freedom. The critical current density J_c is $2.72 \cdot 10^{10}$ A/m².

The gradual penetration of the current density is shown on figure 5.2 with current lines at the peak of the applied field of 20 mT. The current path is

changing only close to the ends of the tape, otherwise the J_y component of the current density is parallel to the y axis. The mid cross-section of the strip at the plane $y=0$ mm is on figure 5.3. The model assumes various power-law exponents like $n=1000,200,30$, in order to get results comparable with the CSM and real values of the superconducting tapes. The case of $n=1000$ is basically the same as the CSM, thanks to the high power-law exponent. The J_y component with $n=1000$ agrees very well with the thin strip analytical formula of [91,92], being at the initial magnetization curve

$$\begin{aligned} J_y(x) &= \frac{2J_c}{\pi} \arctan \frac{cx}{\sqrt{(b^2 - x^2)}}, |x| < b, \\ &= J_c \frac{x}{|x|}, b < |x| < w/2, \end{aligned} \tag{5.1}$$

where

$$b = \frac{w/2}{\cosh \frac{H_a}{H_c}}, \tag{5.2}$$

$$c = \tanh \frac{H_a}{H_c}, \tag{5.3}$$

and

$$H_c = \frac{J_c d}{\pi}. \tag{5.4}$$

Above, w is the width of the the tape, H_a is the instantaneous applied field and d is the thickness of the sample.

Real superconductors present lower n factors. The n -factor 30 is a realistic value of REBCO superconductors. In the Critical State Model, the current density never exceeds J_c but the real superconductor with $n=30$ allows higher $|\mathbf{J}|$, around 10% above J_c in our case, which figure 5.3 confirms.

The second simple geometry is a thin disk with radius $R = 6$ mm and thickness $d = 1 \mu\text{m}$ (sketch 5.1(b)). The critical current density is $2.72 \cdot 10^{10}$ A/m² and sinusoidal applied magnetic field of 50 Hz. The model takes n factor 1000. The penetration of the current density at 7.8 mT is on figure 5.4. The current path is circular according the outer shape of the sample, in spite of the fact that the applied vector potential, \mathbf{A}_a , follows the y direction (section 2.8). The J_y component at the mid cross-section (figure 5.5) agrees very well with the analytical equation (5.5). The formula in [115] for thin disk is

$$\begin{aligned} J_y(r) &= -\frac{2J_c}{\pi} \arctan \frac{\frac{r}{R} \sqrt{(R^2 - a^2)}}{\sqrt{(a^2 - r^2)}}, r < R, \\ &= -J_c, a \leq r < R, \end{aligned} \tag{5.5}$$

5.1. COMPARISON OF THIN FILM MODEL WITH ANALYTICAL FORMULAS.71

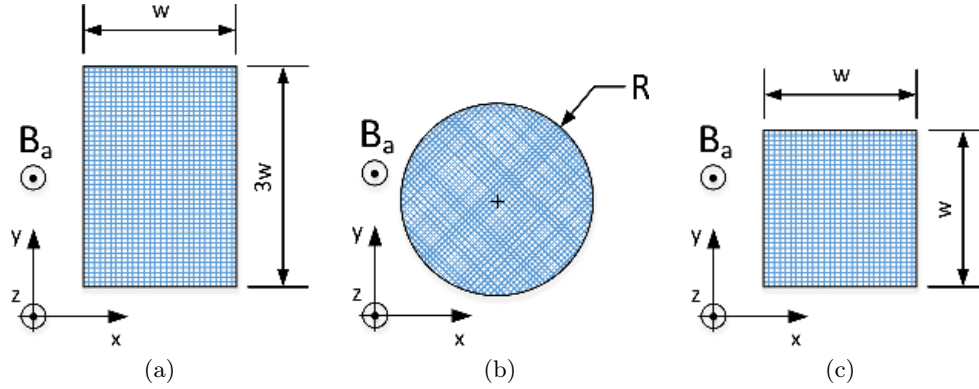


Figure 5.1: Sketch of the thin film modelling geometry (a) thin strip (b) thin disk (c) square film. The results obtained with these geometries agree with calculations with previous models.

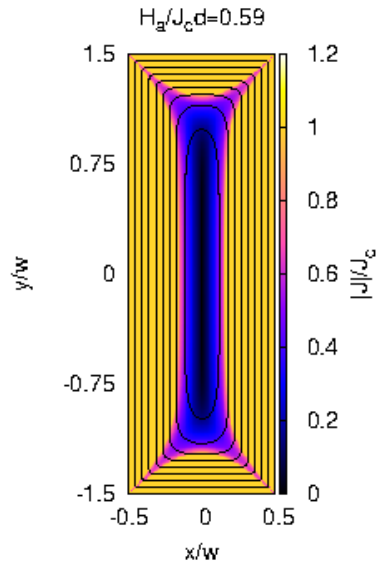


Figure 5.2: The modulus of the current density and current lines at the peak of the AC applied magnetic field 20 mT. The current lines are parallel to y axis except close to the ends of the tape.

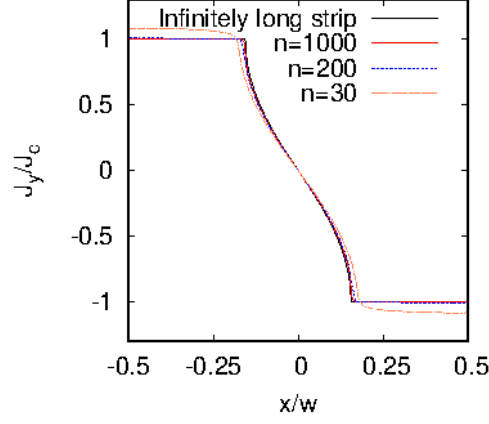


Figure 5.3: The J_y component at the mid cross-section plane $y = 0$ with various power-law exponents n 1000,200,30. The model with n 1000 agrees with the thin strip formula 5.1.

where

$$a = \frac{R}{\cosh \frac{H_a}{H_d}}, \quad (5.6)$$

and

$$H_d = \frac{J_c d}{2}. \quad (5.7)$$

The magnetization formula is split into 3 branches. The initial magnetization is

$$M_{zi}(H_a) = -\chi_0 H_a S\left(\frac{H_a}{H_d}\right), \quad (5.8)$$

where

$$\chi_0 = \frac{8R}{3\pi d} \quad (5.9)$$

and

$$S(x) = \frac{1}{2x} \left[\arccos \frac{1}{\cosh x} + \frac{\sinh x}{\cosh^2 x} \right]. \quad (5.10)$$

Then, the magnetization from positive to negative peak of the applied magnetic field and vice versa is

$$M_{z\downarrow} = M_{zi}(H_m) - 2M_{zi}\left(\frac{H_m - H_a}{2}\right) \quad (5.11)$$

and

$$M_{z\uparrow} = -M_{zi}(H_m) + 2M_{zi}\left(\frac{H_a - H_m}{2}\right), \quad (5.12)$$

where H_m is the maximum applied field. The relation between M_{zi} and $M_{z\downarrow}$, $M_{z\uparrow}$ applies also for other shapes with high symmetry, such as thin strips

5.2. FINITE-LENGTH SUPERCONDUCTING THIN FILM WITH CONSTANT J_C 73

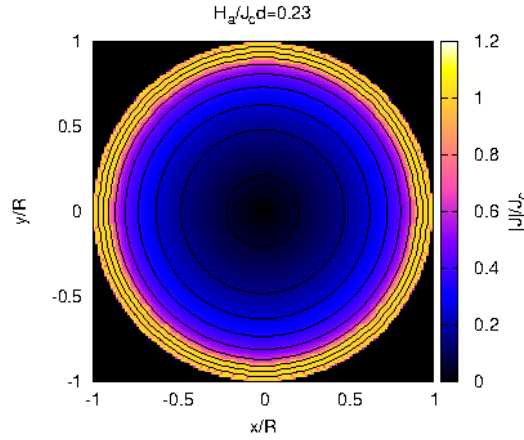


Figure 5.4: The modulus of the current density at applied field 7.8 mT for a thin disk. The current lines form circular loops, while the model does not assume any cylindrical symmetry.

slabs and cylinders. The hysteresis loop of the thin disk on figure 5.6 agrees with equations (5.8,5.11,5.12).

Both simple situations confirm that the MEMEP 3D method can describe the Critical State Model and agrees with it. This is important validation of the model.

5.2 Finite-length superconducting thin film with constant J_c

A more advanced validation of the method is by modelling of finite size rectangular films with all finite size effects. The qualitative comparison is by current loops inside a square film. This is a common shape for investigation of characteristic parameters of superconducting films like J_c or AC loss. Therefore, the validation by square film is desirable. Further, it serves as a basic validation step for more complex modelling as it is anisotropy with perpendicular and parallel applied fields. The following modelling case is the usual electromagnetic response of a superconducting square film on perpendicular applied magnetic fields to the surface with constant J_c . The size of the sample is $12 \times 12 \times 0.001$ mm and the sketch of the square case is on figure 5.1(c). The applied magnetic field is 50 mT with frequency 50 Hz. The number of the elements in the mesh is $60 \times 60 \times 1$. The critical current density is $3 \cdot 10^{10}$ A/m² and we take a realistic n factor of 30. The model calculated 160 time steps per cycle.

The small applied magnetic field of only 19.1 mT already causes penetration of the screening current density into the square sample [figure 5.7

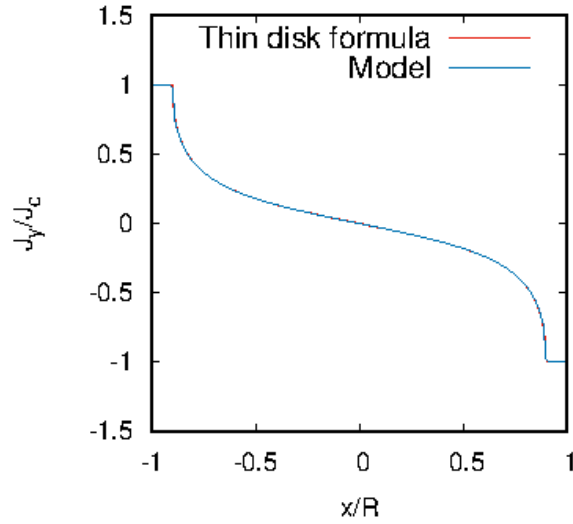


Figure 5.5: The J_y component at the mid cross-section plane $y = 0$ of a thin disk with a power-law exponent $n = 1000$ at applied field of 7.8 mT. The model agrees very well with the thin disk formula [115].

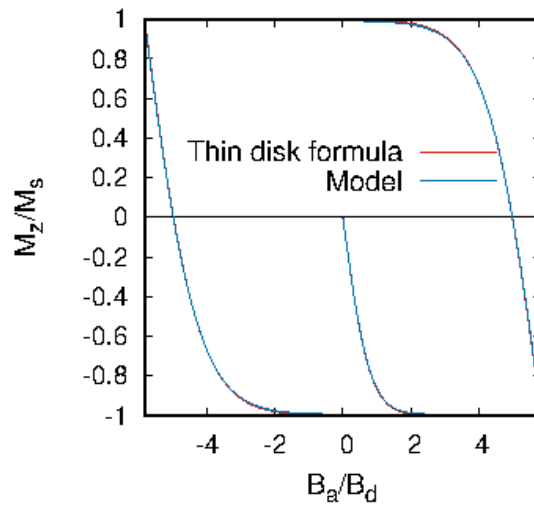


Figure 5.6: The thin disk magnetization loop agrees with the analytical formulas 5.8.

5.3. FINITE SUPERCONDUCTING THIN FILM WITH $J_C(B)$ DEPENDENCE 75

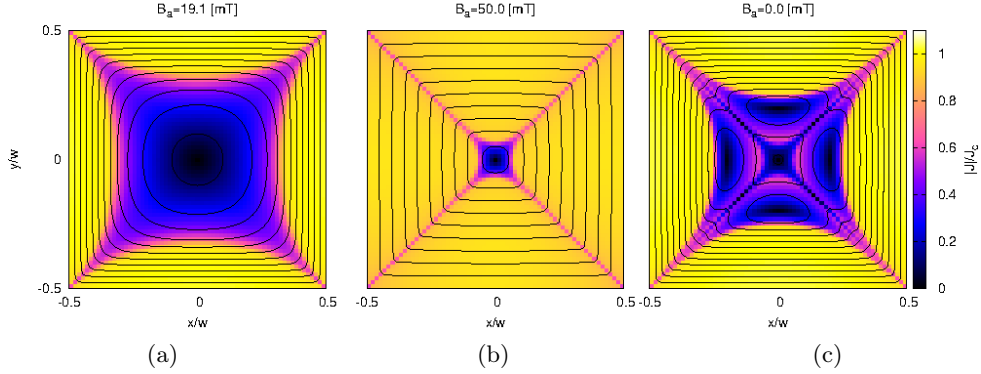


Figure 5.7: The gradual penetration of the current density into a superconducting square thin film with constant J_C dependence and perpendicular applied magnetic field to the surface with amplitude 50 mT.

(a)]. The penetration depth of the critical current density is symmetric along both x and y axes. The sample is almost fully saturated at the peak of the applied field [figure 5.7(b)]. When the applied magnetic field decreases to zero, the region with $|\mathbf{J}| = J_C$ penetrates again from the edges to the center of the sample with the opposite sign, and hence the penetration front erases the previous screening current.

The applied field must be two times higher in order to achieve a J_C penetration to the same depth. Therefore, at the remanent state with zero applied field the sample is penetrated only partially (figure 5.7(c)). The sample becomes completely penetrated at the minus peak of the applied magnetic field, $B_a = -50$ mT, achieving the same current density as figure 5.7(b) but with opposite sign.

The measurements of thin films are based on inversion. The inversion method measures the magnetic field close to the surface sample and then calculates \mathbf{J} from B_z [118–120], which qualitatively agree with our results.

The MEMEP 3D method is able to calculate the electric field, and hence also instantaneous power loss. The AC loss is on figure 5.8(a) and the hysteresis loop is on figure 5.8(b). These results qualitatively agree with previous calculations on thin films [13, 92, 116]. Therefore, these calculations further validate the results.

5.3 Finite superconducting thin film with $J_c(B)$ dependence

The next test includes $J_c(B)$ dependence in the model, since the superconductor reduces J_c by local magnetic field even by self-field, and hence

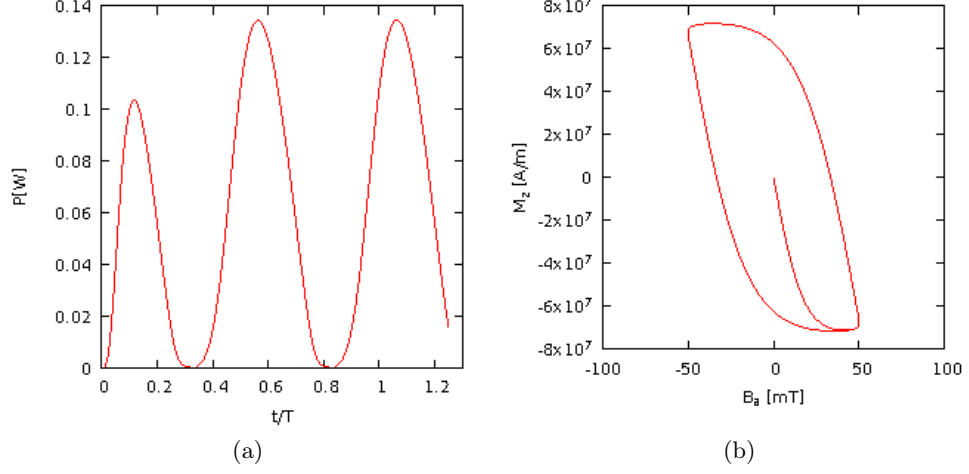


Figure 5.8: (a) AC power loss and (b) hysteresis loop of the superconducting thin film with constant J_c and power-law exponent $n=30$. The applied magnetic field amplitude is 50 mT and the frequency is 50 Hz.

the modelling tool becomes more realistic and complex. The $J_c(B)$ dependence is a further step to model force-free anisotropy inside superconductors and increases the accuracy of the AC loss calculation [121–123]. The calculations with $J_c(B)$ dependence have the same input parameters like the previous ones with constant J_c in section 5.2, except that the method assumes Kim model as $J_c(B)$ dependence [equation (2.13)] with $m=0.5$ and $B_0=20$ mT. With these parameters, we choose a value of J_{c0} so that the transport critical current I_c on an infinitely long tape is the same as that for constant $J_c = 3 \cdot 10^{10}$ A/m², resulting in $J_{c0} = 3.615 \cdot 10^{10}$ A/m².

The applied magnetic field magnetizes the square film, and hence the current density penetrates the sample [figure 5.9(a)]. The penetration depth is roughly the same as for J_c constant [figure 5.7(a)]. The current density is symmetric regarding penetration along both x and y axis and $|\mathbf{J}|$ at the critical region front is around J_{c0} . The local magnetic field decreases the critical current density, and so $|\mathbf{J}|$ does between the sample border and the moving front, where $B_z \approx 0$. The square film is almost fully saturated at the peak of the applied field with current density magnitude around $0.5J_c$ at the edges [figure5.9(b)]. When the applied magnetic field decreases back to zero, the new screening current penetrates from the edges to the center of the sample. The applied field of around 20 mT creates zones with zero local magnetic field close to the edges, where the screening current is around J_{c0} [figure5.9(c)]. The penetration front and zero local field zones move further into the center by continual decreasing the applied field to the remnant state [figure 5.9(d)] and beyond. The penetration depth is higher compared to the

Number	Dependence	$B_{a,\max}$ [mT]	AC loss[mJ]
1	J_c	50	1.22503
2	$J_c(B)$	50	1.26545
3	$J_c(B)$	100	2.70117

Table 5.1: Calculated AC loss per cycle for different cases of the thin film.

case of constant J_c (figure 5.7). Since J_c is reduced by the local magnetic field, the screening current needs bigger penetrated zone to shield the applied field.

The magnetization loop with $J_c(B)$ dependence showed lower magnetization closer to the applied field peaks compare to the constant J_c . Since the J_c is reduced by the local magnetic field. The magnetization curve is higher close to the remanent state, because of higher penetration depth [5.10(b)]. The instantaneous AC loss between $B_a = +B_{a,\max}$, being $B_{a,\max}$ the peak, and the remanent is higher for $J_c(B)$ [figure 5.10(a)]. The reason is the following. For $J_c(B)$, the magnetic field decreases the local J_c between $B_a = +B_{a,\max}$ and the remanent. This causes a larger penetration of the critical zone, increasing the instantaneous AC loss. The second calculation of the AC loss with $J_c(B)$ dependence and applied field of 100 mT shows even higher instantaneous AC loss, since the time derivative of the applied field is larger. The reduced current density at the peaks of the AC field decreases as well the magnetization [figure 5.10(b)]. The area of the magnetization loop increases [figure 5.10(b) point line], therefore the AC loss per cycle is higher. The total AC loss per cycle is in table 5.1. The cycle is from the first positive peak up to the second positive peak of the applied field. The total AC loss is similar for both J_c constant and $J_c(B)$ dependence with applied field 50 mT. The cause is that the local magnetic field is of the order of self-field. The two times higher applied field amplitude of 100 mT shows roughly two times higher AC loss [table 5.1(3)].

5.4 Coupling effects in multi-filamentary tapes

Modelling the coupling effects is important, in order to fully understand the AC loss in the multi-filamentary tapes or coupled tapes. The coupling currents causes the dominant part of the AC loss in low fields.

5.4.1 Coupling effects in two-tape conductor compared with FEM model

The last results from the thin film series is a model of coupling effects like coupling AC loss and coupling current. The modelling situation is two super-

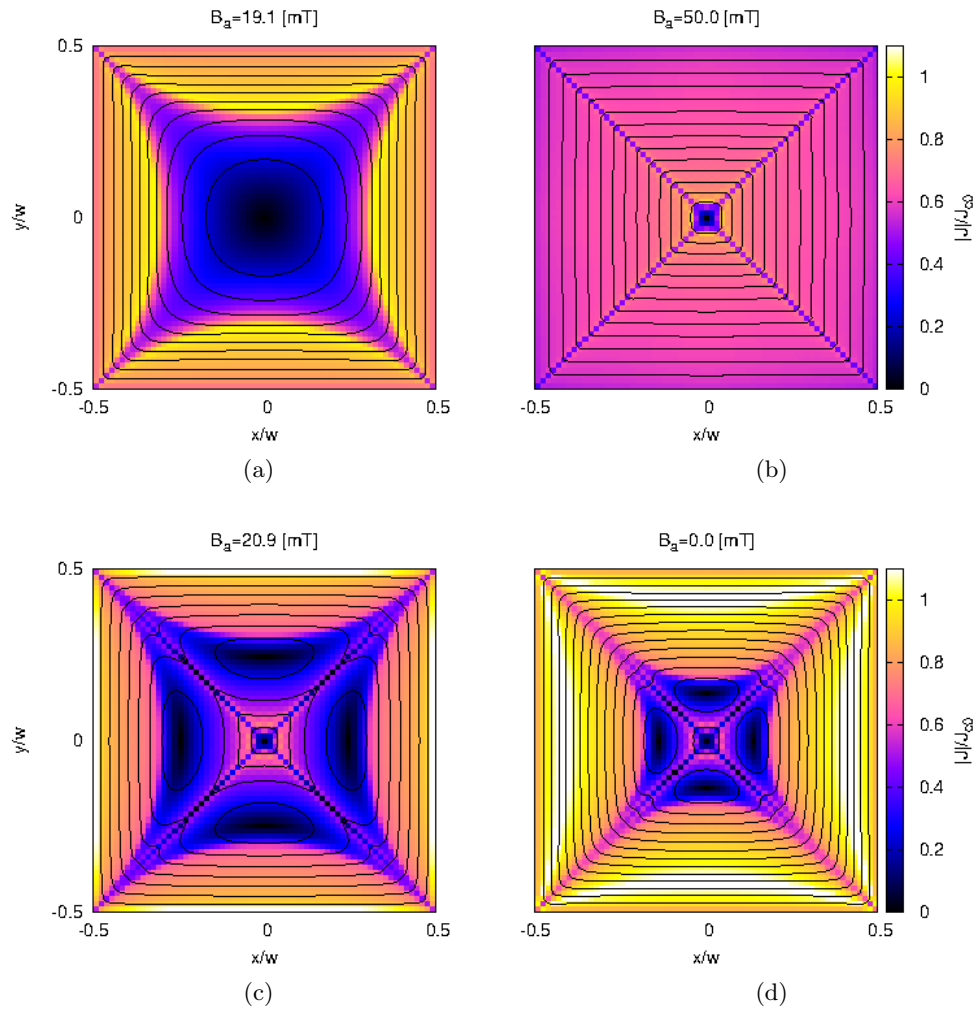


Figure 5.9: The gradual penetration of the current density into the superconducting square thin film with $J_c(B)$ dependence and perpendicular applied magnetic field to surface of 50 mT amplitude.

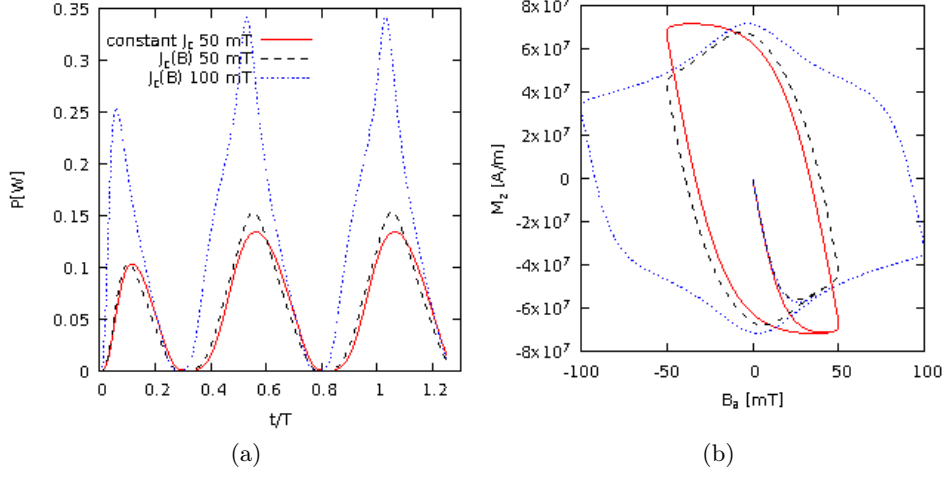


Figure 5.10: Superconducting thin film (a) AC power loss and (b) hysteresis loop of the square with $J_c(B)$ dependence (Kim model) and sinusoidal applied magnetic field ($B_a = B_{a,\max} \sin \omega t$) with amplitude of 50 mT and 50 Hz frequency.

conducting tapes coupled by a normal metal. The sinusoidal applied magnetic field is perpendicular to the surface, with an amplitude of 20 mT and frequency of the power network (50 Hz). The sample size is $4 \times 8 \times 0.001 \text{ mm}^3$ and the sketch of the geometry is on figure 5.11(a). The normal conducting material is of 20 μm width with the effective resistivity ρ_{eff} of $2.4 \cdot 10^{-11} \Omega\text{m}$. The effective resistivity is defined from measurement. The conductivity σ_m is measured along the tapes width and the resistive gap. The resistive width $w_{r,m}$ is estimated from the sample dimension. The model assumes any width of the resistive gap $w_{r,cal}$, and hence $\sigma_{cal} = w_{r,m} \sigma_m / w_{r,cal}$. From where the effective resistivity is $\rho_{eff} = 1 / \sigma_{cal}$. The critical current density is $3 \cdot 10^{10} \text{ A/m}^2$. The mesh is dedicated to 40 cells per each superconducting filament and 1 cell for a metallic joint along the x axis. The total number of elements is $(80 + 1) \times 160 \times 1$.

The usual gradual penetration of the current density at the peak of the applied field is on the figure 5.12(a). The result is compared with the same case calculated by Finite Element Method (FEM) in the \mathbf{H} formulation by Francesco Grilli 5.12(b). Both methods show the same current path and current density [124].

5.4.2 Coupling effects in two-filament tape and measurements

The similar coupling case with different sample size is calculated and later compared with the measurements (details in section 4.2). The sample size is $11 \times 22 \times 0.001 \text{ mm}$ with 150 μm width of the coupling linear material

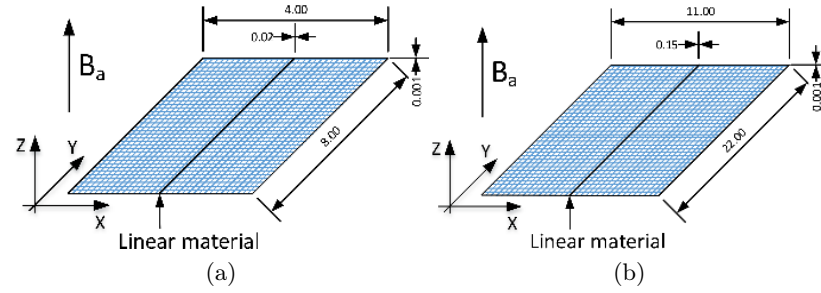


Figure 5.11: The geometry of the long strip with filaments. The superconductors are electromagnetically coupled by a linear material. Dimensions are in mm. (a)(b) Two-filament tape with different dimensions.

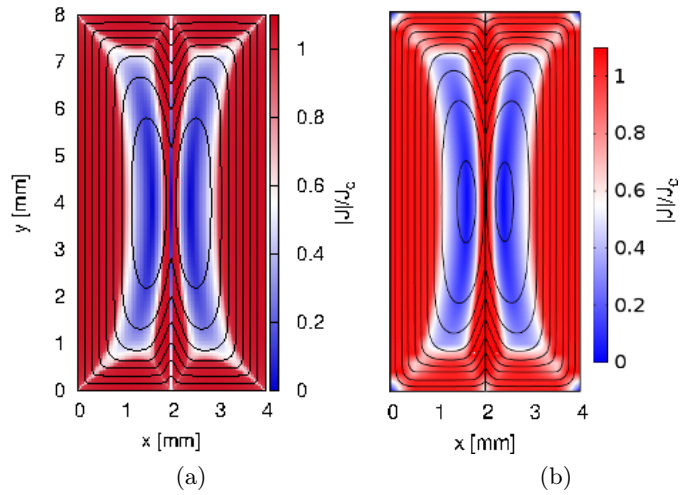


Figure 5.12: Distribution of the current density in a two-filament tape at the applied field of 20 mT with constant J_c . The results are of two methods: (a) MEMEP 3D, (b) FEM in \mathbf{H} formulation.

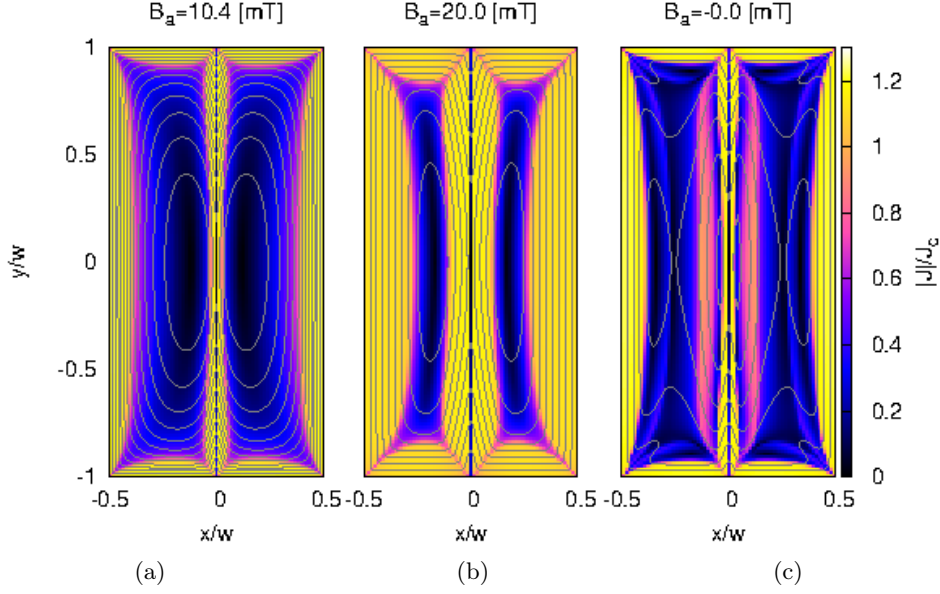


Figure 5.13: Gradual penetration of the current density into the two-filament tape with constant J_c coupled by a normal material due to perpendicular applied magnetic field to the surface (50 mT amplitude).

[figure 5.11(b)]. The critical current density of superconductor is $2.72 \cdot 10^{10}$ A/m², which is the average value of measured tape ($I_c = 160$ A of 6 mm width tape) and the effective resistivity (defined in section 5.4.1) of linear material is $39.4 \cdot 10^{-10}$ Ωm. The applied field frequency is 144 Hz and the relatively low amplitude of 20 mT ensures not fully saturated sample. The mesh contains $(70 + 1) \times 141 \times 1$ elements.

The screening current penetrates into the sample already under the small applied field of 10.4 mT [figure 5.13(a)]. The current lines are parallel to the x and y axis except the metallic joint. The metallic joint conductivity is lower than superconductor and therefore the current line loop bends around the metallic joint and passes through it further at the center of the metallic line [figure 5.13(a)]. The superconductor around the metallic joint is fully saturated with J_c . There are two paths of the current loops. The first one follows the sample outline and passes through the metallic material. The second one closes the loop in his own superconducting filament [figure 5.13(b)]. The first type of the current loop is the coupling current. The remnant state presents a complex current path of the new penetration front coming from the edges. Now, there appear current lines that cross the normal joint but they close in the superconducting region next to the joint, while at the peak of the AC field current lines crossing the joint close to the outer edges of the superconductor [figure 5.13(c)].

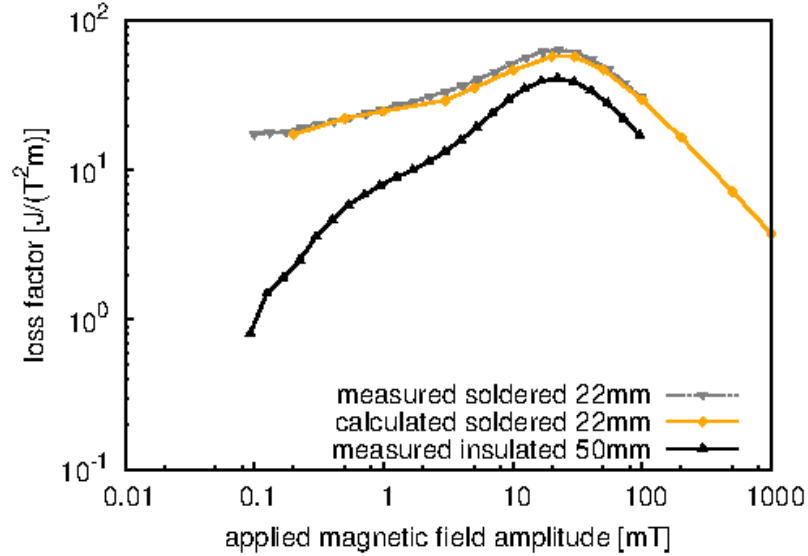


Figure 5.14: The AC loss factor, defined as the loss per cycle and length divided by the square of the applied field amplitude. Comparison of the measurements and model with two-tape conductor and frequency of the perpendicular applied field of 144 Hz. The calculations for the coupled case agree with the measurements.

The comparison of the AC loss measurement with the sample of the same parameters is on figure 5.14. The samples are measured in the applied field range from 0.1 to 100 mT amplitude (section 4.2). The calculation of the AC loss is extended to 1T. The AC loss measurements agree very well with the calculation. The total AC loss contains two contributions: the hysteresis loss from superconducting part and the coupling loss from metallic joint. The maximum 4% deviation of the AC loss is around 20 mT, being around the value of the self-field of the tape. The calculation assumes constant J_c , and hence the modelling accuracy can be even more precise by including the $J_c(B)$ dependence. The measurement of the electrically uncoupled 50 mm long tapes is in the same graph with the black curve on figure 5.14. For this case, the AC loss contains only hysteresis loss created in the superconductors. Since it is much smaller than for the coupled tapes, the coupling loss is the dominant part of the total AC loss in the soldered sample. Understanding the effects of the linear material is key for the reduction of AC loss in such structures, since the coupling current in the metal joint creates increases the loss by creating coupling loss and increasing superconductor loss. The coupling loss is a main part of the AC loss in low applied fields, while superconducting loss dominates at high applied fields.

Chapter 6

Results and discussion

Superconductors are still relatively expensive conductors. Therefore, it is an advantage to have modelling predictions of any superconducting machine before it is built and measured. Superconductors are anisotropic materials with critical current density affected by the magnetic field magnitude and its orientation. The critical current density also depends on the direction of the current density relative to the magnetic field, appearing force-free effects when \mathbf{J} has a parallel component to \mathbf{B} . Therefore, models with high accuracy and with $J_c(B)$ and anisotropy dependence are very required. 3D models with high calculation speed are needed to model properly finite superconducting samples and superconductor machines.

The AC loss in superconductors is important, since it can inflict losses the cryogenic system, causing malfunction of the machine when the heat generation is higher than the cryogenic system can pump out. Striations reduce AC loss. Therefore, AC loss prediction in multi-filament tape is important. Bulk samples are an alternative to permanent magnets, but cubic bulks are still not well understood. Therefore, a detailed study of screening current is very interesting. The magnetization of the prism with decreasing thickness shows the intermediate state between infinitely thin sheet approximation and infinite bar. The tilted applied field angle in bulks and stacks of tapes shows the fundamental difference between them. Cross-field demagnetization predicts how long the magnetization in bulks withstands under cross-fields, which is the situation in motors. The anisotropy study of thin films and prisms shows the real response of REBCO tapes as highly anisotropic material.

Therefore, the MEMEP 3D results are focused on the previously explained cases. The following sections contain original results obtained by the MEMEP 3D method. It is the most important part of thesis, apart from the method itself (section 3.1). The results study fundamental cases focusing on the screening current, magnetization, demagnetization and anisotropy in the samples. The results are important for further improvement of the superconducting power applications.

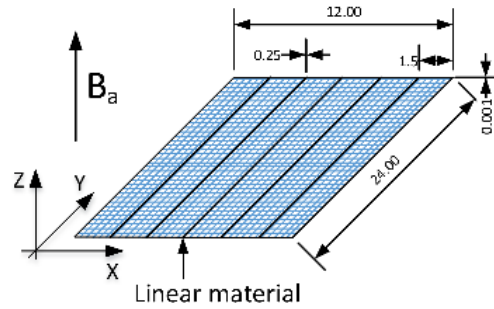


Figure 6.1: The geometry of the long strip with 6 filaments. Dimensions are in mm.

6.1 Coupling loss in multi-filament tape

The following AC loss study is based on infinitely thin film approximation (section 3.3). Other thin film and coupling situations are in section 5. Although other authors modelled electrically coupled striated tapes, the results here provide higher accuracy, and hence these calculations can be consider as an original results.

The following studied coupling situation is a tape with 6 filaments. The size of the sample is $12 \times 24 \times 0.001$ mm (figure 6.1) with the applied field of 20 mT and frequency 144 Hz. The gap between superconductors is $20 \mu\text{m}$ with resistivity $39.4 \cdot 10^{-10} \Omega\text{m}$.

The coupling current lines show the same behaviour like the case of the two filaments tape (see figure 5.13). These current lines pass through the metallic joints at instantaneous applied fields of already 10.4 mT [figure 6.2(a)]. The current density reaches the value of J_c close to the edges of the sample and around the metallic joints [figure 6.2(b)]. The remnant state shows the mixed state of the new penetration current at the edges and the previous screening current at the center of the sample [figure 6.2(c)].

A transient state appears in the model since it contains metallic parts. At remanent, there also appear closed current loops around the metal joints. The superconducting and normal magnetization currents present a phase shift from each other. Both the superconducting and normal magnetization currents present a phase shift with the applied field. This phase shift is larger than that of the two-filament tape (section 5.4.2), and hence the phase shift increases with the number of filaments. The phase shift is the most visible in the remnant state. The penetration front with the opposite sign penetrates less than half of the previous penetration depth. The method allows to model any number of filaments, as long as the mesh contains sufficiently high number of the elements for each filament. The current state of the MEMEP 3D code can accurately model up to 10 filaments.

The six-filament tape at the peak of the applied field (20 mT) shows that

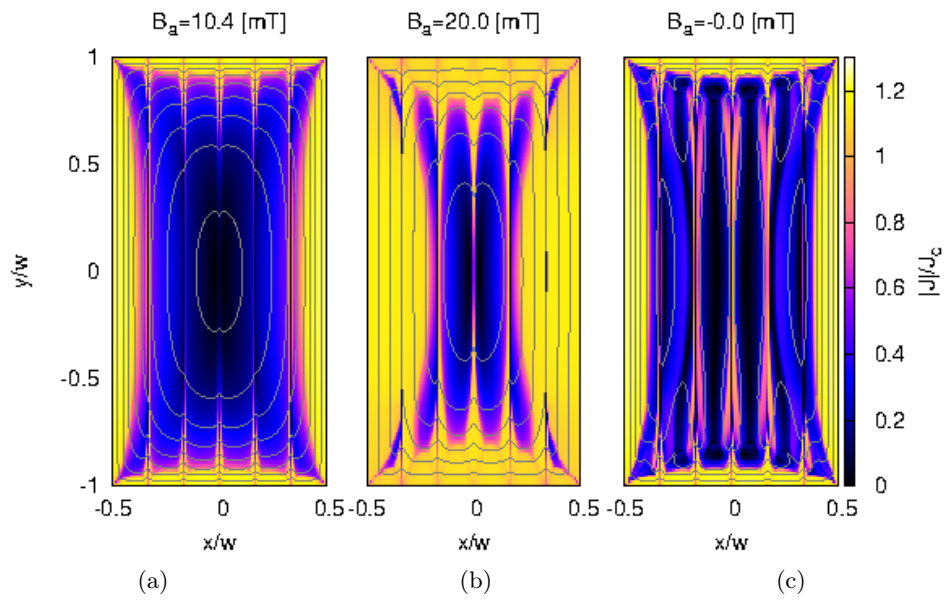


Figure 6.2: The gradual penetration of the current density into the six filament tape coupled by a linear material. Due to a perpendicular applied magnetic field to the surface with amplitude 20 mT and frequency 144 Hz. The superconductor has constant J_c .

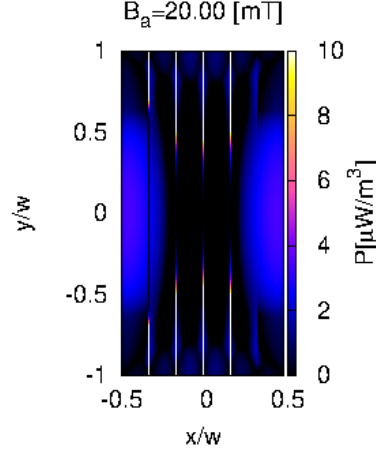


Figure 6.3: Instantaneous power loss at the peak of the applied field for the same situation as figure 6.2.

the coupling current path passes through all the metallic joints [figure 6.2(b)]. The largest AC loss density is at the linear material [figures 6.3], where the maximum loss density is 60 times higher than that in the superconductor. However, when analysing the total power loss, the superconductor is responsible of most of the dissipation, as discussed below.

The AC loss is split into coupling and hysteresis loss on figures 6.4. The applied field of 10 mT creates comparable AC losses in superconducting and normal material [figure 6.4(a)]. However, at the applied field of 20 mT the peak instantaneous AC loss in the superconductor is 6 times higher than at the normal metal [figure 6.4(b)]. Therefore, at very low field (below 10 mT in our case) the dominant part of entire AC loss is coupling loss.

The AC loss factor dependence on various applied field frequencies 1.4, 144 and 1400 Hz with the superconducting gaps of 90 μm is on figure 6.5. The model shows the highest AC loss at 144 Hz. The peaks of the AC loss factor are at the same amplitude, except small shift at 1.4 kHz frequency.

6.2 Magnetization of isotropic rectangular prisms

Before this thesis, the geometry like a cube or prism is still not completely solved and current path inside it is not well understood in spite of its simplicity, therefore a full model with all finite size effects is necessary. The isotropic bulk or prism model is a full 3D model with many layers of cells in the thickness. The MEMEP 3D method allows current to flow in all 3 dimensions (x, y, z) and hence there is \mathbf{J} with all 3 components (J_x, J_y, J_z) , as well as $\mathbf{T} = (T_x, T_y, T_z)$. The full 3D model is demanding on the calculation speed, due to the high number of variables.

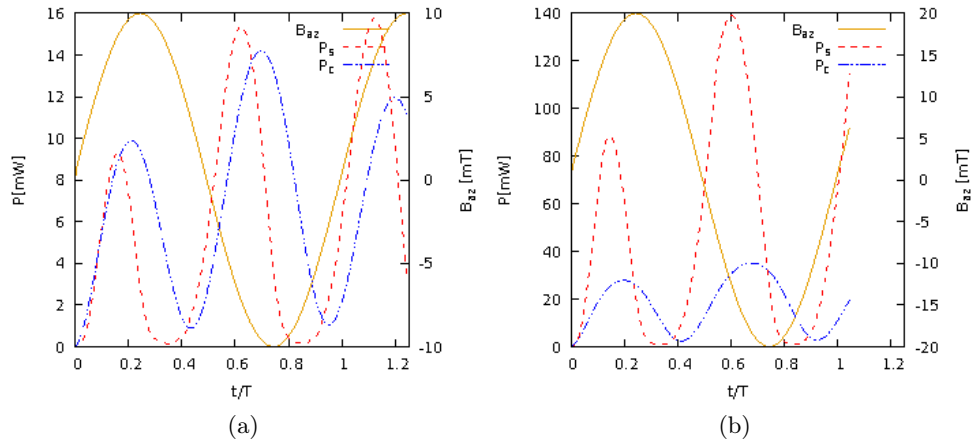


Figure 6.4: The AC loss in 6 filament tape split into superconductor loss (P_s) and coupling current loss (P_c). Cases with applied magnetic field amplitude (a) 10 mT and (b) 20 mT with frequency 144 Hz. B_{az} is the instantaneous applied magnetic field. The coupling loss increases with lower applied field.

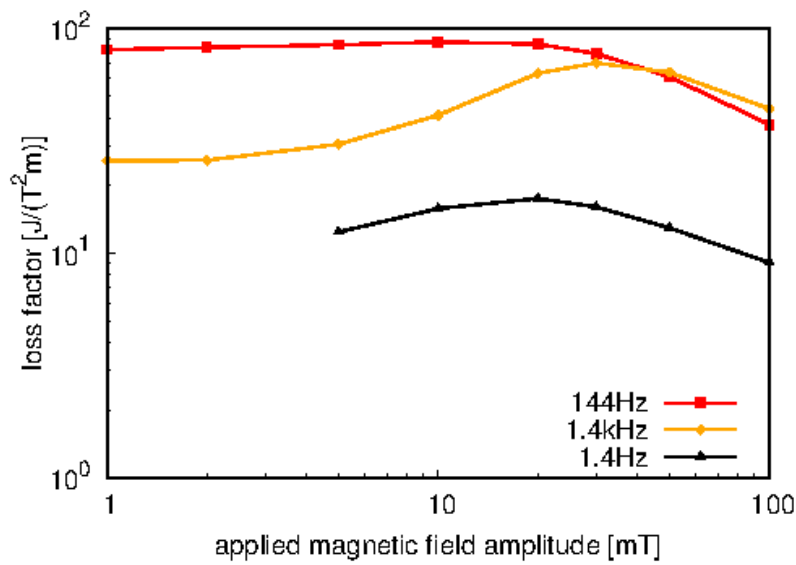


Figure 6.5: The AC loss factor is defined per cycle, divided by square of applied field and length of the sample. Calculation of the six filament tape model. Dominant part of the AC loss at low fields is coupling loss.

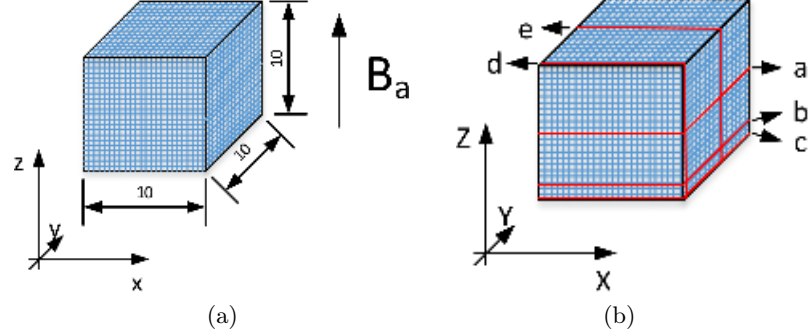


Figure 6.6: The geometry of the cube sample. Dimensions are in mm. (a) Cube and direction of the applied field. (b) The positions of the cross-sectional planes in the cube are “a”, $z/d=0$; “b”, $z/d=-0.39$; “c”, $z/d=-0.49$; “d”, $y/d=-0.49$; and “e”, $y/d=0$.

6.2.1 3D Magnetization currents with constant J_c

Screening currents

The magnetization model of a superconducting cube shows the real 3D current path. We take that the cube edge is 10 mm and the applied field amplitude is 200 mT with frequency of 50 Hz is parallel to the z axis [figure 6.6(a)]. The critical current density is $1 \cdot 10^8$ A/m² with constant J_c . We assume an isotropic power law with $n = 100$. The mesh contains $41 \times 41 \times 41$ elements, which represents more than 200000 degrees of the freedom.

The cube is not fully saturated with screening currents, because the applied field is lower than the saturation field [figure 6.7]. The mid plane at $y/w = 0$ shows the J_y component on figure 6.7. The current distribution in this plane is similar to 2D cross-sectional models for infinitely long samples along the y axis [11]. Close to $z = 0$, the penetration depth of $|\mathbf{J}| \approx J_c$ into the cube is only around $x/w = 0.2$ and the penetration front is almost flat at the center. The screening current penetrates only in a thin area from the top and bottom. The J_x component at plane $x/w = 0$ is symmetric to J_y because of the cube symmetry.

The colour maps in three different heights of the cross-sectional planes show the same penetration depth of the current modulus from all sides [figure 6.6(b)]. At the mid plane ($z/d = 0$), the screening current penetrates $x/d \approx 0.2$ from each edge of the cube and the current lines are square, following the outer shape of the cube [figure 6.8(a)]. The penetration depth is higher at a lower plane $z/d = -0.39$ and the current lines closer to the center starts to be rounded [figure 6.8(b)]. The last plane, $z/d = -0.49$, shows full penetration and fully rounded current lines at the center of the plane [figure 6.8(c)].

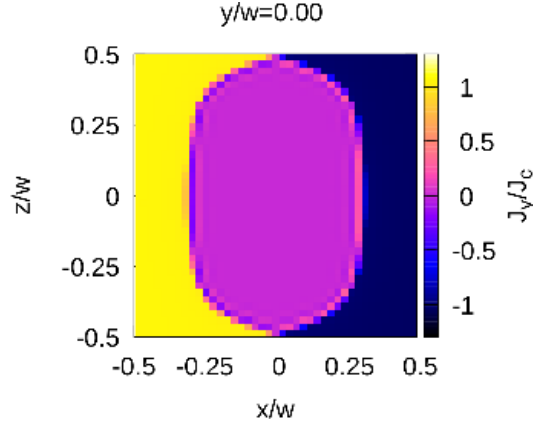


Figure 6.7: The J_y component at the mid cross-section plane $y/d = 0$ of the cube in figure 6.6 at the applied field amplitude of 200 mT. The power law exponent is $n=100$.

The MEMEP 3D model also finds the J_z component of the current density inside the cube. The maximum magnitude of J_z is around $0.3J_c$, being the highest around the diagonal lines in the plane $z/d = -0.39$ [figure 6.8(e)]. This is the reason why we chose the $z/d = -0.39$ plane for the maps. The lateral surface $y/d = -0.49$ shows symmetrical distribution of J_z [figure 6.8(d)]. J_z slightly bends the main screening current in the z direction. The full 3D current path is on figure 6.10. The current path goes up and down in the places where J_z has the highest value. J_z at the mid plane $z/d = 0$ is zero, because of cube symmetry. The main reason of the existence of J_z is a shape of the sample. The cylinder does not have J_z component, because the circular screening current loops shield the magnetic field completely. However, the square current loops cannot create uniform self-field in the corners of the sample in order to completely shield the magnetic field. The self-field in the corners is higher than along the rest of the current path, and hence the J_z currents are necessary to completely shield penetrating field at the region with $|\mathbf{J}| < J_c$. The J_z current exists only in the case of not fully saturated sample [125]. Previous works from Badia [113, 125] justified that the current loops always need to be rectangular, also below full penetration. However, the argumentation assumes that $|\mathbf{J}|$ can only be 0 or J_c , while the Critical-State Model allows any $|\mathbf{J}| < J_c$.

The same model study is on the cube with the similar input parameters except the power law exponent $n=30$. The calculation shown the J_z (figure 6.9) is qualitatively the same as case with $n = 100$. The result confirmed that the J_z is independent on the power law exponent.

The second magnetization calculation is with applied field 1 T. The applied field is higher than the saturation field, which is $B_s = 413$ mT. The current density $|\mathbf{J}|$ is practically equal to J_c because of the high power law

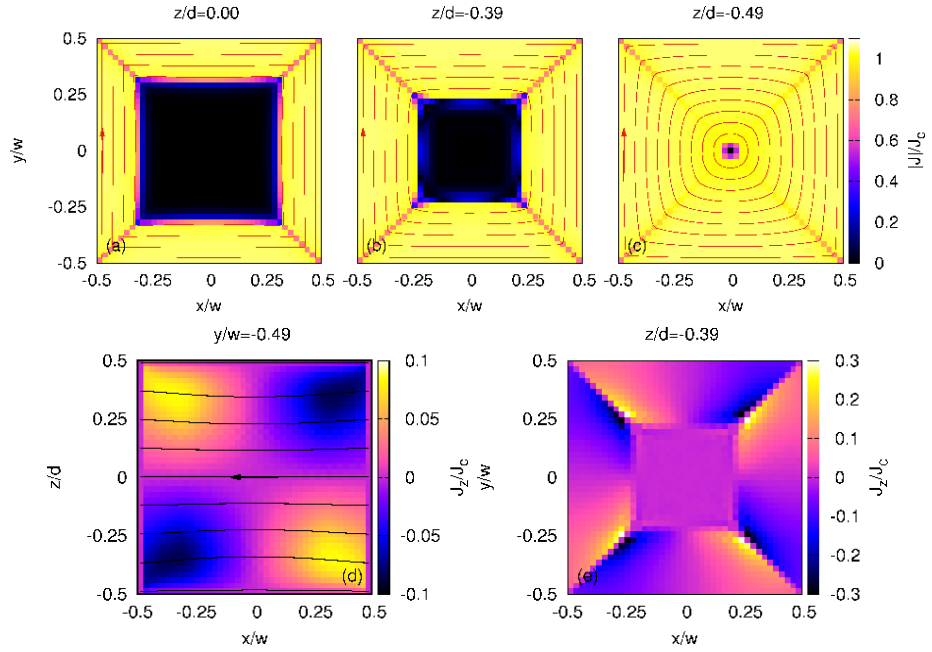


Figure 6.8: The penetration of the current density modulus into the cube with power law $n = 100$ at the peak of the applied field of 200 mT amplitude. The cross-sectional planes are at (a) $z/d = 0$, (b) $z/d = -0.39$, (c) $z/d = -0.49$, (d) $y/w = -0.49$ and (e) $z/d = -0.39$.

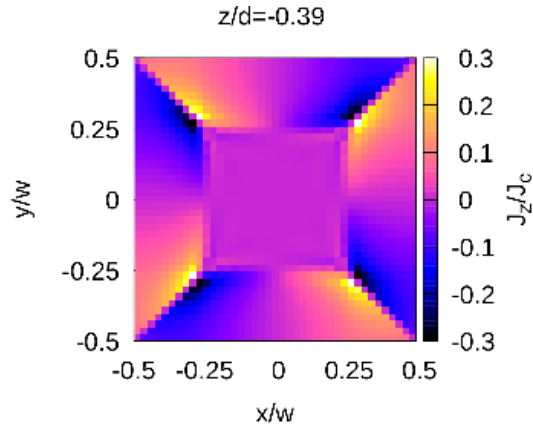


Figure 6.9: The J_z component at the mid cross-section plane $z/d = -0.39$ at the applied field amplitude of 200 mT. The power law exponent $n=30$ proved independence of the J_z on the CSM.

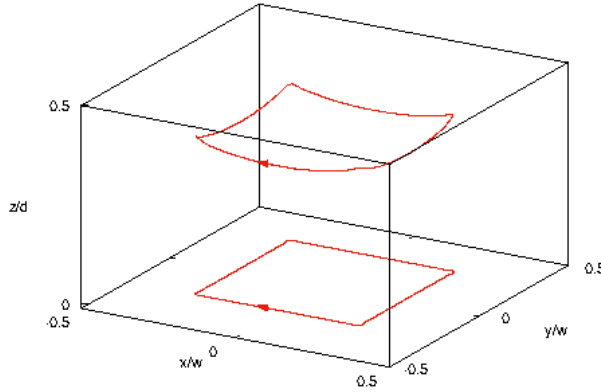


Figure 6.10: The upper half of the cube sample with real 3D current lines in two positions. The current lines are bended from z plane by J_z component, which improve shielding of the applied fields in corners.

$n=100$. The current line loops are all square [figure 6.11(a),(b),(c)]. Since the sample is fully saturated $|\mathbf{J}| = J_c$ everywhere, and hence current loops need to be square due to current conservation [125]. The model shows zero value of J_z at the planes $y/d = -0.49$ and $z/d = -0.39$ on figures 6.11(d)(e), and hence the model confirms the Critical State prediction for long bars.

Effect of aspect ratio of rectangular prisms

A prism with any intermediate thickness is more realistic than any slab, cylinder or thin sheet approximation, and hence the model includes all finite size effects. This model is more accurate and reveals new effects.

The next modelling situation is the magnetization of prisms with different aspect ratio $c = d/w$, where d is the thickness of the sample and w is its width. The cross-section of the prisms is 12×12 mm and their thicknesses are $d = 20, 10, 5, 2, 1$ mm (figure 6.12). The critical current density is $J_c = 1 \cdot 10^8$ A/m² for all aspect ratios $c = 2, 1, 0.5, 0.2, 0.1$ and the n factor is 100. The applied magnetic field is parallel to the z axis with frequency 50 Hz.

The mesh of various c cases are created by different number of cells such as $c = 0.1$ ($101 \times 101 \times 11$), $c = 0.2$ ($81 \times 81 \times 21$), $c = 0.5$ ($61 \times 61 \times 31$) and $c = 1$ ($41 \times 41 \times 41$). Therefore, the colour maps are finer in the z plane for thinner samples. The applied magnetic field for $c = 1$ is 200 mT, which is 0.484 of the penetration field, B_p . We assume the same ratio for the applied field, $B_a = 0.484B_p$, and hence the applied field for the prism with various aspect ratios are $B_a = 200, 153.02, 87.65, 51.81$ mT. We calculate and discuss the penetration field in section 6.2.3.

The J_y component at the mid-cross section plane $y/w = 0$ for each case of c is on figure 6.13. Close to the center, the J_c penetration front for $c = 1$ is around $x/w = 0.2$ from both sides of the prism and is almost flat along the

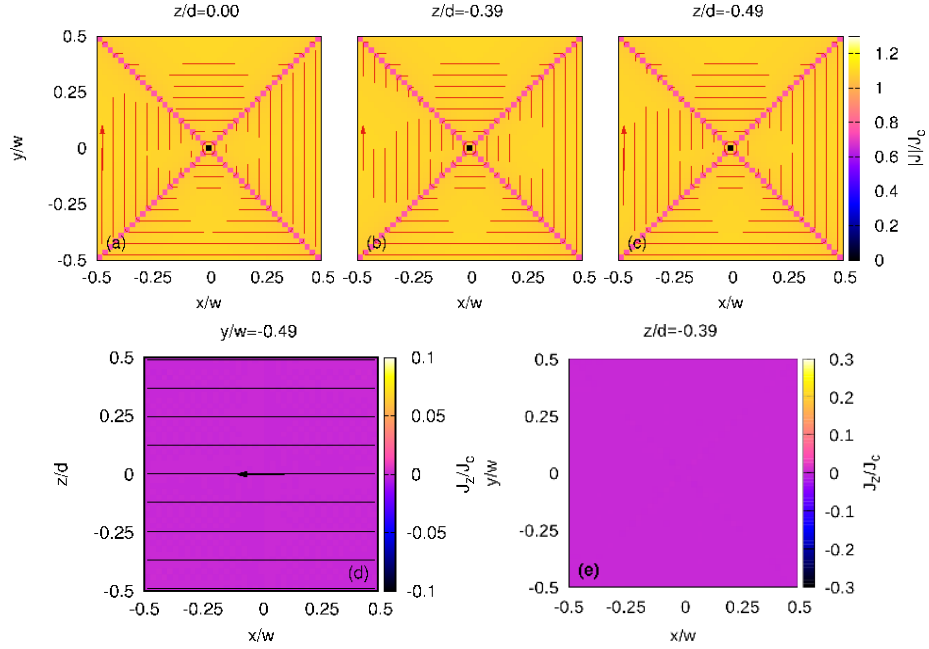


Figure 6.11: The penetration of the current density modulus into the cube with power law $n = 100$ at the instantaneous applied field of 418 mT. The cross-sectional planes are at (a) $z/d = 0$, (b) $z/d = -0.39$, (c) $z/d = -0.49$, (d) $y/w = -0.49$ and (e) $z/d = -0.39$.

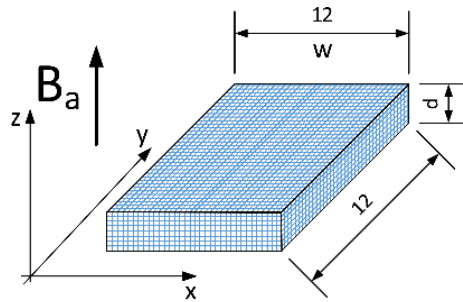


Figure 6.12: The geometry and dimensions of the prism (in mm) with the direction of the applied field, where d is the thickness of the prism and w is its width. The aspect ratio is defined as $c \equiv d/w$.

z axes. There is an additional close to the center small penetration from top and bottom [figure 6.13(a)]. The thinner prism with $c = 0.5$ shows shorter flat part of the J_y [figure 6.13(b)]. There is no flat part of J_y along the z axis in the case of $c = 0.2$ and the not penetrated zone is roughly elliptic [figure 6.13(c)]. The thinner prism with aspect ratio 0.1 presents again the same penetration depth and not saturated central zone, which is basically a thinner ellipse [figure 6.13(d)]. The J_y distribution shows that even in the thinnest prism, the current penetration depth is similar to the bulk one [figure 6.13(a)].

The next colour maps contain the J_z distribution in different planes z/d (figure 6.14). These are the planes that show the highest value of J_z for each c . The cubic bulk shows the highest J_z along the diagonal lines in plane $z/d = -0.39$ [figure 6.14(a)]. The prism with $c = 0.5$ has the same J_z distribution in relatively lower plane $z/d = -0.32$ [figure 6.14(b)]. The penetration depth in a thinner prism with $c = 0.2$ is slightly smaller and J_z has smooth and round penetration front [figure 6.14(c)] instead of the flat parts along the x and y axis like in the cube [figure 6.14(a)]. The round penetration front comes from non-square current loops in the z plane projection, which are explained in the next section 6.2.1. The last prism, with $c = 0.1$, still has J_z around $0.3J_c$ along the diagonal lines but in plane $z/d = -0.27$ [figure 6.14(d)]. The z/d plane with the highest J_z is moving to the center of the prism exactly according to the additional J_y penetration in figure 6.13 from the bottom and the top of the prism. The plane of maximum J_z corresponds roughly to the center of this zone with additional penetration. The cause is that J_z is caused by the self-field, being the highest close to the sample ends. Moreover, J_z approaches zero at exactly the sample end. The model shows that the J_z component is not vanishing with decreasing the aspect ratio and that the penetration front starts to be rounded.

Thin rectangular prism (aspect ratio $c = 0.1$)

This section is focused on the 3D current path in the thinnest prism, with aspect ratio $c = 0.1$. The modulus of the current density is on figure 6.15. The figure also shows the current lines, which are a projection on the plotted plane of the 3D current lines. The mid cross-section plane $z/d = 0$ shows the penetration depth of the screening current [figure 6.15(a)]. The lower plane $z/d = -0.09$ presents almost square current lines and higher penetration depth [figure 6.15 (b)]. The plane $z/d = -0.18$ shows smooth bending of the current lines at position 2 on figure 6.15(c) and a flat path section marked as 1. The current path in position 1 is in the same z plane but in position 2 the current path is going out of the shown z plane and back, because of the J_z component [figure 6.16(c)]. The planes $z/d = -0.27$ and $z/d = -0.36$ start to make rounded current lines close to the diagonals [figure 6.15(d)(e)] with higher penetration of the current density. The last plane $z/d = -0.45$ is

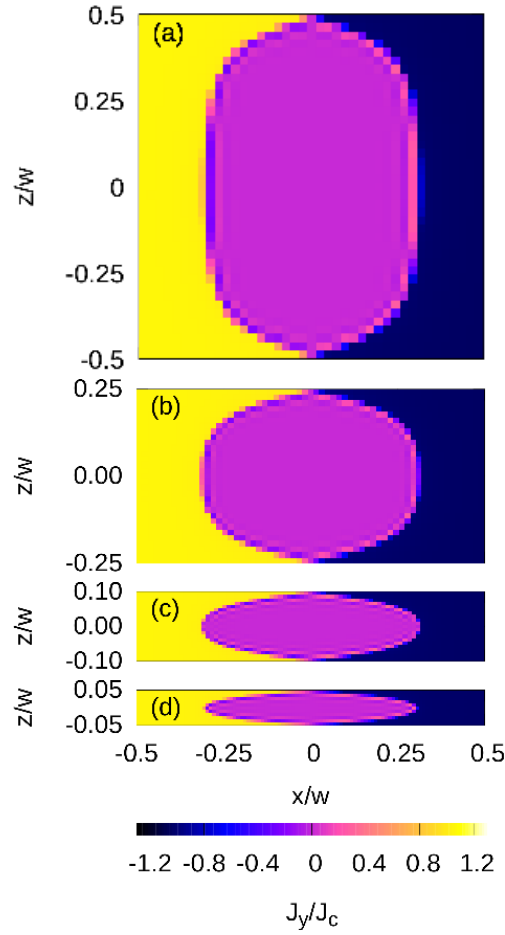


Figure 6.13: The J_y component of the current density in the mid plane $y/w = 0$ for various aspect ratios $c = w/d$ of the prism with $n=100$ and the applied field of the same ratio $B_a = 0.484B_s$, where B_s is the saturation field defined in section 6.2.3. (a) $c=1$, (b) $c=0.5$, (c) $c=0.2$, (d) $c=0.1$. The penetration depth of J_y is the same for each case of c .

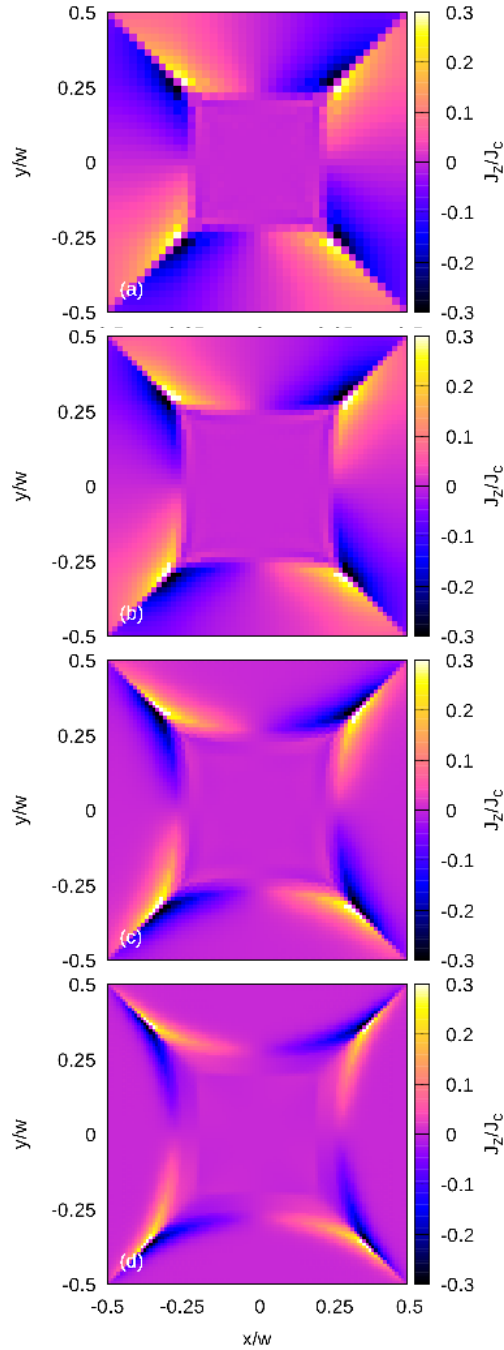


Figure 6.14: The J_z component of the current density in the prism with various aspect ratios c in the z plane with the highest value. (a) $c=1$, $z/d=-0.39$ (b) $c=0.5$, $z/d=-0.32$ (c) $c=0.2$, $z/d=-0.29$ (d) $c=0.1$, $z/d=-0.27$.

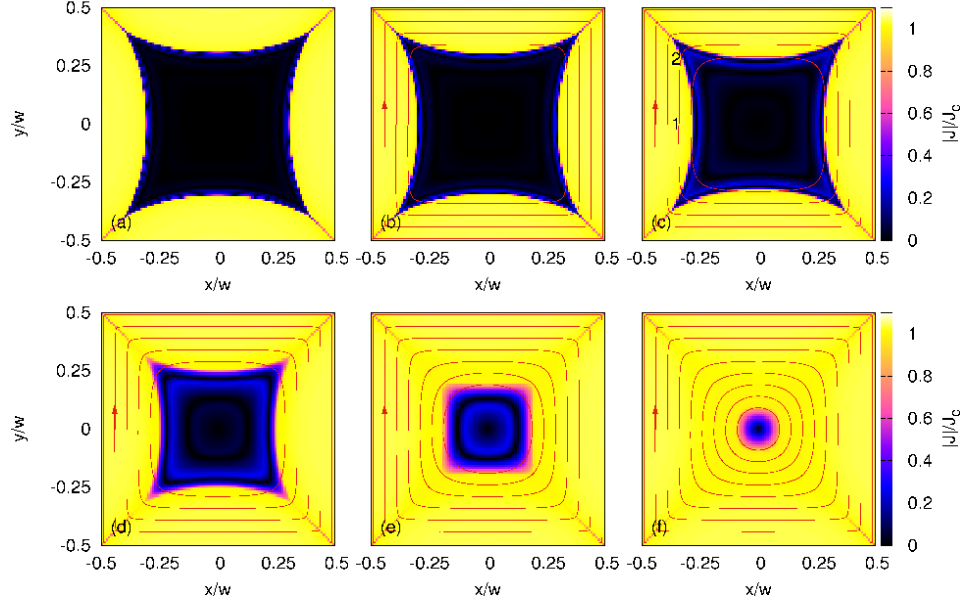


Figure 6.15: The gradual penetration of the current modulus into the prism with aspect ratio $c=0.1$ and $n=100$ at the peak of the applied field 51.81 mT. The different positions of the z plane are (a) $z/d=0.0$, (b) $z/d=-0.09$, (c) $z/d=-0.18$, (d) $z/d=-0.27$, (e) $z/d=-0.36$, (f) $z/d=-0.45$.

close to the bottom surface, where the sample is almost fully penetrated. The current lines are circular at the middle of the plane and square close to the edges [figure 6.15(f)]. The maps reveal that in the thinnest prism, $c = 0.1$, there exist circular current lines closer to the top and bottom surfaces, as it was shown in the bulk sample section (6.2.1).

The J_z component of the current density is zero in plane $z/d = 0$ [figure 6.16(a)], because of the cube symmetry. Since the current can not flow outside the sample, J_z is almost zero close to the bottom surface [figure 6.16(f)]. The J_z penetration front is a bit beyond the modulus penetration front with $J \approx J_c$ [figure 6.16(b)]. The penetration front contains the J_z current density with higher value at the diagonals, such as position 2, and lower value at the straight parts, such as position 1 on figure 6.16(c). The current path from the shown z plane is bended down to a lower plane at the position 2 and then back. The complete 3D current lines are on figure 6.17. The current lines are clearly bended at the diagonals. The highest bending is in the prism with aspect ratio $c = 0.1$, being and smaller in the prism with $c = 1$ (figure 6.10). J_z in the lower plane $z/d = -0.27$ is moving further into the prism with the highest value $0.3J_c$ [figure 6.16(d)]. The next plane decreases J_z [figure 6.16(e)] since the z planes are saturated with J_x and J_y components close to J_c . The prisms show that non-zero J_z exists as well in

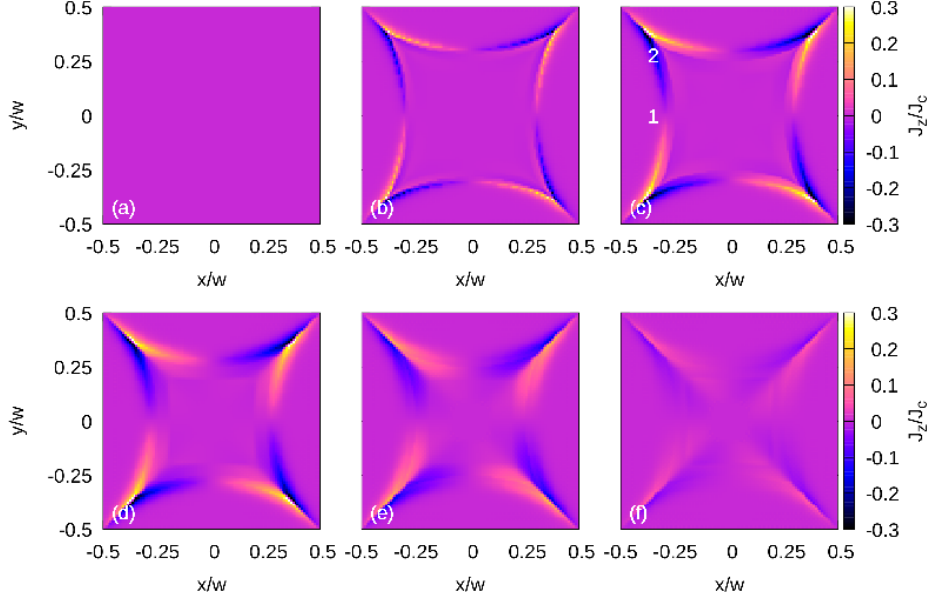


Figure 6.16: J_z in the prism with aspect ratio $c=0.1$ and $n=100$ at the peak of the applied field of 51.81 mT. The different positions of the z plane are (a) $z/d=0.0$, (b) $z/d=-0.09$, (c) $z/d=-0.18$, (d) $z/d=-0.27$, (e) $z/d=-0.36$, (f) $z/d=-0.45$.

the thinnest prism with aspect ratio $c = 0.1$ and that its maximum value.

The thickness-average current density of the prism with aspect ratio $c = 0.1$ is on figure 6.18. The current lines are calculated from the average \mathbf{T} , having only z component. The penetration of critical current density and the shape of the current lines are similar to the thin film case [figure 5.7(a)] [126]. It confirms that there must exist current lines with square and circular current paths in the cube or prism. Indeed, rounded current lines of the thickness average of \mathbf{J} cannot be obtained by superposing rectangular current lines at every height z .

6.2.2 3D Magnetization currents with $J_c(B)$ dependence

The next calculated electromagnetic response is for a cube model that includes $J_c(B)$ dependence, using the same input parameters as for constant J_c in section 6.2.1. The critical current density is $J_{c0} = 1 \cdot 10^8$ A/m², being the same value as for the constant J_c case, and $B_0 = 20$ mT. The $J_c(B)$ dependence is Kim model of (2.13) with the following parameters $m=0.5$ and power law $n=30$.

The distribution of J_y in the mid plane $y/w = 0$ at the applied field 178.2 mT is on figure 6.19. The current distribution is similar to the J_y of the constant J_c (figure 6.7). The penetration front of J_y reaches the J_{c0} value

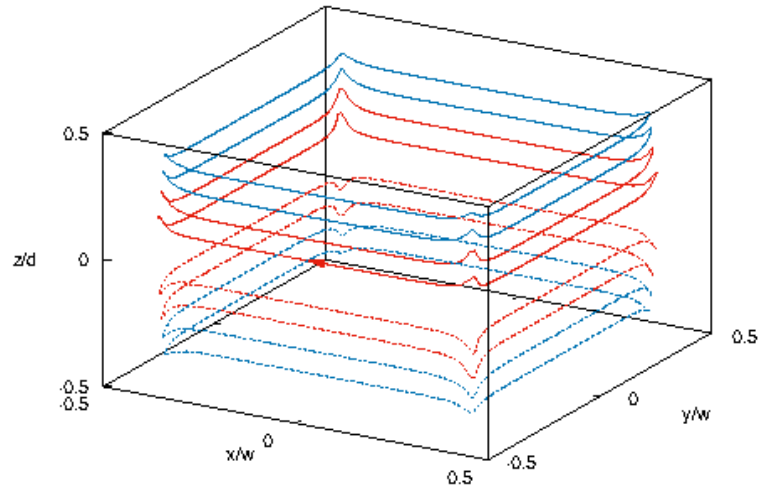


Figure 6.17: The 3D current lines in the prism with aspect ratio $c=0.1$. The current path goes up and down in the places with the highest J_z with the same behaviour like in bulk sample (figure 6.10).

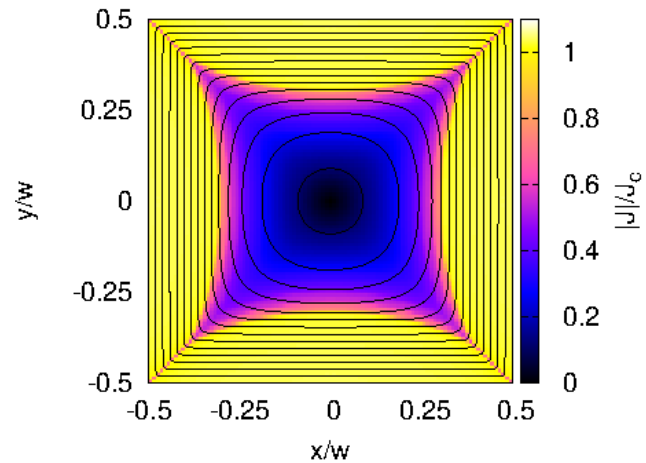


Figure 6.18: The average current density over the thickness of the prism with aspect ratio $c = 0.1$. The current distribution is qualitatively similar to the thin film (figure 5.7).

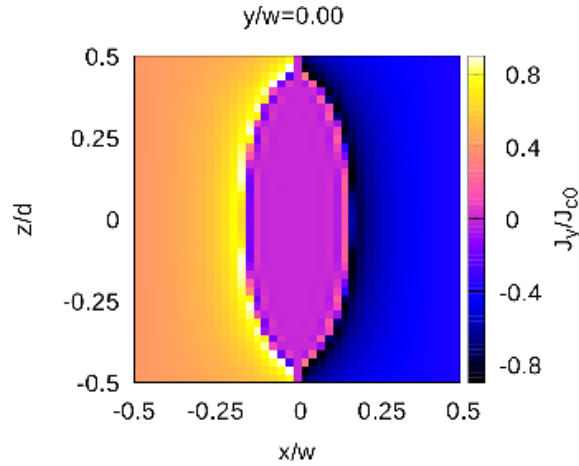


Figure 6.19: The J_y component at the mid cross-section plane $y = 0$ at the applied magnetic field 178.2 mT with $J_c(B)$ dependence. The power law exponent is $n=30$. The penetration depth is higher compare to J_c constant case (figure 6.7).

and the current density slowly decreases when moving towards to the edges of the sample. The J_y component decreases because the local magnetic field reduces J_c , and hence so does J_y . Since local $J_c(B)$ is lower than J_{c0} , the penetration depth is higher compared to the case of J_c constant with value J_{c0} , in order to completely shield the applied magnetic field at the center.

The current density modulus in all planes shows the same penetration depth as J_y [figure 6.20(a,b,c)]. The current loops are square at the mid plane $z/d = 0$ and $z/d = -0.39$ [figure 6.20(a)(b)]. The current lines are a bit rounded close to the center in the plane $z/d = -0.49$ [figure 6.20(c)]. The penetration front of the modulus shows a value around J_{c0} with reduction when approaching to the edges like the J_y component in figure 6.19. The magnetic field dependence increases the penetration depth. The current loops close to the top and bottom are not fully rounded, because the sample is closer to the saturation state [figure 6.20(c)]. The current lines are square in the square sample at the saturated state. The J_z component decreases close to the edges, because of the local saturation state [figure 6.20(e)]. J_z is almost zero at the lateral surface $y/d = -0.49$ [figure 6.20(d)]. The local magnetic field and the higher sample penetration decreases the maximum J_z to the value of $0.2J_{c0}$.

6.2.3 Magnetization loops and penetration field of rectangular prisms with constant J_c

The magnetization loops for the prisms with all aspect ratios c and the applied magnetic field 1 T is on figure 6.21. The saturation field increases

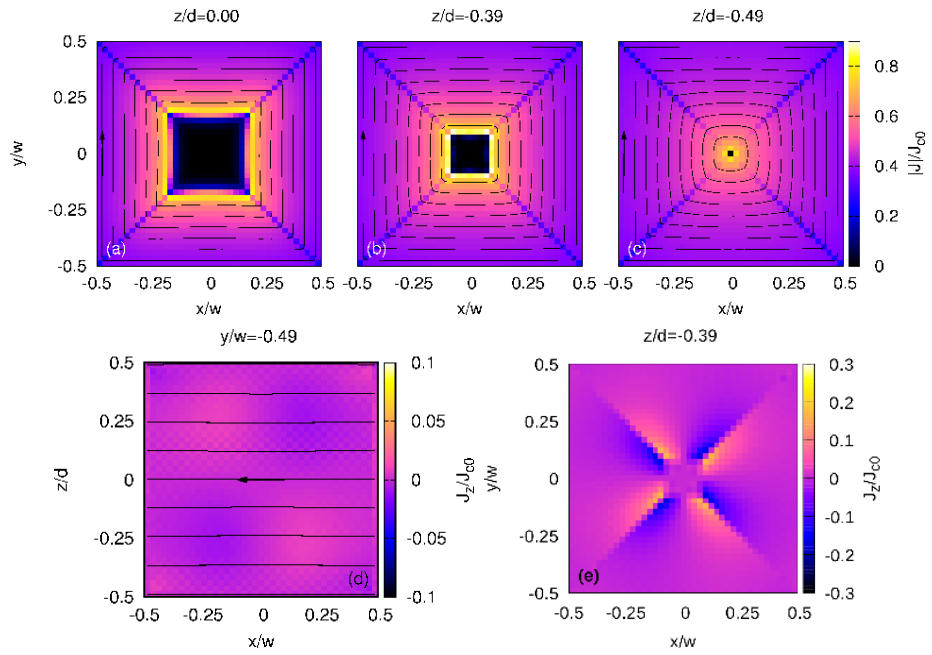


Figure 6.20: The penetration of the current density modulus and J_z into the cube at the instantaneous applied field 178.2 mT with power law $n=30$ with $J_c(B)$ dependence. The cross-sectional planes are at (a) $z/d=0$, (b) $z/d=-0.39$, (c) $z/d=-0.49$, (d) $y/w=-0.49$ and (e) $z/d=-0.39$.

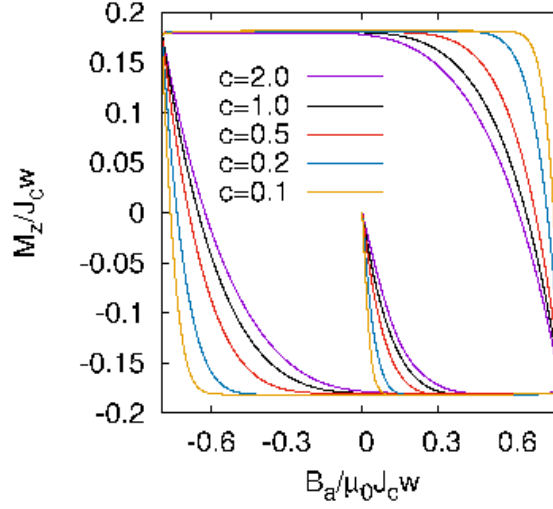


Figure 6.21: The hysteresis loops of the prisms with various aspect ratio $c = d/w$ and the applied field amplitude of 1 T. The saturation field increases with aspect ratio c .

with the thickness of the prism. Higher prisms can induce screening currents in a larger zone, and hence they shield higher applied fields at the sample center.

We set the criterion that the saturation field (or penetration field) is 99% of the magnetization of the sample, $M(B_p) = 0.99M_s$. We choose that criterion, in order to unified the criterion for others shapes like cylinder ($M = 0.9903M_s$), slab ($M = 0.75M_s$) and strip ($M = 0.9856M_s$). Since the rectangular prisms contain similar behaviour from all of them. The penetration field dependence on the aspect ratio is on figure 6.22 and values are in the table 6.1. The analytical fit of equation (6.1) reaches 97% accuracy and it also includes the limits for infinite bar and thin square film. The analytical fit is

$$B_s(c) = \mu_0 J_c w a_1 \left[1 + a_2 e^{\frac{-\ln^2(a_3 c)}{2a_4^2}} \right] \tanh(a_5 c), \quad (6.1)$$

where the fit parameters are $a_1 = 0.3915$, $a_2 = -0.26$, $a_3 = 2.56$, $a_4 = 0.75$ and $a_5 = 2.41$.

6.2.4 Benchmark of superconducting bulk with perpendicular applied magnetic field.

The state of the art of the modelling methods and tools is presented biannually at the International Workshop on Numerical Modelling of HTS [127].

Aspect ratio	d/w	Saturation field $B_s/J_c w \mu_0$
2.0		0.38
1.0		0.32
0.5		0.25
0.2		0.14
0.1		0.08

Table 6.1: Calculated saturation field for the prisms with various aspect ratio c . The saturation field is assumed as the one that causes 99% of the magnetization $M(B_s) = 0.99M_s$.

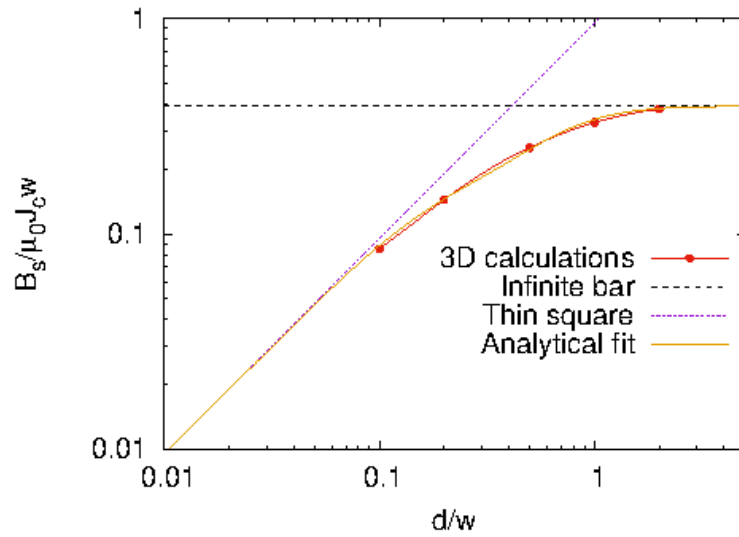


Figure 6.22: The saturation field increases with on the aspect ratio $c = d/w$. The analytical fit of equation (6.1) reaches 97% accuracy and meets the thin square and infinite bar limits.

The HTS Work Group maintains the benchmark web site [128], in order to evaluate many kinds of modelling tools. In conclusion, the workshop in 2016 showed that the 2D models reached the required level of development to model most power application.

The MEMEP 3D results for the cube magnetization have been chose as a simple benchmark test to develop 3D modelling tools. The simple modelling case serves as an example to test the speed and accuracy of new 3D modelling methods.

The modelling situation is a superconducting cube with the same parameters as in section 6.2.1, where all finite size effects are explained.

The modelling mesh contains $41 \times 41 \times 41$ cells, which is 211806 degrees of freedom. The current tolerance is $10^{-5} J_c$. The calculation time is less than 7 hours on desktop computer: Intel Core i7-4771 CPU@3.50GHz8, 8GB RAM, Linux Ubuntu 64 bit.

6.3 Magnetization of stacks of tapes and bulks in tilted applied field

2D cross-sectional model cannot model finite size effects, which are important; and hence state-of-the art modelling tools starts to model full 3D cases [129, 130]. However, 3D modelling needs to be improved, since the accuracy of models is low [32, 131–133] due to the required high number of elements.

The 3D modelling cases of the stack of tapes and homogeneous bulk with tilted applied magnetic field are interesting, since they can be seen in experiments by VSM and SQUID and for power applications such as motors and generators [134]. The 2D results have been already predicted by [135, 136]. However, the full 3D models with all finite size effects are missing. The magnetic response of stacks of tapes and bulks is expected to be different.

6.3.1 Screening currents

The magnetization of stack and bulk by tilted applied field is modelled by MEMEP 3D, in order evaluate the method and see all finite size effects in full 3D models and compare to other methods.

The modelling geometry is on figure 6.23(a). The sample size is $10 \times 10 \times 1$ mm, where w is width and d is thickness of the sample. The sinusoidal applied magnetic field is of 200 mT amplitude and 50 Hz frequency with angle $\theta = 60^\circ$. The critical current density is $1 \cdot 10^8$ A/m². We assume isotropic power law with $n=25$. We model both bulk and stack geometries. For the stack, we take the homogeneous approximation. The difference between them is that the bulk allows currents to flow in any 3D direction in contrast

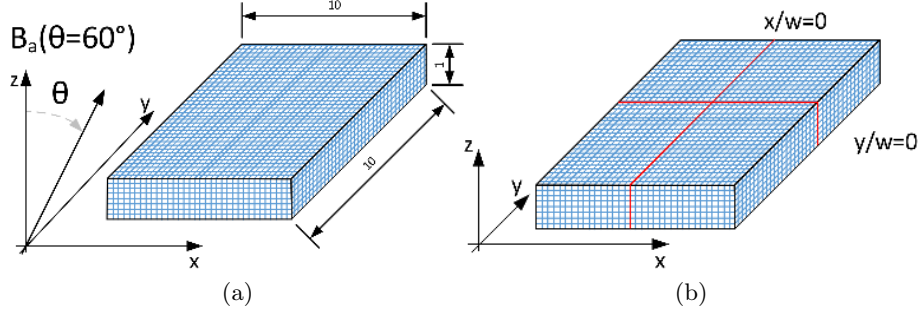


Figure 6.23: The geometry of the bulk and stack samples. (a) The size of the sample with the angle of the applied field. Dimensions are in mm. (b) The cross-sectional planes for the colour maps with w as width of the sample.

to the stack, where there is no current in the direction perpendicular to the tapes surface. The stack model assumes electrically isolated tapes, and hence J_z always vanishes.

In the midplane with $y/w = 0$ (y -midplane), the current density distribution in the bulk sample is fully saturated with J_y [figure 6.24(b)]. The border between positive and negative current density is tilted according to the applied field angle θ . The border plane is not parallel to θ because of the effect of the self-field. For much larger applied fields, we expect a border that is parallel to the applied field. In the midplane with $x/w = 0$ (x -midplane), J_x penetrates completely into the sample only in the mid- z line [figure 6.24(a)]. In contrast, the stack response to the applied magnetic field is different. The J_x and J_y components at the x - and y -midplanes, respectively are symmetric, since J_z is zero. The center zone is not fully saturated with any component of the current density [figure 6.24(c) for J_x and (d) for J_y], because the top and bottom “tapes” partially shield the applied field. At the top and bottom planes, the prism is fully saturated. The screening current in the center, $z/d = 0$, needs to shield smaller magnetic fields, and hence the current density penetrates less.

6.3.2 AC loss, magnetization loops, and comparison with other methods

Different 3D modelling methods can reproduce the electromagnetic response of our studied cases, which will further validate the MEMEP 3D method. In this sub-section, we focus on the comparison of three methods: the MEMEP 3D variational method, the Finite Element Method (FEM) based on \mathbf{H} formulation [26, 137, 138], and Volume Integral Method (VIEM) based on $\mathbf{A} - \phi$ formulation [139, 140].

The instantaneous power dissipation for both cases is on figure 6.25. All three methods reach excellent agreement. The bulk sample generates higher

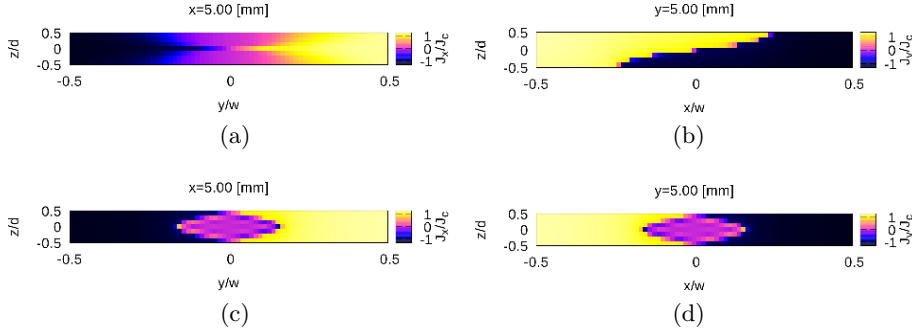


Figure 6.24: The current density penetration to the bulk (a, b) and stack (c, d) at the peak of the applied magnetic field 200 mT with angle $\theta = 60^\circ$ and $n=25$. The J_x (a,c) and J_y (b,d) components of the current density are calculated by MEMEP 3D.

Method	Q_{JE} bulk	Q_{MH} bulk	Q_{JE} stack	Q_{MH} stack
MEMEP 3D	4.58	4.62	3.48	3.50
H-formulation	4.59	4.62	3.47	3.45
VIEM	4.67	4.70	3.56	3.56

Table 6.2: Calculated AC loss per cycle for bulk and stack under tilted applied magnetic field by different methods MEMEP 3D, FEM, VIEM. The AC loss is calculated by integrating [72] the instantaneous power dissipation $\mathbf{E} \cdot \mathbf{J}$ (Q_{JE}) and magnetization loops (Q_{MH}).

AC loss than the stack, since bulk is more saturated with the screening current, and hence there is a bigger zone with $|\mathbf{J}|$ above J_c , which contributes to the AC losses. The total AC loss per cycle for bulk and stack [90] is in table 6.2. The AC losses results agree very well between models. The power loss is calculated by instantaneous power dissipation as

$$Q_{JE} = 2 \int_{T/2}^T \int_V \mathbf{J} \cdot \mathbf{E} dV dt, \quad (6.2)$$

where V is the volume of the superconductor and the AC loss is calculated at a half cycle multiplied by 2, being T the period. The magnetization loop is calculated by

$$Q_{MH} = \int m_a dH_a, \quad (6.3)$$

where H_a is the applied field and m_a is the magnetic moment in the applied field direction [90].

The magnetization loops for bulks and stacks perfectly overlap by all three methods [figure 6.26 (a) bulk (b) stack]. The stack of tapes does not

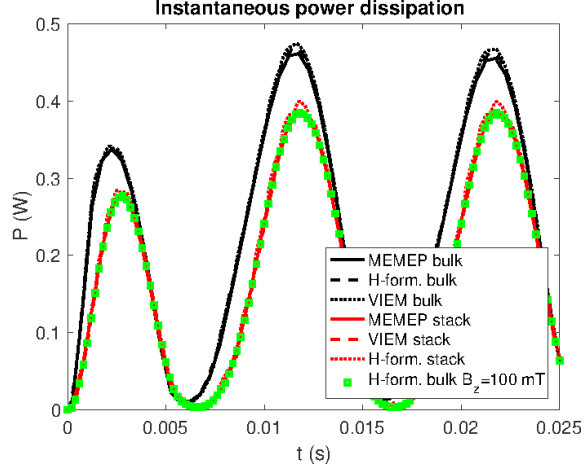


Figure 6.25: The instantaneous power dissipation calculated by MEMEP 3D, FEM and VIEM method for bulk and stack samples with tilted applied magnetic field. The results shown great accuracy between each method.

have M_x component because J_z is equal to zero, and hence the magnetization loops close in the xy plane. The magnetization component M_z is slightly higher because the screening current is only in the xy plane. The M_x component in the bulk is small because of the thin sample.

The J_y current density penetration into the bulk is on figure 6.27. The current density distribution is in plane $z = 0$ mm with three line positions $y = 0, y = 0.2w, y = 0.4w$. The methods confirm again very nice agreement.

6.4 Cross-field demagnetization of cubes.

Superconducting bulks are a potential alternative to permanent magnets. Bulk magnetization is higher compared to permanent magnets. The world record of trapped field, B_t , is 17.6 T [36] with big effort to developed such material [109, 141]. The transverse or cross-fields demagnetize the bulks, decrease the trapped field. There are demagnetization studies based on modelling by 2D H formulation and comparison with experiments [142, 143]. Experimental and 2D and 3D modelling study of hybrid structures such as ferromagnetic and superconducting material can be found in [31], where the superconductor is cylindrical. The comparison of 2D models based on A and H formulation with Brandth and Mikitik theory are in [144]. However, demagnetization of a cube sample is still not well understood. Since the finite sample includes end effects, a full 3D accurate model is necessary.

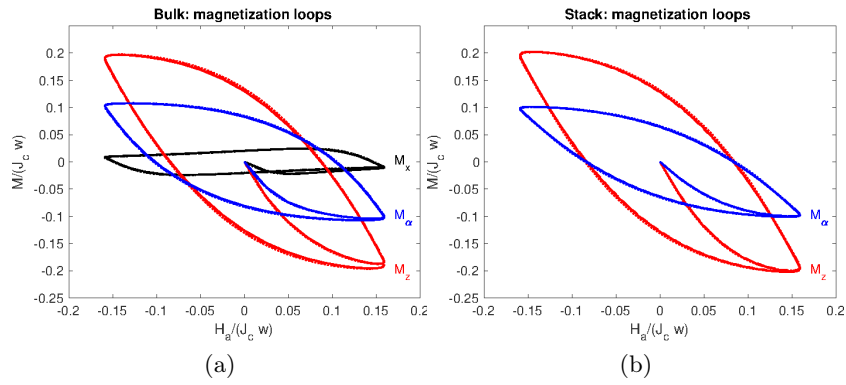


Figure 6.26: The magnetization loops of (a) bulk and (b) stack sample under tilted applied field.

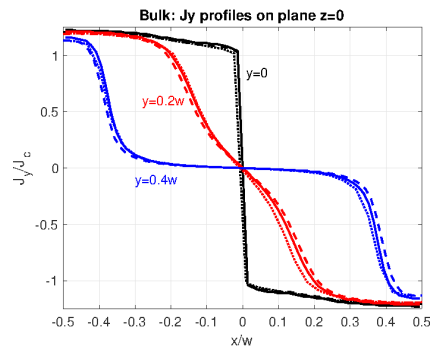


Figure 6.27: The J_y profile at the plane $z = 0$ at three different positions $y/w = 0, 0.2, 0.4$ at the peak of the applied field of 200 mT.

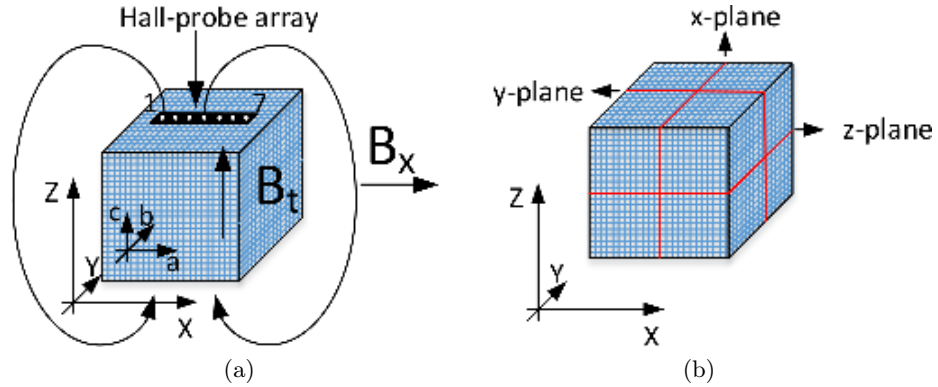


Figure 6.28: The geometry of the cube for the demagnetization process. (a) The trapped field B_t is along the z axis and the applied cross-field ripples are along the x axes. The Hall probe array is parallel to the ripples, sensing B_z in the z direction. (b) The cross mid planes for colour maps with current density components are at planes $x=3$ mm, $y=3$ mm and $z=3$ mm.

Size[mm]	6x6x6
J_c [A/m ²]	$2.6 \cdot 10^8$
$B_{az,max}$ [T]	1.3
Ramp rate[mT/s]	13
Relaxation[s]	900
E_c [V/m]	1e-4
f_{ax} [Hz]	0.1,1
B_{ax} [mT]	35,73,130
n[-]	30

Table 6.3: The input parameters for the cross-field demagnetization modelling based on the real sample and measurement.

6.4.1 Modelling of cross-field demagnetization

The demagnetization model of a bulk by cross-fields follows the demagnetization measurements in section 4.4. The input parameters are in table 6.3. The critical current density is chosen as $J_c = 2.6 \cdot 10^8$ A/m², in order to have the same trapped field as in the measurements. We magnetize the sample by an applied field in the z axis with triangular wave-form and ramp rate of 13 mT/s. A transverse field of various amplitudes and frequencies is applied along the x axes after the relaxation time of 900 s [figure 6.28(a)].

Figure 6.29 shows the calculated magnetization inside the sample and

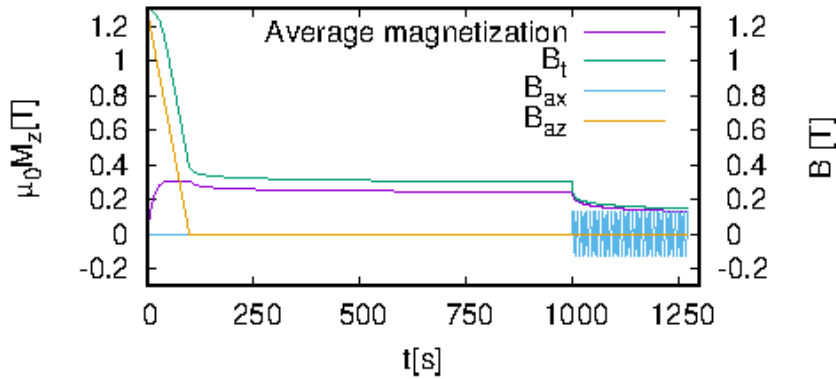


Figure 6.29: The figure of the entire magnetization and demagnetization process over time with wave-forms of the applied field B_{az} and ripple B_{ax} . The magnetization inside the sample and trapped field at $100 \mu m$ above the sample are reduced by the applied ripples.

trapped field $100 \mu m$ above the sample for the entire demagnetization process. The model assumes ripples with frequency 0.1 Hz and maximum amplitude, B_{ax} of 130 mT . The ripples demagnetize the sample and decrease the trapped field, B_t . The B_t value at the end of the relaxation time is 0.3 T and the peak of the trapped field is on figure 6.30. The peak decreases with the applied transverse field B_{ax} and it is shifted aside from the center. The trapped field peak is shifted with the first positive peak of the transverse applied field on figure 6.30 (blue line at time 1002.5 s). The second negative peak of B_{ax} decreases the trapped field further and it shifts the trapped field peak to the opposite side along the x axes [figure 6.30 red line at time 1007.5 s].

The calculation result of MEMEP 3D is compared with Finite Element Method model made by Mark Ainslie in Comsol Multiphysics 5.2a based on H - formulation [26, 110, 145, 146]. Both methods agree very well and small discrepancy in FEM model comes from the linear (first-order) elements and coarse mesh (figure 6.30).

Figure 6.31 shows the current distribution crossing the mid-planes $x=3\text{mm}$, $y=3\text{mm}$, $z=3\text{mm}$ [sketch 6.28(b)] at the end of the relaxation time and at the first positive and tenth positive peak of the applied field ripples.

The cube is fully saturated by screening current at the end of the relaxation time [figure 6.31(a)(d)]. The screening current is perpendicular to the applied field B_{az} according to the CSM. Since the sample is fully saturated, the J_z component vanishes [figure 6.31(g)], and hence there are only J_x and J_y components of the current density. The current density reduces its value to $0.8J_c$ during relaxation.

The ripples are applied along the x axis, and hence the new screening current penetrates into the sample with current loops in the yz plane, in-

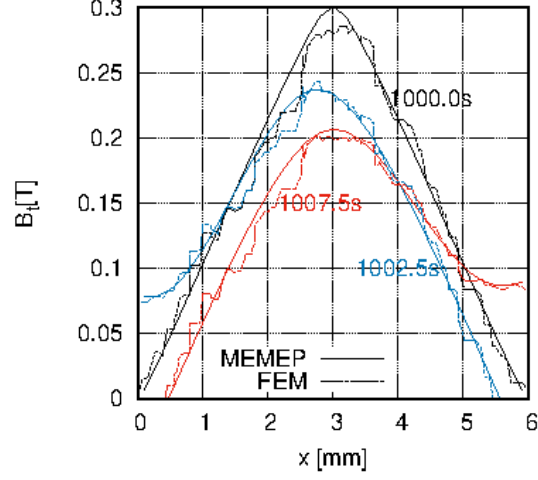


Figure 6.30: The peak of the trapped field at the end of the relaxation time of 900 s, which follows the 100 s long magnetization by B_{az} . The red and blue lines are trapped fields at 1002.5 s (at first positive peak of ripple) and 1007.5 s (at first negative peak of ripple).

ducing J_z and J_y . The following situation is at the first positive peak of the ripple. J_z smoothly penetrates the z plane [figure 6.31(h)] and it erases J_x at the edges [figure 6.31(b)]. J_y changes the previous distribution in the y plane and it creates an “S” shaped front, which was already predicted by 2D models [144]. This J_y induced from the ripples increases the value at the corners up to J_c [figure 6.31(e)]. The ripple field does not only create the S-shaped current front in the y -plane but it also changes the direction of the screening current loops, from in the xy plane for the initial magnetization currents to the yz plane for the de-magnetization currents. Then, the ripple fields induce a J_z component.

The current distribution under the following ripples keep the same penetration behaviour. The J_z penetration is sharper after ten cycles of the ripples B_{ax} [figure 6.31(c)], therefore J_x in the plane $x = 3$ mm is erased at the edges with sharp step to zero [figure 6.31(c)]. After 10 cycles with bipolar peaks of B_{ax} , there appears a separate zone at the center with the first magnetization currents due to B_{az} and a screening current zone due to B_{ax} [figure 6.31(f)]. The central zone is with value around $0.9J_c$, which corresponds to the value of J_x at the plane $x = 3$ mm [figure 6.31(c)].

The entire demagnetization of the cube and the current distribution is the origin of the decreased trapped field and the asymmetry of the trapped peak 6.30. The FEM model confirmed the same current path and behaviour. The comparison of both methods with J_y distribution in the plane $y = 3$ mm at the first positive peak of the ripples is on figure 6.32.

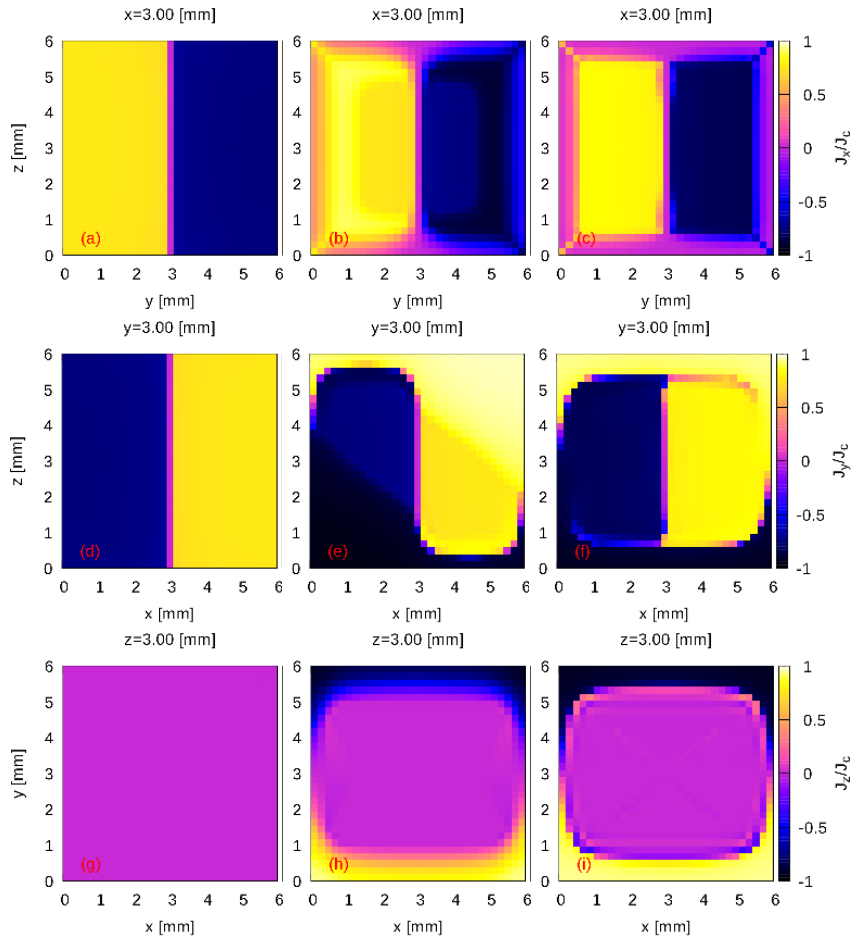


Figure 6.31: The current density distribution in the cube during the demagnetization process. The profiles at 1000 s (end of relaxation) (a),(d),(g), at 1002.5 s (end of first demagnetizing peak) (b),(e),(h) and at 1012.5 s (end of 10th demagnetizing peak) (c),(f),(i). The J_x component is in the top row, J_y in the mid row and J_z at bottom row. The positions of the cross planes are on figure 6.28(b).

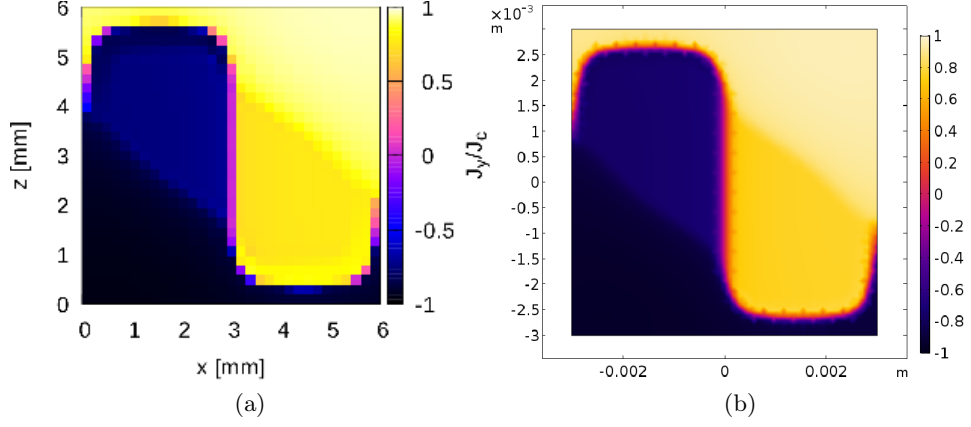


Figure 6.32: The J_y distribution in plane $y = 3$ mm at the time 1002.5 s (after the first demagnetizing cycle). (a) The MEMEP 3D and (b) The FEM model, which confirmed the current distribution during demagnetization process.

6.4.2 Experiments and comparison to modelling

The real sample is prepared and measured according to section 4.4. The reduction of the trapped field by cross-field ripples is on figure 6.33. The ripples are with frequency 0.1, 1 Hz and maximum applied fields $B_{ax} = B_t/2, B_t/4, B_t/8$ ($B_{ax} = 130, 70, 35$ mT). The trapped field decreases rapidly during first a few cycles of ripples, because the current distribution changes mostly at that time. The higher frequency reduces faster the trapped field during the 10-minute measurements, due to the higher number of ripples compared to the case of 0.1 Hz. The trapped field decreases with increasing the applied ripple fields.

The dependence of the reduced trapped field on the number of ripple cycles is on figure 6.34. The curve for the ripples with amplitude 35 mT shows nice agreement for both frequencies. The applied field, B_{ax} , with higher amplitude presents 10% frequency dependence caused by the finite power-law exponent. Higher frequency ripples induce higher electric fields, and hence the screening current is with higher amplitude and lower penetration depth [90, 147–149].

The complete signal of the trapped field measured by the 7 Hall-probe sensors is on figure 6.35. The position of the sensor array is on figure [6.28(a)]. The sensor 1 and 7, which are on both sides of the array confirms, the asymmetry of the trapped field, because the phase of the trapped field is shifted by 90° .

Finally, we compare the measurements with both models, MEMEP 3D and FEM (figure 6.36). The models agree very well in low applied fields, B_{ax} , at frequency 0.1 Hz [figure 6.36(a)] and 1 Hz [figure 6.36(b)]. The applied

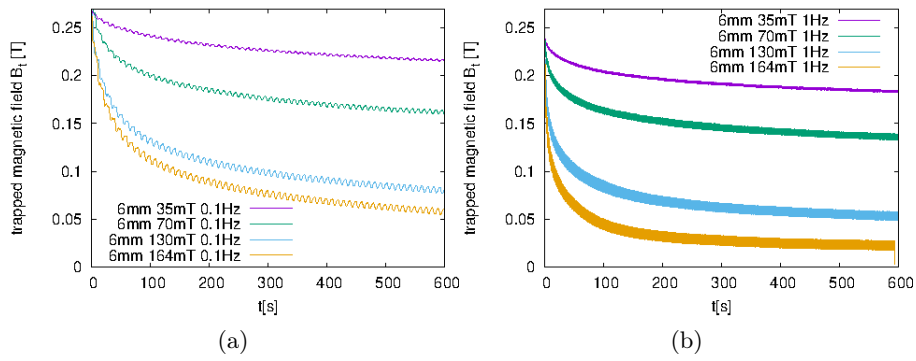


Figure 6.33: The measurements of the trapped field with various applied fields ripples $B_{ax} = 35, 70, 130, 164$ mT and frequency (a) 0.1 Hz, (b) 1.0 Hz. The measurements details in section 4.4.

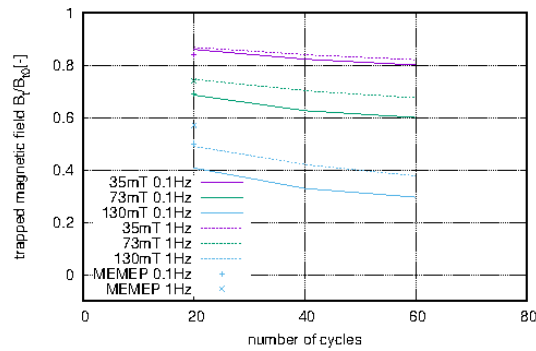


Figure 6.34: The trapped magnetic field dependence on the number of ripple cycles. The ripples of 35 mT are compared with MEMEP 3D model.

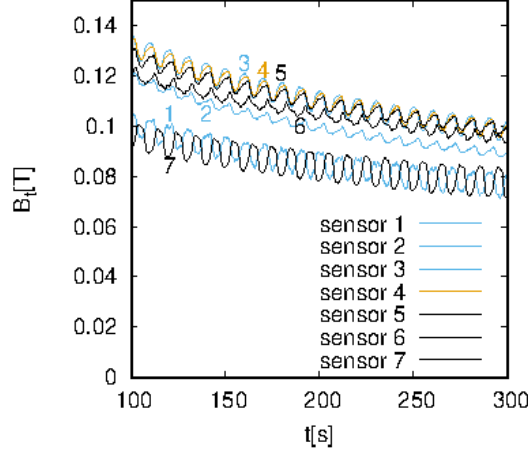


Figure 6.35: The trapped magnetic field profile during demagnetization measurement by the 7 Hall-probe sensor array. The measurements confirmed the asymmetry of the peak. The signal from Hall-probe sensors is marked by 1 to 7 from left to right side of the array.

field ripples with amplitude $B_{ax} = B_t/2$ show higher deviation, which can be explained by inaccurate power-law exponent and the constant J_c assumption. The FEM model shows even higher deviation compare to the MEMEP 3D. The deviation comes from coarse mesh and (first-order) elements.

6.5 Anisotropic force-free effects

Superconductors could be isotropic (LTS or MgB_2 wires, even though MgB_2 is intrinsically anisotropic material) and anisotropic (YBCO or REBCO) materials. Isotropic superconductors are with homogeneous properties in any direction. However, anisotropic superconductors change properties according the direction of the current flow. The anisotropy can be distinguished between “intrinsic”, “de-pinning” and “force-free” anisotropy.

The intrinsic anisotropy is due to different internal material properties. For example, REBCO films and bulks present lower critical current density when current flows in the c -plane compared to the ab plane. The second kind of anisotropy is de-pinning anisotropy, which comes from anisotropic pinning of vortices [84] and depends on the applied field direction. The de-pinning anisotropy is important to for increase J_c by improving pinning centers at perpendicular applied field with \mathbf{J} .

The other type of anisotropy is due to force-free effects, which depend on the angle between magnetic field \mathbf{B} and current density \mathbf{J} . Force-free effects are due to flux cutting and crossing [34, 150, 151], which appear when the local magnetic field is not perpendicular to the current density. They appear

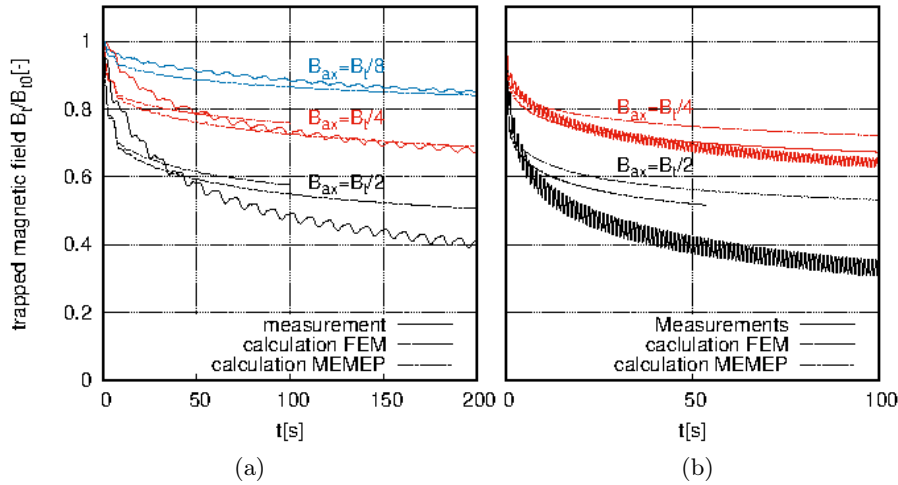


Figure 6.36: The comparison of the cube demagnetization by cross-field B_{ax} measurements with the MEMEP 3D and FEM models. The measurements with ripples of (a) 0.1 Hz and (b) 1 Hz. The models and measurements agree for low ripple amplitudes.

in all superconducting power applications with parallel magnetic fields. The macroscopic anisotropy study of superconductors developed new models such as the Double Critical State Model [150] with a later improvement by the General Double Critical State Model [152]. Branth and Mikitik introduce the Extended DCSM [153] and Badia and Lopez introduce Elliptic CSM [125, 154]. The summarization of the previous models is in [151].

On the other hand, all models must be validated by experiments such as on REBCO tapes by de-pinning anisotropy [65–71], Bi223 [155, 156] or iron based superconductors [157–160]. There is a wide database of tapes characterizations with J_c results [161]. The correction of I_c in measurements is in [162, 163]. There are other more exotic causes of anisotropy, such as that due to flux channelling in vicinal films [164, 165], although this particular case could be considered as intrinsic anisotropy.

The force-free effects in infinite samples are still not fully understood, and hence light on this topic is important for material characterization and for optimization of power devices. The force-free effects are important for rotating machines containing bulks and magnets containing transposed cables like CORC or ROEBEL.

The 3D modelling tool with all finite size and force free effects is necessary. The following two sections are focused on modelling force-free effects in thin films and prisms with various applied magnetic fields angles. The anisotropic results are compared with the isotropic case.

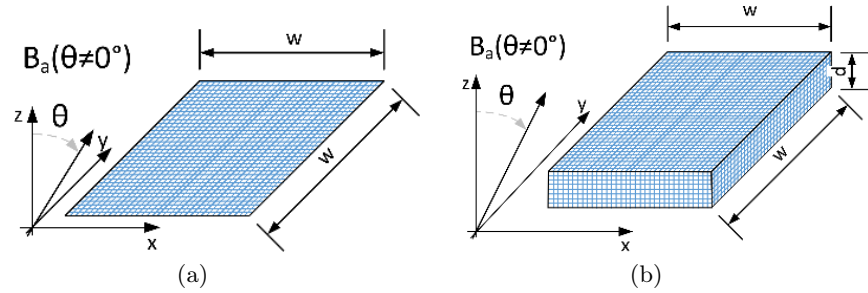


Figure 6.37: The geometry of the modelling sample with non-zero applied field angle θ . (a) Thin film with width w . (b) Prism with thickness d and width w .

6.5.1 Finite superconducting thin film with anisotropic $\mathbf{E}(\mathbf{J})$ relation

This section studies the magnetization of thin films with various angles of the applied magnetic field. The MEMEP 3D modelling tool can take any $\mathbf{E}(\mathbf{J})$ relation into account, and hence the tool models force-free effects in thin films. The results here discuss all effects and current paths under several applied magnetic field angles θ .

The modelling situation of a square thin film magnetization is on figure 6.37(a). The sample dimensions are $12\text{mm} \times 1\mu\text{m}$ ($w \times d$), where w is the width and d is the thickness. The anisotropic power law parameters are the perpendicular critical current density $J_{c\perp} = 3 \cdot 10^{10} \text{ A/m}^2$, parallel critical current density $J_{c\parallel} = 9 \cdot 10^{10} \text{ A/m}^2$ and a realistic n value of 30. The alternating applied magnetic field is with constant z component of 50 mT for any applied field angle θ . The applied field angles are $0^\circ, 45^\circ, 60^\circ$ and 80° . The minimization algorithm uses the magnetic field from the previous time step $B_{(t-\Delta t)}$, because the anisotropic power law is not well defined in very low or zero local magnetic field (section 2.5). Therefore, the results for the remanent state are shifted to the next time step with non-zero applied field. The error in calculation is decreased by higher number of total time steps per cycle, and hence lower Δt .

AC power device situation

Next, we assume that the applied field is sinusoidal of 50 Hz frequency, in order to simulate the situation of a power device.

The first modelling case is with angle $\theta = 0^\circ$ and applied field amplitude of 50 mT. The screening current density gradually penetrates symmetrically into the sample from the edges already under the small applied field of 19.1 mT [figure 6.38(a)]. The modelling sample presents the same features as the isotropic case in figure 5.7. Actually, the current penetration process is

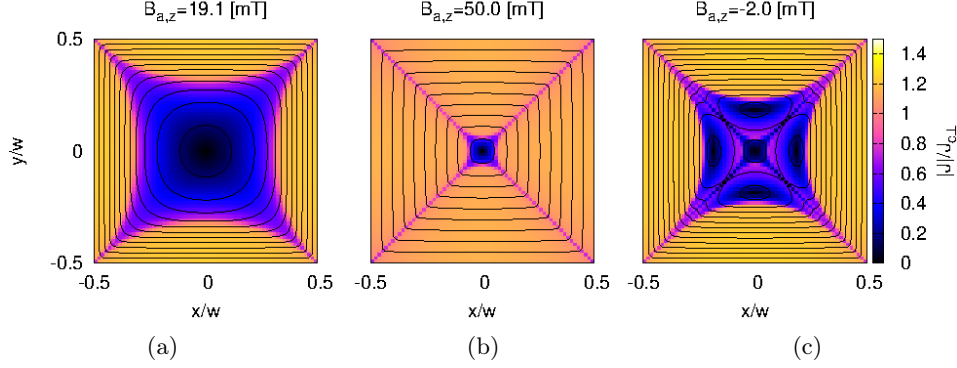


Figure 6.38: The gradual penetration of the current density into the thin film with the sinusoidal applied field $B_a=50$ mT. The applied field angle is $\theta=0^\circ$ and frequency 50. The anisotropic power law is with n value 30 and $J_{c\parallel} = 3J_{c\perp}$. The penetration \mathbf{J} is the same as in isotropic case on figure 5.7.

identical. The almost saturated state is on figure [6.38(b)] and the remanent state is on figure[6.38(c)]. The screening current density is around $J_{c\perp}$, because the applied field angle and self-field are perpendicular to the sample surface.

The second modelling case is with angle $\theta = 45^\circ$ and the applied magnetic field amplitude is 70.7 mT, in order to keep $B_{a,z}$ component is equal 50 mT. The small B_{az} of 19.1 mT creates significant penetration of the screening current into the sample [figure 6.39(a)]. In the colour maps there appear regions with $|\mathbf{J}| \approx J_c$ with \mathbf{J} parallel to x or y axes. We refer to the current density in these regions as J_x and J_y components, respectively. The penetration depth of J_y is the same as the previous case with $\theta = 0^\circ$. However, the J_x component of the current density is around $2 \times J_{c\perp}$. The reason is that the applied field is slightly aligned with the current density, enabling $|\mathbf{J}|$ between $J_{c\perp}$ and $J_{c\parallel}$. The higher J_x density with lower penetration depth is enough to close the current loops with J_y component with larger penetration depth. The sample is almost fully saturated with screening current density at the peak of applied field [figure 6.39(b)] with the same penetration depth of J_y as in case $\theta = 0^\circ$. The J_x component shows the highest value at the penetration front, where self-field, which is perpendicular to the sample is lower than behind the penetration front. The remanent state shows complex current paths with another penetration front due to the currents induced during the decrease of applied field. This front presents half the penetration depth [figure 6.39(c)]. The applied field is zero, which leaves as non-zero only the perpendicular self-field. Therefore, the previously enhanced current density by $J_{c\parallel}$ is reduced to a value around $J_{c\perp}$.

The next cases with angles $\theta = 60^\circ$ and 80° (applied fields 100 and 287.9

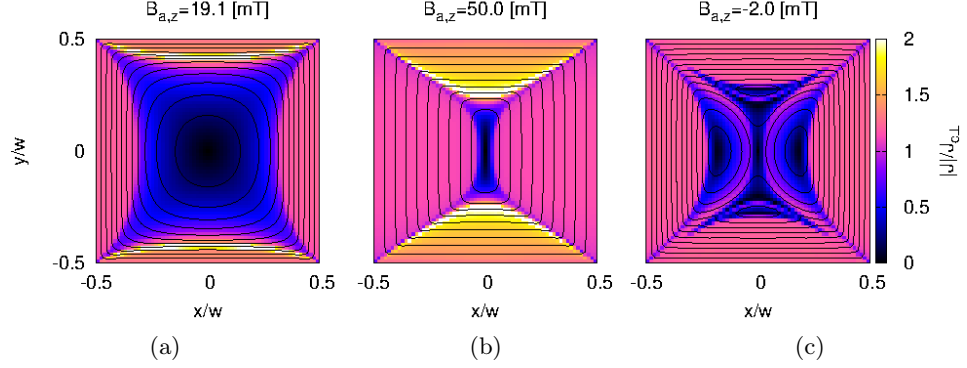


Figure 6.39: The gradual penetration of the current density into the anisotropic thin film with the sinusoidal applied field amplitude $B_a=70.7$ mT. The applied field angle is $\theta=45^\circ$.

mT, respectively) show the same magnetization behaviour with the similar current paths. The J_y screening current reaches the same penetration depth as for $\theta = 0^\circ$. For $B_{a,z}=19.1$ mT, [figures 6.40(a) and 6.41(a)]. The J_x component increases the value with applied field angle θ and decreases the penetration depth. The saturation state [figure 6.40(b) and 6.41(b)] at the peak of applied field shows again the same penetration depth of J_y up to the sample center, because of the θ -independent $B_{a,z}$. J_x increases with the angle θ and reaches a value around $J_{c\parallel}$. For both cases at the remanent state, there appears a reduction of J_x component to $J_{c\perp}$, because the self-field of the thin film is perpendicular [figure 6.40(c) and 6.41(c)].

In the following, we analyse the hysteresis loops with anisotropic power law [figure 6.42(a)]. The magnetization increases with angle θ , since this angle increases the current density in part of the sample. The remanent state is with zero applied field and non-zero self-field, which reduces $|\mathbf{J}|$ to $J_{c\perp}$, since the self-field is perpendicular. Therefore, the hysteresis loops present a magnetization drop around the remanent state. The thin film model allows only the J_x and J_y components of the current density, and hence the only non-zero component of the magnetization is M_z .

We also consider the case with isotropic power law, for comparison. Now, we assume frequency 50 Hz and applied field 50 mT. The magnetization loops are on figure 6.42(b). The magnetization loop is the same for any applied field angle θ , since J_c does not depend on the angle of local magnetic field and the z component of the applied field is the same. The magnetization loop for any angle is the same as the anisotropic case with angle $\theta=0^\circ$ [figure 6.42(a)].

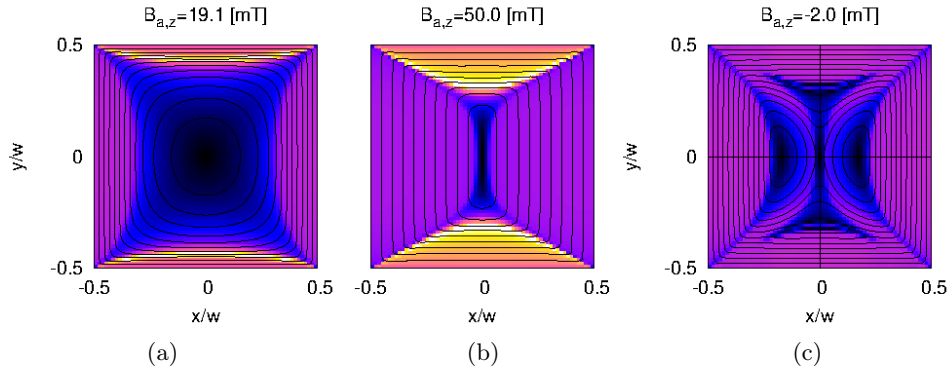


Figure 6.40: The gradual penetration of the current density into the anisotropic thin film with the sinusoidal applied field of amplitude $B_a=100$ mT. The applied field angle is $\theta=60^\circ$.

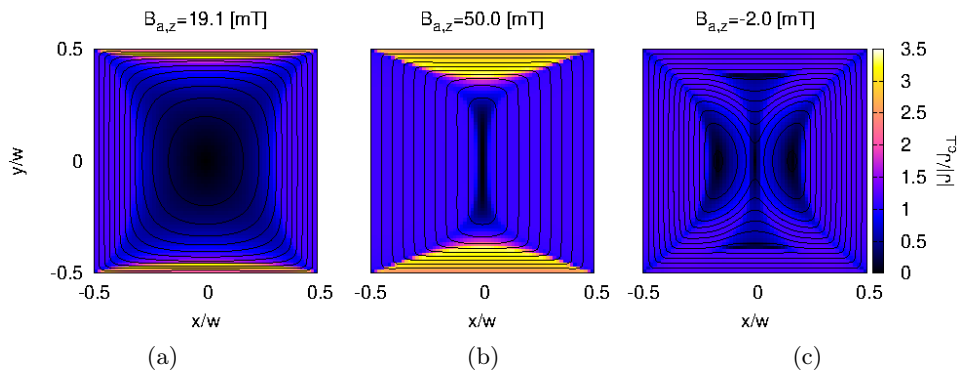


Figure 6.41: The gradual penetration of the current density into the anisotropic thin film with the sinusoidal applied field of amplitude $B_a=287.9$ mT. The applied field angle is $\theta=80^\circ$.

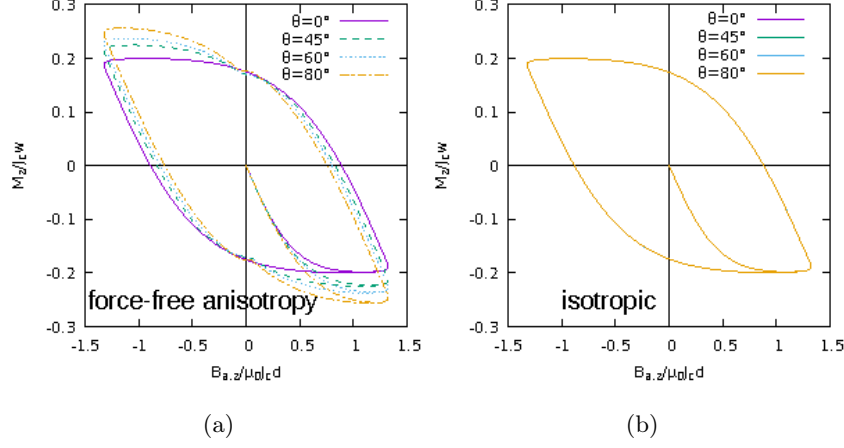


Figure 6.42: The magnetization loops with (a) anisotropic and (b) isotropic power law. The sinusoidal applied field amplitude is of $B_{a,z}=50$ mT with frequency of 50 Hz and n value 30.

Magnets situation

Next, we discuss an applied field situation similar to magnets. The applied field frequency is 1 mHz with triangular waveform, which is the same as slow ramp up of the magnet. The applied field amplitude is with $B_{amz}=150$ mT for any angle θ , being the total amplitude $B_{am} = B_{amz} / \cos \theta$. The power law exponent n is 100, and hence the $\mathbf{E}(\mathbf{J})$ curve is approximately the same as the Critical State model (section 2.6). The hysteresis loops are on figure 6.43. The magnetization increases with angle θ and the saturation state is with a flat curve. The flat part comes from the constant ramp, causing a constant induced electric field. In addition, the high n value reduces current density to the value equal or below $J_{c\perp}$. The remanent state shows the same magnetization drop as previous cases, since the local magnetic field contains the self-field only.

The last thin film model includes a magnetic field dependence like Kim model. The Kim model is well defined even for low local magnetic fields, and hence the minimization process uses the applied field, $B_a(t)$, from the same time step to calculate $\mathbf{J}(t)$. Therefore, at the remanent state $B_a = 0$ [figure 6.44(b)]. We assume the Kim model parameters of $m=0.5$, $B_0=20$ mT and $J_{c0} = 10^8$ A/m². The applied field amplitude is with constant z component of 300 mT for all angles θ . The magnetization increases with the angle θ [figure 6.44(a)]. The $J_{c\perp}$ and $J_{c\parallel}$ depend on the local magnetic field, and hence the current density and magnetization decreases with the applied field, being the lowest at the remanent state. Increasing the applied field saturates the sample already at $B_{az} = 40$ mT. The case of $\theta = 80^\circ$ shows the

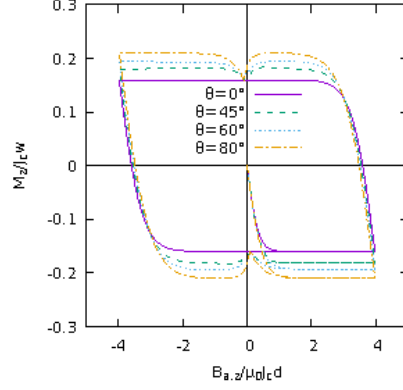


Figure 6.43: The magnetization loops with anisotropic power similar to the magnet situation. The input parameters of magnetization loops are the triangular applied magnetic field of amplitude $B_{a,z}=150$ mT with frequency 1 mHz and n value 100.

highest magnetization even with the highest applied field; since \mathbf{B} and \mathbf{J} are more aligned, causing J_c closer $J_{c\parallel}$. The perpendicular self-field at remanent state reduces $|\mathbf{J}| \approx J_c$, and hence in the magnetization loop there appears a drop down to the same value as the case of $\theta = 0^\circ$. The remanent state shows a smooth drop, because of the self-field and the high number of time steps per cycle of 480 [figure 6.44(b)].

6.5.2 Prism with various thicknesses and anisotropic $\mathbf{E}(\mathbf{J})$ relation

The prism model contains all components of $\mathbf{T}(T_x, T_y, T_z)$, compared to the thin film, where only T_z was non-zero. Now the current path due to the force-free effects presents a more complex behaviour.

Detailed analysis for a given thickness

The modelling sample size is $12 \times 12 \times 1$ mm with applied field angle θ in $x-z$ plane [figure 6.37(b)]. In order to keep the magnetization comparable with the thin film, we take the same sheet current density $J_c d$, being d the sample thickness. Then, the critical current densities of the 1 mm thick sample are $J_{c\perp} = 3 \cdot 10^7$ A/m² and $J_{c\parallel} = 9 \cdot 10^7$ A/m² with n value 30. The sinusoidal applied magnetic field is the same as the thin film in the previous section, and hence the amplitude is 50, 70.7, 100, 287.9 mT for angles 0, 45, 60, 80°, respectively, with frequency 50 Hz. The minimization uses the anisotropic $\mathbf{E}(\mathbf{J})$ relation and the magnetic field from the previous time step $\mathbf{B}_{(t-\Delta t)}$.

The first magnetization case is with the angle $\theta = 0^\circ$. The average current density over the thickness is on figure 6.45 (b). The screening current density

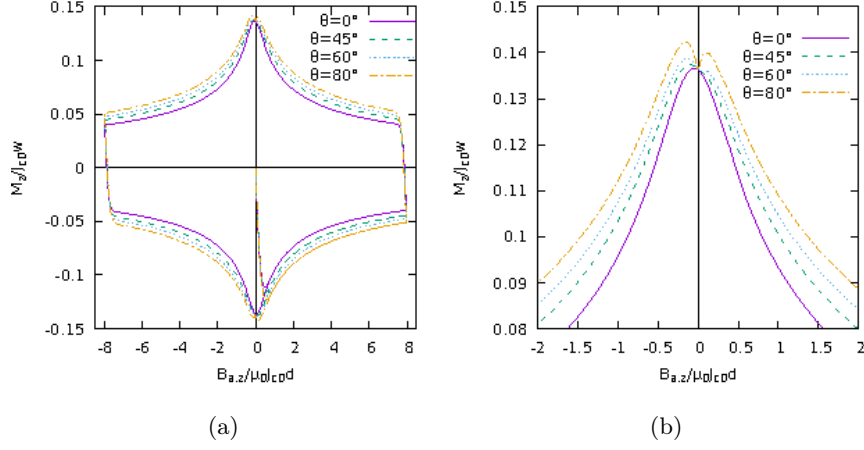


Figure 6.44: (a) The magnetization loops with anisotropic $\mathbf{E}(\mathbf{J})$ relation and magnetic depend like Kim model with parameters $m=0.5$, $B_0=20$ mT and $J_{c0} = 10^8$ A/m². The triangular applied field is of 300 mT amplitude and frequency 1 mHz. (b) Zoom on the magnetization loop at the remanent state.

fully penetrates into the sample at the peak of applied field of 50 mT. The thin film model [figure 6.45(a)] agrees with the prism. The slight difference in the penetration depth comes from the relatively coarser mesh in the prism in the z -plane. The thin film mesh contains $65 \times 65 \times 1$ (4225) cells, which is 4096 degrees of freedom. However, the prism requires a fully 3D model and the mesh contains $31 \times 31 \times 15$ (14415) cells, resulting in around 40000 degrees of freedom. The prism contains 10 times more degrees of freedom, but each z plane contains 4.5 times less cells. A more precise comparison is by cross-sectional current density [figure 6.45(c),(d)]. The cross-section lines are in the middle of the sample and two time steps with instant applied field 19.1 and 50 mT. The current profiles agree with thin film with small deviation. The prism is fully saturated with the screening current density, and hence there is no J_z component. The applied field is perpendicular to the sample surface, therefore magnitude of the current density is around $J_{c\perp}$.

The second modelling case is with angle 45° and applied field amplitude of 70.7 mT. The average current density at the peak of applied field [figure 6.46(b)] agrees very well with the thin film case [figure 6.46(a)]. The cross-sectional comparison confirms the same penetration depth. The J_y component of the screening current is always perpendicular to the applied field, and hence the current density value is around $J_{c\perp}$ [figure 6.46(d)]. However, the J_x component is slightly parallel to the applied field, and hence force-free effects start to play a role. The alignment of \mathbf{J} and \mathbf{B} in the x direction increases the current density of J_x to a value around $2J_{c\perp}$ [figure 6.46(c)].

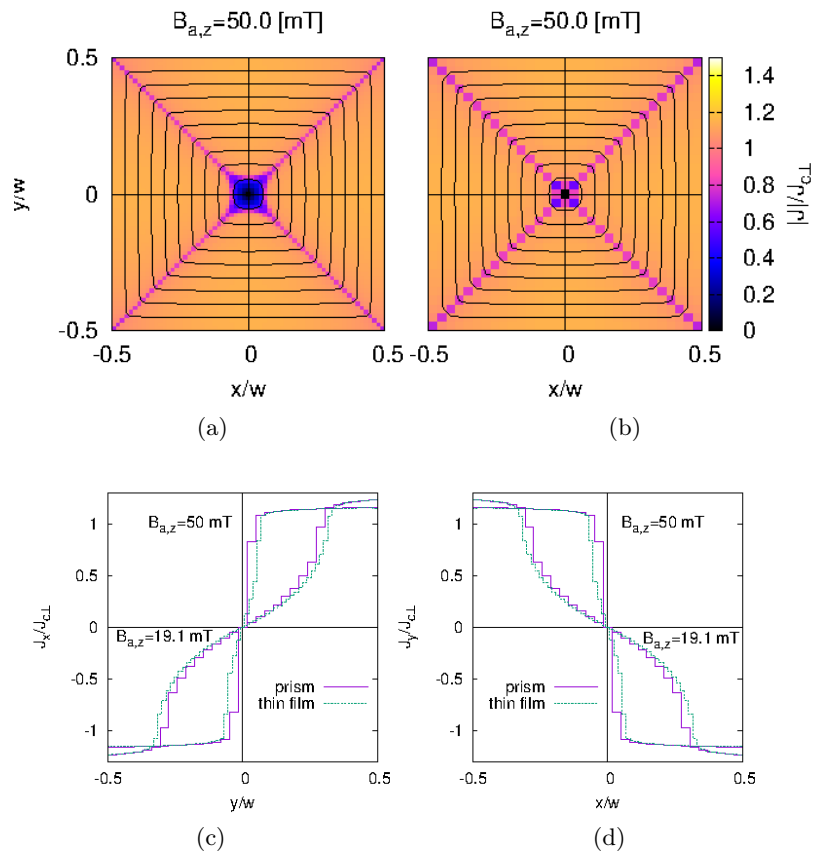


Figure 6.45: The penetration of the current density at the peak of applied field of 50 mT in (a) thin film and (b) prism. The prism colour map is with average current density over thickness. The current density in the mid cross-section is shown with (c) J_x and (d) J_y components.

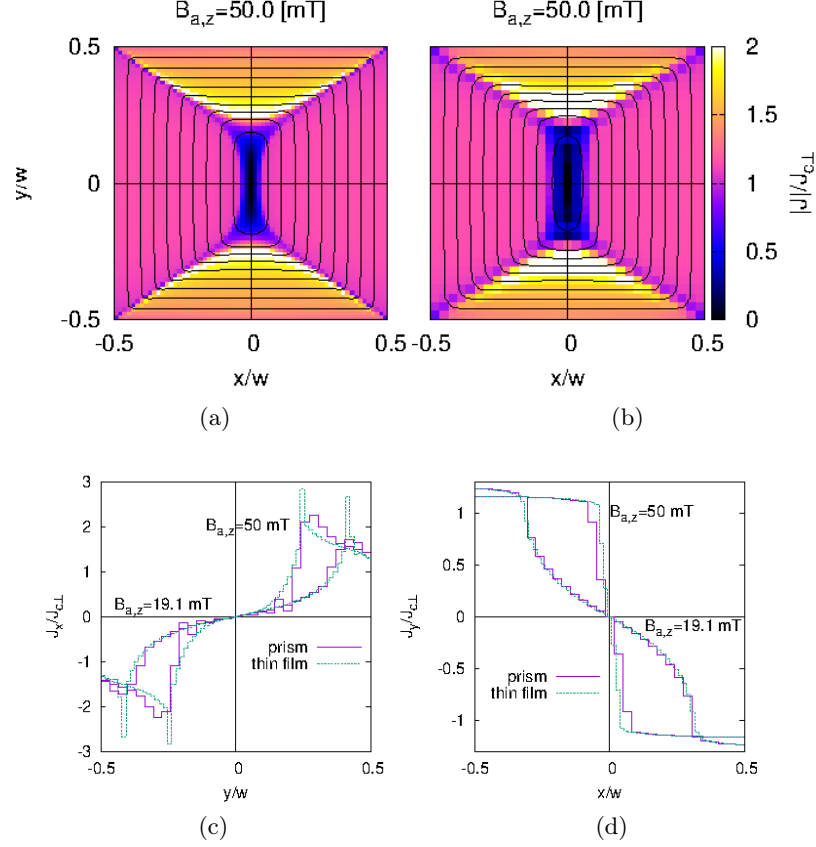


Figure 6.46: The penetration of the thickness-average current density at the peak of applied field of 70.7 mT with angle $\theta = 45^\circ$ in (a) thin film and (b) prism. The current density in the mid cross-section is shown for the (c) J_x and (d) J_y components.

The cause is that for $\mathbf{J} \parallel \mathbf{B}$, $|\mathbf{J}|$ could reach up to $J_{c\parallel}$, being 3 times higher than $J_{c\perp}$ in our case. The thin film model shows J_x at the penetration front with value around $2.8J_{c\perp}$. The prism model does not show the same sharp peak, because the prism mesh contains thicker cells, which smear out the results.

The third case is with $\theta = 60^\circ$ and applied field amplitude of 100 mT. The colour maps of current density show small deviation between the thin film [figure 6.47(a)] and the prism [figure 6.47(b)]. The J_x component at the cross-sections [figure 6.47(c)] agrees very well with thin film. The J_x value increases with angle θ and reaches $2.5J_{c\perp}$. The tilted applied field increases the J_z component of the screening current density to a value around $J_{c\perp}$ and reduces J_y . The lower penetration depth of J_y at the peak of applied field confirms the cross-sectional current density [figure 6.47(d)].

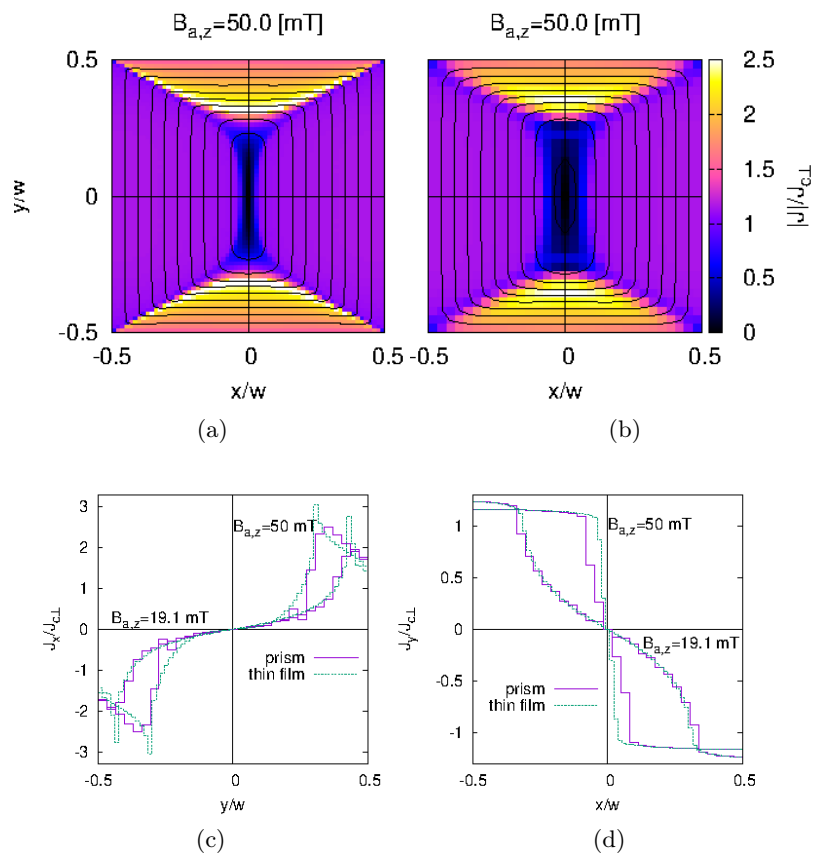


Figure 6.47: The penetration of the thickness-average current density at the peak of applied field of 100 mT with angle $\theta = 60^\circ$ in (a) thin film and (b) prism. The current density in the mid cross-section is shown for the (c) J_x and (d) J_y components.

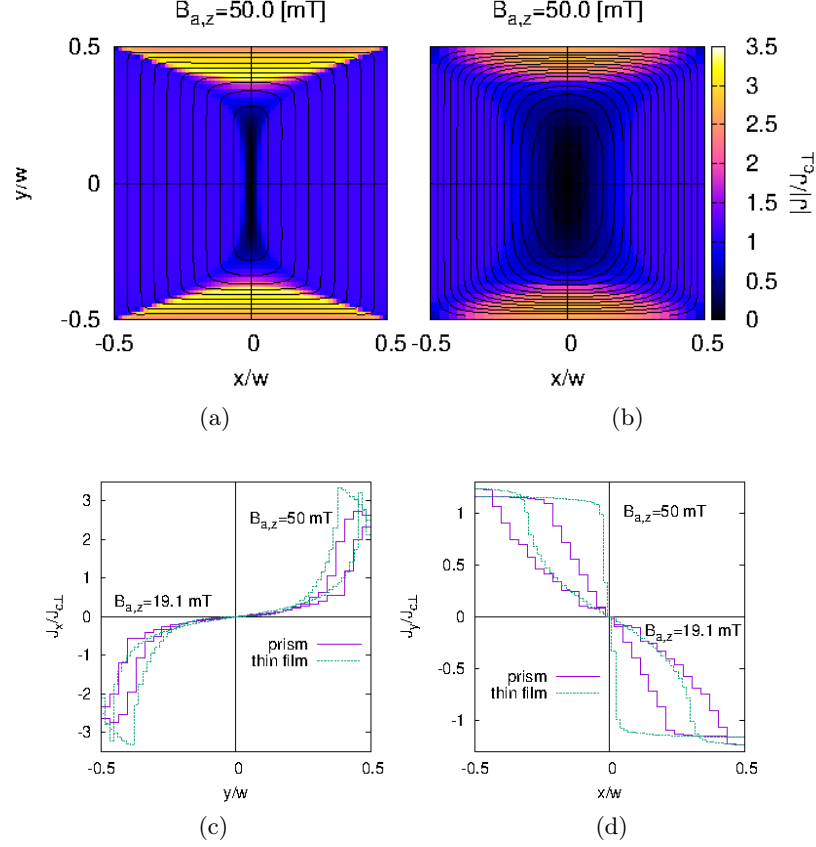


Figure 6.48: The penetration of the thickness-average current density at the peak of applied field of 287.9 mT with angle $\theta = 80^\circ$ in (a) thin film and (b) prism. The current density in the mid cross-section is shown for the (c) J_x and (d) J_y components.

The last calculation, for angle $\theta = 80^\circ$ and applied field of 287.9 mT, shows the same magnetization behaviour like the case of 60° . The model presents even lower penetration depth in J_y [figure 6.48(b),(d)], because of tilted applied field angle. The J_x component shows slightly lower penetration depth from the same reason [figure 6.48(c)].

The 3D current distribution in the prism with perpendicular applied field is on figure 6.49. The sample is fully saturated with screening current [see figure 6.49(a),(b) central maps], and hence J_z is zero [figure 6.49(c)]. The applied and local magnetic fields are perpendicular to the screening current flowing only in the z plane, and hence there is no $|\mathbf{J}| \approx J_{c\parallel}$.

The 3D current distribution with angle $\theta = 80^\circ$ is on figure 6.50. The penetration depth of J_x is around 1 mm and the current density is around $J_{c\parallel}$ [figure 6.50(a)], because the current is almost parallel with the applied

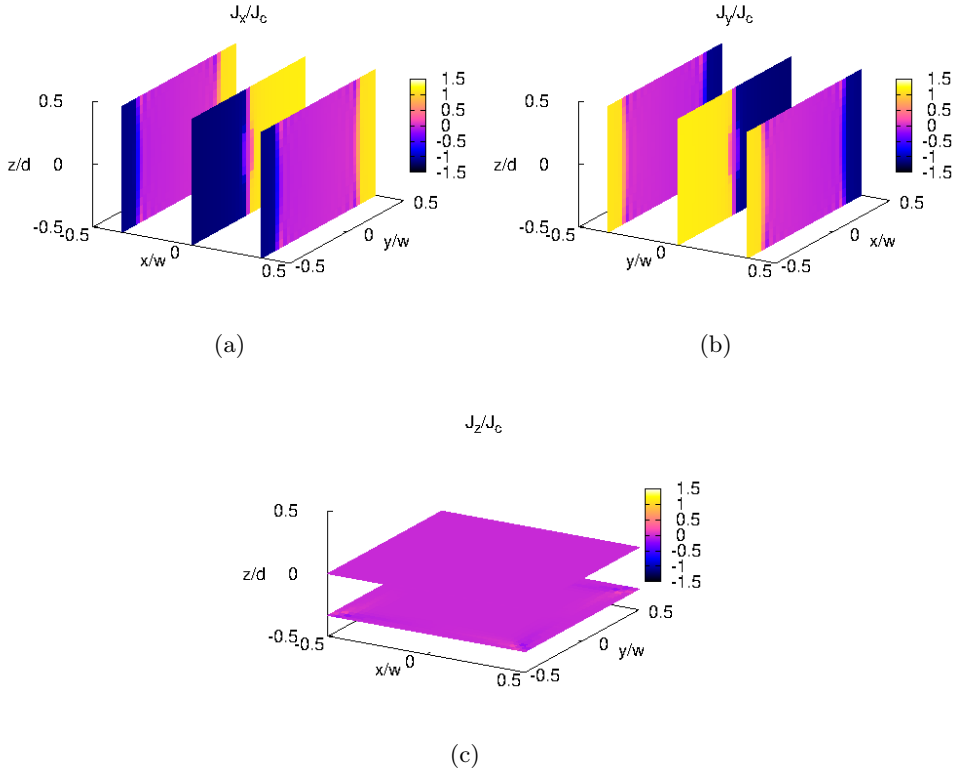


Figure 6.49: The 3D current density in the prism with applied field 50 mT and angle $\theta = 0^\circ$. The maps are for screening current density components (a) J_x , (b) J_y and (c) J_z .

field. The highest penetration depth is for J_y . The J_y value is around the $J_{c\perp}$, since the applied field is perpendicular with \mathbf{J} and the border between positive and negative sign is aligned with the applied field direction [figure 6.50(b)]. The J_z component is around the $J_{c\perp}$ with the same penetration depth as J_x [figure 6.50(c)].

The remanent state is on figure 6.51. The penetration depth of the J_x component is lower than it was at the peak of applied field. J_x is with opposite sign, because of the opposite sign of the ramp of the applied field. The value of J_x is around $J_{c\parallel}$, since the applied field is almost zero and local magnetic field is parallel with J_x [figure 6.51(a)]. The increase of J_x close to remanent causes the peak in the hysteresis loop after the remanent state. Comparing to figure 6.50, J_y swapped the sign with amplitude around $J_{c\perp}$ [figure 6.51(b)]. The lower penetration depth close to the corners is because of not complete reversal of the screening current, since the applied field is lower than the minus peak. J_z also swaps the sign and keeps the value around $J_{c\perp}$.

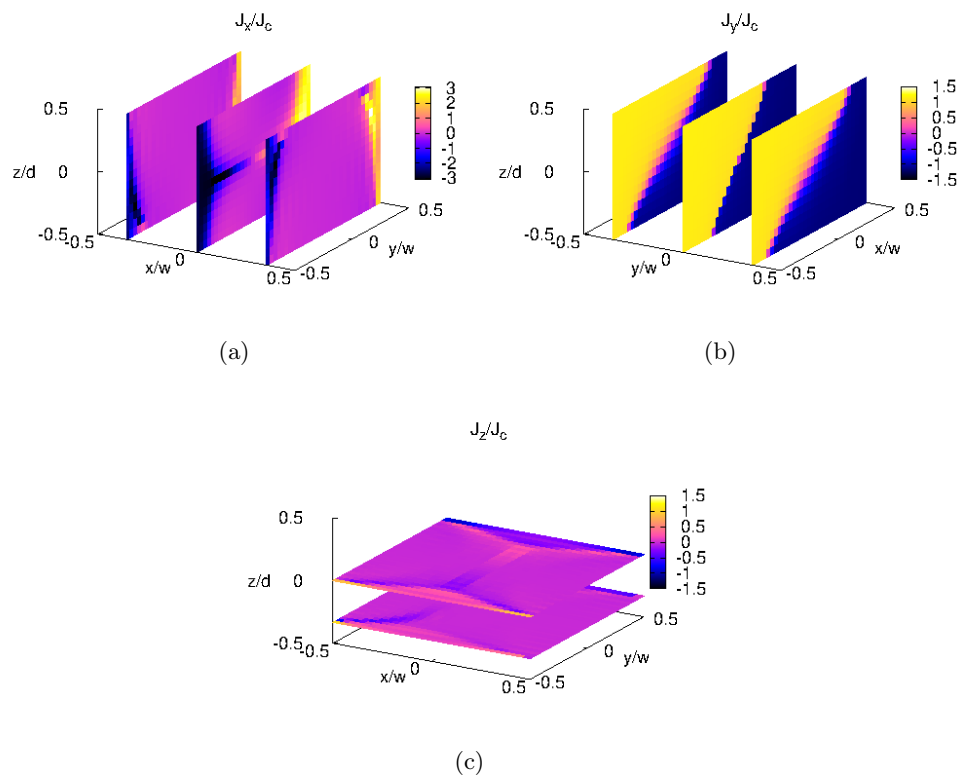


Figure 6.50: The 3D current density in the prism with the applied field 287.9 mT and angle $\theta = 80^\circ$. The maps are for screening current density components (a) J_x , (b) J_y and (c) J_z .

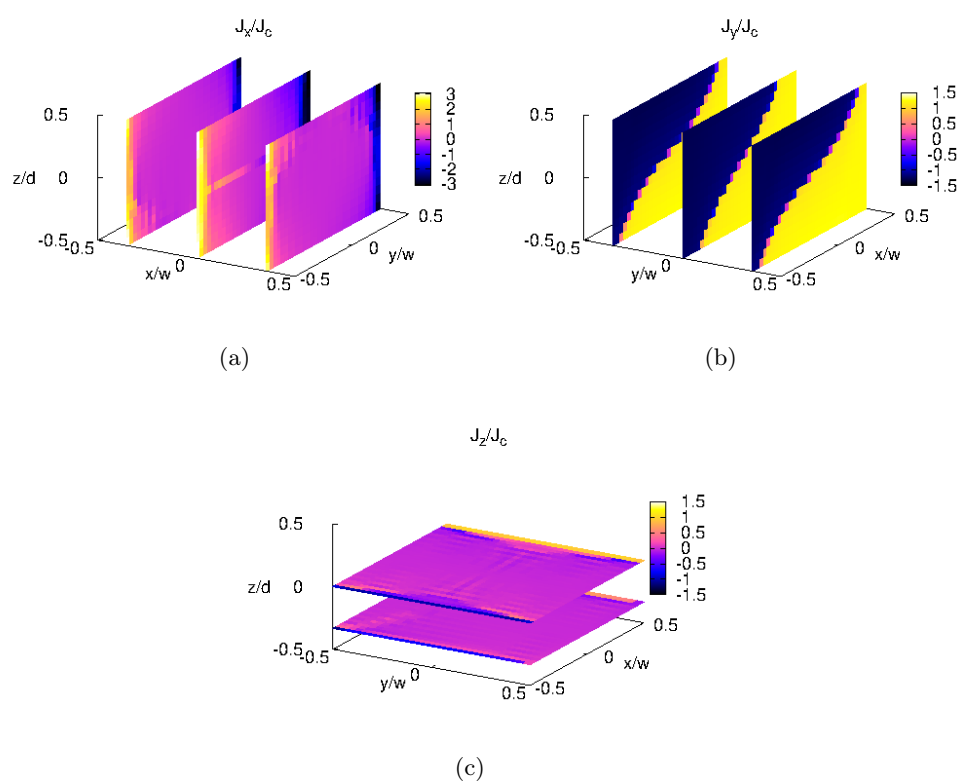


Figure 6.51: The 3D current density in the prism with angle $\theta = 80^\circ$ at the remanent state. The maps are for the screening current density components (a) J_x , (b) J_y and (c) J_z .

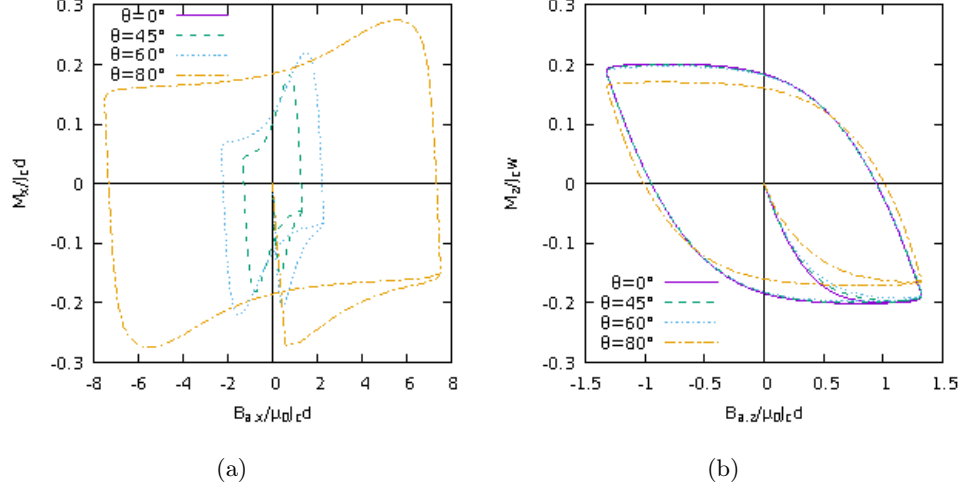


Figure 6.52: The magnetization loops with isotropic power law and various angles θ of the applied field. The magnetization components (a) M_x and (b) M_z are shown.

Comparison between anisotropic and isotropic effects

The comparison of the magnetization loops between isotropic and anisotropic $\mathbf{E}(\mathbf{J})$ relations reveals all finite size and force-free effects.

The first loops are for isotropic power law [figure 6.52]. The magnetization M_z decreases with the applied field angle [figure 6.52(b)] and M_x increases with the angle [figure 6.52(a)]. The reason is that the magnetization loops are roughly normal to the applied field direction. Then, the angle θ tilts the magnetization loops, tilting also the magnetization. The saturation magnetization according the CSM for square slab is $M_s = J_c w / 6$ [166]. For the prism, the saturation magnetization is $M_s \approx 0.17 J_c w$. The model with power law exponent $n = 30$ allows the current density value above J_c , and hence the saturation magnetization is slightly higher than the analytical prediction $M_s \approx 0.2 J_c w$.

For the anisotropic case, M_z increases with the applied field angle [figure 6.53(b)]. The magnetic field aligns with the current density in part of the sample. This increases $|\mathbf{J}|$ towards $J_{c\parallel}$, rising the magnetization. M_x shows almost the same behaviour as for the isotropic case, increasing with applied field angle [figure 6.53(a)]. The anisotropic case presents a small peak for both magnetization components M_x and M_z . The self-field is dominant at the remanent state and it is parallel to the top and bottom surface of the sample. The alignment of \mathbf{J} and local \mathbf{B} increases $|\mathbf{J}|$ to $J_{c\parallel}$, and hence there appears a peak in the magnetization loop. The following increase of the applied field magnitude changes the local magnetic field, and hence reduces

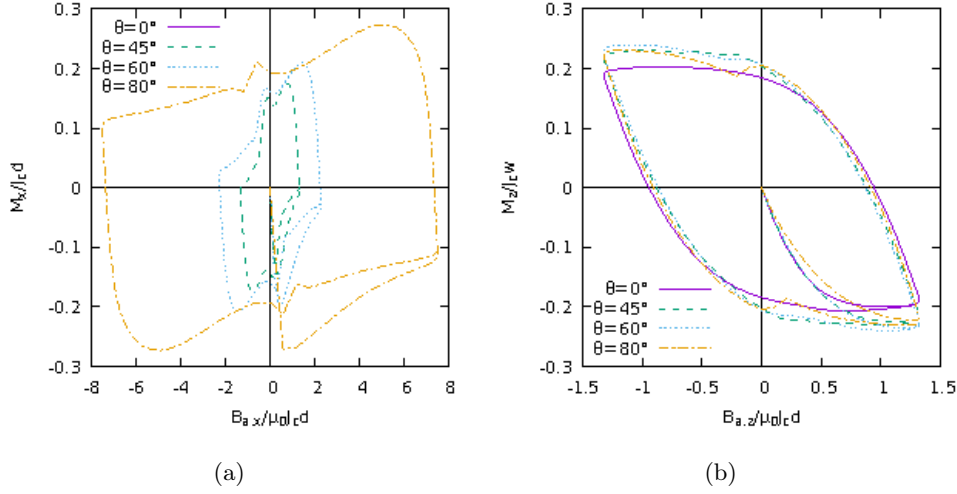


Figure 6.53: The magnetization loops with anisotropic power law and various angles θ of the applied field. The magnetization components (a) M_x and (b) M_z are shown.

$|\mathbf{J}|$ to $J_{c\perp}$ and M_x , M_z components [figure 6.53(a),(b)].

Detailed study of thickness effects

The other comparison of magnetization loops is with the sample of various thickness and applied field angle $\theta = 80^\circ$. The prism with $1 \mu\text{m}$ thickness [the curve on figure 6.54(b)] is modelled by the thin film approximation. M_x increases with thickness [figure 6.54(a)], because thicker sample contains higher J_z . The $M_z/J_c d$ component saturates to higher values for very low thickness of the sample. The normalized magnetization actually decreases with the thickness because of the tilt in the magnetization loops, raising M_x but decreasing M_z [figure 6.54(b)]. The magnetization difference is only a finite size effect. This confirms the correctness of the MEMEP 3D model. All the samples with different thickness in the range $1\mu\text{m}$ - 1mm show the same magnetization loop of M_z [figure 6.55]. With small differences due to the finite thickness. The cases of $1 \mu\text{m}$ (thin film approach) and 0.1 mm (several cells over the thickness) present the same M_z curve.

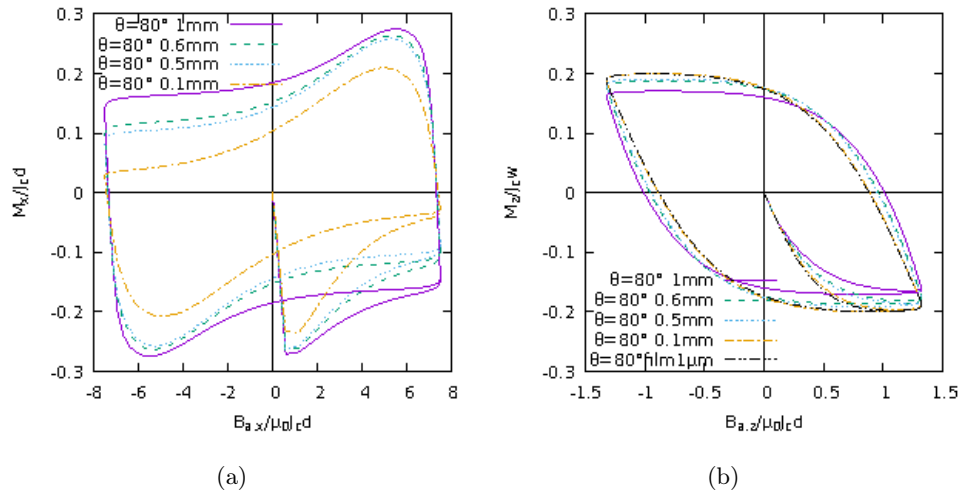


Figure 6.54: The magnetization loops with isotropic power law and various thicknesses for an applied field angle $\theta = 80^\circ$. The magnetization components (a) M_x and (b) M_z are shown.

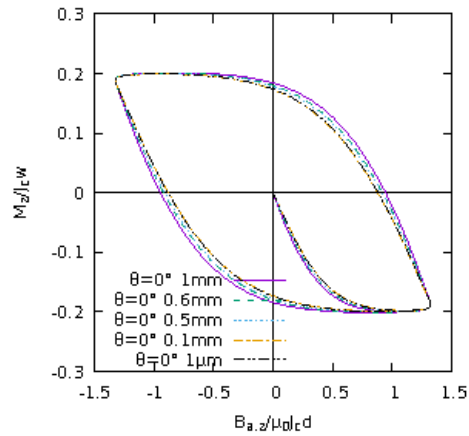


Figure 6.55: The magnetization loops with isotropic power law and various thicknesses for perpendicular applied field ($\theta = 0^\circ$).

Chapter 7

Conclusion

The full 3D calculation methods for non-linear superconducting materials is necessary, in order to explain all finite size effects. The finite size effects help to understand and optimize superconductors in power applications, since power devices are of finite size. The finite size effects are also important to interpret characterization measurements. Modelling methods needs to include any dependence like $J_c(B)$ and any $\mathbf{E}(\mathbf{J})$ relation in order to provide realistic predictions, which is very demanding. Moreover, it must handle full 3D mesh with a lot of elements to fulfil accurate results in relatively short times.

This thesis developed and implemented a novel 3D modelling method for the electromagnetic response of superconductors. We developed a new variational method in \mathbf{T} formulation, where \mathbf{T} is the effective magnetization. The variational method is called Minimum Electro Magnetic Entropy Production MEMEP 3D. The entire calculation method is implemented in a modelling tool written in C++ language with parallel computing hierarchy. The parallel computing efficiency is tested on a computer cluster with efficiency of 80%. Parallel computing enabled modelling cases with high resolution of elements in the mesh, higher number of cycles and total time steps per cycle. The numerical method included sectors, in order to drastically reduce the computing time, even without parallel programming, and hence the electromagnetic response of the superconducting sample is modelled in a relatively short time. The results of the models confirmed the correctness of the 3D functional, which is the core of the entire MEMEP 3D method, the solution being unique without saddle points.

The electromagnetic response of the superconducting sample was verified by analytical solutions by 2D cross-sectional models for infinitely long thin films and thin disks. We also modelled a square film with constant J_c and $J_c(B)$. The predictions were for the current density profiles, hysteresis loops and qualitative gradual penetration of the current density under perpendicular applied magnetic field.

The modelling geometry is focused on thin films and cubic samples, which are of high importance. Nowadays superconducting commercial tapes are around $1\ \mu\text{m}$ thick and stacks of tapes are an alternative to permanent magnets. The comparison between the AC loss measurement on two soldered superconducting tapes and model showed high accuracy of 96%. The coupling loss is the dominant part at low applied fields below 10 mT. The current state of the modelling tool can accurately model AC loss in tapes of up to 10 filaments. Elongated cells allowed to prolong the sample length far beyond the length of the usual sample for characterization measurements of the tapes.

The general magnetization model of the cubic bulk found the existence of the J_z component, which does not appear in superconducting cylinders or fully saturated square samples. The fundamental study improved the general knowledge of magnetization on rectangular prism samples, which is still not fully understood. The HTS modelling work group chose our magnetization model of cubic bulk as a benchmark model for other modelling method on the international HTS modelling workshop 2016. Further study about prism magnetization of different thickness proofed a remaining J_z component of $0.3J_c$ even for aspect ratios as low as 0.1. Study presented analytical fit of magnetization on aspect ratio dependence between infinitely thin film and slab of 97% accuracy.

International collaboration resulted in a further comparison of three modelling methods. The modelling cases were bulk and stack magnetization with tilted applied fields. The comparison further validated the MEMEP 3D method. The calculation of AC loss, hysteresis loops and 3D current path have been performed by MEMEP 3D, FEM and VIEM with great accuracy of results.

Demagnetization by cross-fields of cubic bulks are important for power applications as potential alternative to permanent magnets. The model showed the asymmetry of the trapped magnetic field during demagnetization process, which confirmed the measurements on my stay in Cambridge University. The comparison agreed very well for low fields but showed a small deviation at high cross-fields of 150 mT. The origin of the asymmetry in the trapped field can be explained by the 3D current penetration, which was partially predicted by 2D cross-sectional models. The full 3D current path was confirmed with a FEM model. The MEMEP 3D method modelled the entire magnetization and demagnetization process with more than 500 time steps.

The modelling method can take any $\mathbf{E}(\mathbf{J})$ relation, and hence the last study in this Thesis was on force-free effects in thin films and bulks with anisotropic power law. The force-free effects are important for power applications where superconducting tapes are expose to rotating magnetic fields or in magnets with 3D transpose cables, and also for sample characterisation. The force-free effects appear when current density and local magnetic fields

are not perpendicular as it is explained by the Elliptic Double Critical State Model. The force-free effects study on the thin film with tilted applied field revealed zones of value $|\mathbf{J}| \approx J_{c\parallel}$ and reduction at remanent state back to $|\mathbf{J}| \approx J_{c\perp}$. The reduction came from the self-field, which was always perpendicular to the film samples without applied field, and hence no "enhanced" J_c is present. The magnetization of the M_z component increased with the applied field angle, because of the $J_{c\parallel}$ influenced by the alignment of \mathbf{J} and \mathbf{B} . The anisotropic bulk presented even more complex force-free effects. The enhanced current density created a peak after the remanent state in the hysteresis loop. The thickness study on the isotropic prism showed an increase of M_z with decreasing the thickness, since the screening current is squeezed towards the xy plane, and hence there is a reduction of the M_x component.

In conclusion, the variational method was verified by analytical predictions and measurements. The MEMEP 3D method showed very good results of new findings with high speed calculation time. However, there is still room for improvement of the calculation time. The method can includes any $\mathbf{E}(\mathbf{J})$ relation, and hence the method is promising for another fundamental studies of the 3D superconductors in not fully understood electromagnetic configurations.

Chapter 8

Appendix

8.1 Average vector potential of the self-point interaction.

The minimization process requires the evaluation of the average vector potential 3.32. The self-interaction average vector potential contains a double volume integral, whose solution has to be found. This appendix is focused on the analytical solution of the double volume integral and its correctness.

The elements of the vector-potential interaction matrix between surfaces i and j of the s type ($s \in x, y, z$) is

$$a_{sij} = \frac{\mu_0}{4\pi V_{si} V_{sj}} \int_V d^3r \int_V d^3r' \frac{h_{si}(r) h_{sj}(r')}{|\mathbf{r} - \mathbf{r}'|}, \quad (8.1)$$

where \mathbf{r}, \mathbf{r}' are vector positions of the surfaces. The approximation of the analytical formula for the case of not overlapping surfaces $i \neq j$ are equations (3.37) and (3.40). The undefined double volume integral related to equations (3.36) and (3.39) is

$$f = \int_V d^3r \int_V d^3r' \frac{1}{|\mathbf{r} - \mathbf{r}'|}. \quad (8.2)$$

The full length analytical formula is

$$\begin{aligned}
f = & -\frac{(x^2 + y^2) \sqrt{x^2 + y^2 + z^2}^3}{216} + \frac{x^2 y z^2}{4} \ln \left(y + \sqrt{x^2 + y^2 + z^2} \right) \\
& + \frac{x y^2 z^2}{4} \ln \left(x + \sqrt{x^2 + y^2 + z^2} \right) + \frac{x^2 y^2 z}{4} \ln \left(z + \sqrt{x^2 + y^2 + z^2} \right) \\
& + \frac{(5x^4 + 5y^4 + 4x^2 y^2 - x^2 z^2 - y^2 z^2) \sqrt{x^2 + y^2 + z^2}}{72} - \frac{x^2 y^2 z}{48} - \frac{x^2 y z^2}{48} \\
& + \frac{x^4 y}{12} \ln(x^2 + z^2) + \frac{y z^4}{12} \ln(x^2 + z^2) + \frac{x^4 z}{12} \ln(x^2 + y^2) + \frac{y^4 z}{12} \ln(x^2 + y^2) \\
& + \frac{x y^4}{16} \ln(y^2 + z^2) + \frac{x z^4}{48} \ln(y^2 + z^2) + \frac{x^4 y}{24} \ln \frac{y + \sqrt{x^2 + y^2 + z^2}}{-y + \sqrt{x^2 + y^2 + z^2}} \\
& + \frac{x y^4}{24} \ln \frac{x + \sqrt{x^2 + y^2 + z^2}}{-x + \sqrt{x^2 + y^2 + z^2}} + \frac{x^4 z}{24} \ln \frac{z + \sqrt{x^2 + y^2 + z^2}}{-z + \sqrt{x^2 + y^2 + z^2}} \\
& + \frac{x y z^3}{6} \arctan \frac{y^2 + z^2 + y \sqrt{x^2 + y^2 + z^2}}{x z} + \frac{x y^3 z}{6} \arctan \frac{y^2 + z^2 + z \sqrt{x^2 + y^2 + z^2}}{x y} \\
& - \frac{x y z^3}{3} \arctan \frac{x y}{z \sqrt{x^2 + y^2 + z^2}} - \frac{x y^3 z}{3} \arctan \frac{x z}{y \sqrt{x^2 + y^2 + z^2}} \\
& - \frac{x^3 y z}{6} \arctan \frac{y z}{x \sqrt{x^2 + y^2 + z^2}} \\
& - \frac{x y^4}{16} \ln \left[\left(x^2 + y^2 + x \sqrt{x^2 + y^2 + z^2} \right)^2 + y^2 z^2 \right] \\
& - \frac{x^4 y}{16} \ln \left[\left(x^2 + y^2 + y \sqrt{x^2 + y^2 + z^2} \right)^2 + x^2 z^2 \right] \\
& - \frac{x^4 z}{16} \ln \left[\left(x^2 + z^2 + z \sqrt{x^2 + y^2 + z^2} \right)^2 + x^2 y^2 \right] \\
& - \frac{x z^4}{48} \ln \left[\left(x^2 + z^2 + x \sqrt{x^2 + y^2 + z^2} \right)^2 + y^2 z^2 \right] \\
& - \frac{y z^4}{48} \ln \left[\left(y^2 + z^2 + y \sqrt{x^2 + y^2 + z^2} \right)^2 + x^2 z^2 \right] \\
& - \frac{y^4 z}{48} \ln \left[\left(y^2 + z^2 + z \sqrt{x^2 + y^2 + z^2} \right)^2 + x^2 y^2 \right] \\
& - \frac{\sqrt{x^2 + y^2 + z^2}^5}{45} + \frac{7 \sqrt{x^2 + y^2 + z^2}^3 (-2x^2 - 2y^2 + 3z^2)}{540} \quad (8.3)
\end{aligned}$$

where (x, y, z) are defined by the vector positions r and r' as $x = r - r'_x$, $y = r - r'_y$ and $z = r - r'_z$. We checked that the analytical solution follows mirror symmetry [$f(x, y, z) = f(-x, y, z) = f(x, -y, z) = f(x, y, -z)$] and permutation [$f(x, y, z) = f(y, x, z) = f(x, z, y) = f(z, y, x)$] even if this is not evident in the expression. The solution was checked several times by

comparison with other formulas. However, there exist simplified analytical solutions for a cube element [167] and a square surface [168]. The cube formula is

$$f = \frac{1}{l_{si}} \frac{1 + \sqrt{2} - 2\sqrt{3}}{5} - \frac{\pi}{3} + \ln \left[(1 + \sqrt{2}) (2 + \sqrt{3}) \right], \quad (8.4)$$

where l_{si} is the side of the cube. The thin square surface formula is

$$f = \frac{1}{l_{si}} \frac{1 - \sqrt{2}}{3} + \ln (1 + \sqrt{2}), \quad (8.5)$$

where l_{si} is the side of the surface bigger than its thickness.

8.2 Euler equations of the functional

The variational method is based on a certain functional, whose solution is found by minimization. The minimum of the functional should be the same as the solution of Maxwell differential equations. One needs to proof that the Euler equations of the functional of the extreme correspond to the Maxwell equations and that the extreme is a unique minimum.

A general formalism for this does not exist for functionals of double volume integrals. Since the functional contains double volume integral the Euler an equation needs to be found. The following appendix presents this formalism of the general functional with the double volume integral and it explains the Euler-equations.

The general form of a functional with double volume integral [169] is

$$L[\{u_i\}] = \int_{\Omega} d^n r \int_{\Omega} d^n r' f(\{r_{\alpha}\}, \{r'_{\alpha}\}, \{u_i\}, \{u'_i\}, \{u_i^{(\alpha)}\}, \{u'_i^{(\alpha)}\}), \quad (8.6)$$

where the integer $\alpha \in [1, n]$, u'_i and u_i are functions with variables $\{r'_{\alpha}\}$ and $\{r_{\alpha}\}$, $u'_i = u_i(\{r'_{\alpha}\})$, $u_i^{(\alpha)} \equiv \partial_{\alpha} u_i \equiv \partial u_i / \partial r_{\alpha}$, $u'_i^{(\alpha)} \equiv \partial'_{\alpha} u'_i \equiv \partial u'_i / \partial r'_{\alpha}$.

After Taylor expansion, ([169] A.3) the first variation of double volume integral becomes, using that $\partial_{\alpha}(u_i + \epsilon g_i) = u_i^{(\alpha)} + \epsilon g_i^{(\alpha)}$

$$\begin{aligned} \delta L[\{u_i\}] = & \epsilon \int_{\Omega} d^n r \int_{\Omega} d^n r' \left(\frac{d}{d\epsilon} f(\{r_{\alpha}\}, \{r'_{\alpha}\}, \{u_i + \epsilon g_i\}, \{u'_i + \epsilon g'_i\}, \right. \\ & \left. \{u_i^{(\alpha)} + \epsilon g_i^{(\alpha)}\}, \{u'_i^{(\alpha)} + \epsilon g_i'^{(\alpha)}\}) \right)_{\epsilon=0}, \end{aligned} \quad (8.7)$$

and with

$$\left(\frac{df}{d\epsilon} \right)_{\epsilon=0} = f^{(u_i)} g_i + f^{(u_i^{(\alpha)})} g_i^{(\alpha)} + f^{(u'_i)} g'_i + f^{(u'_i^{(\alpha)})} g_i'^{(\alpha)}. \quad (8.8)$$

Integration by parts rewrite it to

$$\begin{aligned} \delta L[\{u_i\}] &= \epsilon \int_{\Omega} d^n r \int_{\Omega} d^n r' \left[g_i \left(f^{(u_i)} - \partial_{\alpha} f^{(u_i^{(\alpha)})} \right) + \right. \\ &\quad \left. g'_i \left(f^{(u'_i)} - \partial'_{\alpha} f^{(u'_i^{(\alpha)})} \right) \right]. \end{aligned} \quad (8.9)$$

If the functional density is symmetric

$$\begin{aligned} f(\{r_{\alpha}\}, \{r'_{\alpha}\}, \{u_i\}, \{u'_i\}, \{u_i^{(\alpha)}\}, \{u'_i^{(\alpha)}\}) = \\ f(\{r'_{\alpha}\}, \{r_{\alpha}\}, \{u'_i\}, \{u_i\}, \{u'_i^{(\alpha)}\}, \{u_i^{(\alpha)}\}), \end{aligned} \quad (8.10)$$

the first variation becomes

$$\delta L[\{u_i\}] = 2\epsilon \int_{\Omega} d^n r g_i \int_{\Omega} d^n r' \left[f^{(u_i)} - \partial_{\alpha} f^{(u_i^{(\alpha)})} \right]. \quad (8.11)$$

The extreme of the functional appears when for any arbitrary g_i the variation is $\delta L = 0$ and

$$2 \int_{\Omega} d^n r' \left[f^{(u_i)} - \partial_{\alpha} f^{(u_i^{(\alpha)})} \right] = 0. \quad (8.12)$$

This is the Euler equation of the functional. A functional with both single and double volume integrals, is

$$\begin{aligned} L[\{u_i\}] &= \int_{\Omega} d^n r h(\{r_{\alpha}\}, \{u_i\}, \{u_i^{(\alpha)}\}) \\ &+ \int_{\Omega} d^n r \int_{\Omega} d^n r' f(\{r_{\alpha}\}, \{r'_{\alpha}\}, \{u_i\}, \{u'_i\}, \{u_i^{(\alpha)}\}, \{u'_i^{(\alpha)}\}), \end{aligned} \quad (8.13)$$

Following the same step as for the previous functional, the variation of the functional is

$$\begin{aligned} \delta L[\{u_i\}] &= \epsilon \int_{\Omega} d^n r g_i \left[h^{(u_i)} - \partial_{\alpha} h^{(u_i^{(\alpha)})} \right. \\ &\quad \left. + 2 \int_{\Omega} d^n r' \left(f^{(u_i)} - \partial_{\alpha} f^{(u_i^{(\alpha)})} \right) \right]. \end{aligned} \quad (8.14)$$

Then, the Euler equations are

$$h^{(u_i)} - \partial_{\alpha} h^{(u_i^{(\alpha)})} + \left[2 \int_{\Omega} d^n r' \left(f^{(u_i)} - \partial_{\alpha} f^{(u_i^{(\alpha)})} \right) \right] = 0. \quad (8.15)$$

The second variation proves, if the functional extreme, where $\delta L = 0$, is a minimum or not. The second variation of the double volume integral is

$$\begin{aligned} \delta^2 L[\{u_i\}] &= \frac{1}{2} \epsilon^2 \int_{\Omega} d^n r \int_{\Omega} d^n r' \left(\frac{d^2}{d\epsilon^2} f(\{r_{\alpha}\}, \{r'_{\alpha}\}, \{u_i + \epsilon g_i\}, \{u'_i + \epsilon g'_i\}, \right. \\ &\quad \left. \{u_i^{(\alpha)} + \epsilon g_i^{(\alpha)}\}, \{u'_i^{(\alpha)} + \epsilon g'_i^{(\alpha)}\}) \right)_{\epsilon=0}, \end{aligned} \quad (8.16)$$

where the second derivative is

$$\begin{aligned}
\left(\frac{d^2 f}{d\epsilon^2}\right)_{\epsilon=0} &= f^{(u_i u_j)} g_i g_j + f^{(u'_i u'_j)} g'_i g'_j + 2f^{(u_i u_j^{(\beta)})} g_i g_i^{(\beta)} + 2f^{(u'_i u_j^{(\beta)})} g'_i g_j^{(\beta)} \\
&+ f^{(u_i^{(\alpha)} u_j^{(\beta)})} g_i^{(\alpha)} g_j^{(\beta)} + f^{(u'_i^{(\alpha)} u'_j^{(\beta)})} g'_i^{(\alpha)} g'_j^{(\beta)} \\
&+ 2f^{(u_i u'_j^{(\beta)})} g_i g'_j^{(\beta)} + 2f^{(u'_i u_j^{(\beta)})} g'_i g_j^{(\beta)} \\
&+ 2f^{(u_i u'_j)} g_i g'_j + 2f^{(u_i^{(\alpha)} u'_j^{(\beta)})} g_i^{(\alpha)} g'_j^{(\beta)}, \tag{8.17}
\end{aligned}$$

with notation $f^{(u_i u'_j^{(\beta)})} \equiv \partial^2 f / (\partial u_i \partial u'_j^{(\beta)})$. If the functional is symmetric, the second variation is rewritten as

$$\begin{aligned}
\delta^2 L[\{u_i\}] &= \frac{1}{2} \epsilon^2 \int_{\Omega} d^n r \int_{\Omega} d^n r' \left[2f^{(u_i u_j)} g_i g_j + 2f^{(u_i^{(\alpha)} u_j^{(\beta)})} g_i^{(\alpha)} g_j^{(\beta)} \right. \\
&+ 2f^{(u_i u'_j)} g_i g'_j + 2f^{(u_i^{(\alpha)} u'_j^{(\beta)})} g_i^{(\alpha)} g'_j^{(\beta)} \\
&\left. + 4f^{(u_i u_j^{(\beta)})} g_i g_i^{(\beta)} + 4f^{(u_i u'_j^{(\beta)})} g_i g'_j^{(\beta)} \right], \tag{8.18}
\end{aligned}$$

If the functional contains both single and double volume integrals, $\delta^2 L$ becomes

$$\begin{aligned}
\delta^2 L[\{u_i\}] &= \frac{1}{2} \epsilon^2 \int_{\Omega} d^n r \left[h^{(u_i u_j)} g_i g_j + h^{(u_i^{(\alpha)} u_j^{(\beta)})} g_i^{(\alpha)} g_j^{(\beta)} + 2h^{(u_i u_j^{(\beta)})} g_i g_j^{(\beta)} \right] \\
&+ \frac{1}{2} \epsilon^2 \int_{\Omega} d^n r \int_{\Omega} d^n r' \left[2f^{(u_i u_j)} g_i g_j + 2f^{(u_i^{(\alpha)} u_j^{(\beta)})} g_i^{(\alpha)} g_j^{(\beta)} \right. \\
&+ 2f^{(u_i u'_j)} g_i g'_j + 2f^{(u_i^{(\alpha)} u'_j^{(\beta)})} g_i^{(\alpha)} g'_j^{(\beta)} \\
&\left. + 4f^{(u_i u_j^{(\beta)})} g_i g_i^{(\beta)} + 4f^{(u_i u'_j^{(\beta)})} g_i g'_j^{(\beta)} \right]. \tag{8.19}
\end{aligned}$$

Chapter 9

Parameters of the input file

The modelling tool of any method has a lot of input options, and hence user friendly interface is an essential feature. The MEMEP 3D modelling tool contains an input.txt file, which is loaded to the tool at the beginning of the calculation with all possible combinations of the input options. The example of input parameters with short explanation are:

x[m]: - width of the sample

xl[m]: - width of the metallic part in the sample between two filaments

y[m]: - length of the sample

z[m]: - thickness of the sample

nsucx[-]: - number of the cells along the x axes in the superconducting material

mncx[-]: - number of the cells along the x axes in the metal material (tape with filaments)

ncy[-]: - number of the cells along the y axes

ncz[-]: - number of the cells along the z axes (thin film approximation $ncz=1$)

elc[-]: - 0 disable/1 enable, elongated cells in the long sample with aspect ratio >2

tol elc[-]: - tolerance criterion for average vector potential of elongated cells (0.001-default)

Bamax[T]: - maximum amplitude of the applied magnetic field

Bamax1[T]: - maximum amplitude of the applied magnetic cross-field

Bshape[-]: - waveform of the applied field : 0-sinusoidal, 1-ramp down follows by cross-field of Bamax1 and fi1, 2-constant ramp (triangular)

Btrape[-]: - 0 disable/1 enable, calculation of the magnetic field outside of the sample in a certain plane (B-plane)

rcx plane[m]: - x component of the center position of the B-plane (see Btrape)

rcy plane[m]: - y component of the center position of the B-plane (see Btrape)

rcz plane[m]: - z component of the center position of the B-plane (see Btrape)

x plane[m]: - width of the B plane (see Btrape)

y plane[m]: - length of the B plane (see Btrape)

z plane[m]: - thickness of the B plane (see Btrape)
 ncx plane[-]: - number of the cells in the B plane along the x axes (see Btrape)
 ncy plane[-]: - number of the cells in the B plane along the y axes (see Btrape)
 ncz plane[-]: - number of the cells in the B plane along the z axes (see Btrape)
 theta[degree]: - angle of the applied magnetic field from the x axes to the y axes
 fi[degree]: - angle of the applied magnetic field from z axes to the x axes
 fl1[degree]: - angle of the cross-applied magnetic field from z axes to the x axes for Bamax1 and fl
 uni[-]: - type of the mesh: 0-non-uniform, 1-uniform (default), 2-semi-uniform
 rel[-]: - $\mathbf{E}(\mathbf{J})$ relation: 1-isotropic, 2- $J_c(B)$ Kim model, 3-anisotropic, 4-multi-valued CSM
 sym[-]: - type of minimization: 0 no speed up, 1-symmetry (odd input), 2-sectors, 3-sectors with symmetry
 Ec[V/m]: - critical electric field
 Jo[A/m2]: - critical current density
 Jol[A/m2]: - current density for metallic material
 rhoR[ohm*m]: - effective resistivity of the metallic material between filaments
 dl[m]: - width of the metallic joint
 Jcpa[A/m2]: - parallel critical current density
 Jcpe[A/m2]: - perpendicular critical current density
 Bo[T]: - characteristic magnetic field for the Kim model
 N[-]: - power law exponent
 Nl[-]: - power law exponent for metallic material (1-default)
 m[-]: - Kim model exponent
 f[Hz]: - frequency of the applied field
 fl1[Hz]: - frequency of the applied cross-field Bamax1
 ns[-]: - number of the time steps per cycle
 step[-]: - total number of the time steps
 tolJ[-]: - tolerance of the current density(1e-5 default)
 shape[-]: - geometry shape of the sample: 0-square/rectangular, 1-disk/ball, 2-cylinder, 3-tape with filaments, 4-stack of tapes
 num threads[-]: - number of the threads in the computer
 nscx[-]: - number of cells in one sector along the x axes
 nscy[-]: - number of cells in one sector along the y axes
 nscz[-]: - number of cells in one sector along the z axes (thin film approximation nscz=1)
 shift1[-]: - shift by the cells between the first and second set of sectors along the x and y axes
 shift2[-]: - shift by the cells between the second and third set of sectors along

the x and y axes

shiftz1[-]: - shift by the cells between the first and second set of sectors along the z axes

shiftz2[-]: - shift by the cells between the second and third set of sectors along the z axes

Publications

- **M.Kapolka**, E. Pardo “Three-dimensional modeling of macroscopic force-free effects in superconducting thin films and rectangular prisms”, (preprint) arXiv:1803.06342
- **M.Kapolka**, V. M. R. Zermeno, S. Zou, A. Morandi, P. L. Ribani, E. Pardo, F. Grilli “Three-Dimensional Modeling of the Magnetization of Superconducting Rectangular-Based Bulks and Tape Stacks”, IEEE Transactions on Applied Superconductivity (Volume:28, Issue:4), Article number: 8201206, 2018
DOI: 10.1109/TASC.2018.2801322
- **M.Kapolka**, J. Srpacic, D. Zhou, M. Ainslie, E. Pardo, A. Dennis “Demagnetization of cubic Gd-Ba-Cu-O bulk superconductor by cross-fields: measurements and 3D modelling”, IEEE Transactions on Applied Superconductivity (Volume:28, Issue:4), Article number: 6801405, 2018
DOI: 10.1109/TASC.2018.2808401
- E. Pardo, **M.Kapolka**, “3D computation of non-linear eddy currents: Variational method and superconducting cubic bulk”, "J. Comput. Phys." (Volume:344, Issue:), Article number:, 2017
DOI: 10.1016/j.jcp.2017.05.001
- E. Pardo, **M.Kapolka**, “3D magnetization currents, magnetization loop, and saturation field in superconducting rectangular prisms”, "Supercond. Sci. Technol." (Volume:30, Issue:), Article number: 064007, 2017
DOI: 10.1088/1361-6668/aaa5db
- E. Pardo, **M.Kapolka**, J. Kovac, J. Souc, F. Grilli, A. Pique “3D modeling and measurement of coupling AC loss in soldered tapes and striated coated conductors”, **Invited paper** IEEE Transactions on Applied Superconductivity (Volume:26, Issue:3), Article number: 4700607, 2015
DOI: 10.1109/TASC.2016.2523758

Bibliography

- [1] E. Brandt, “Square and rectangular thin superconductors in a transverse magnetic field,” *Phys. Rev. Lett.*, vol. 74, no. 15, pp. 3025–3028, 1995.
- [2] E. H. Brandt, “Electric field in superconductors with rectangular cross section,” *Phys. Rev. B*, vol. 52, no. 21, pp. 15 442–15 457, 1995, DOI: 10.1103/PhysRevB.52.15442.
- [3] ———, “Superconductors of finite thickness in a perpendicular magnetic field: Strips and slabs,” *Phys. Rev. B*, vol. 54, no. 6, p. 4246, 1996.
- [4] J. Rhyner, “Calculation of AC losses in HTSC wires with arbitrary current voltage characteristics,” *Physica C*, vol. 310, no. 1-4, pp. 42–47, 1998.
- [5] M. C. Bouzo, F. Grilli, and Y. Yang, “Modelling of coupling between superconductors of finite length using an integral formulation,” *Supercond. Sci. Technol.*, vol. 17, no. 10, p. 1103, 2004.
- [6] A. Morandi and M. Fabbri, “A unified approach to the power law and the critical state modeling of superconductors in 2d,” *Supercond. Sci. Technol.*, vol. 28, no. 2, p. 024004, 2015.
- [7] J. Vestgård, D. Shantsev, Y. Galperin, and T. Johansen, “Flux distribution in superconducting films with holes,” *Phys. Rev. B*, vol. 77, no. 1, p. 014521, 2008.
- [8] N. Amemiya, Y. Sogabe, M. Sakashita, Y. Iwata, K. Noda, T. Ogitsu, Y. Ishii, and T. Kurusu, “Magnetisation and field quality of a cosine-theta dipole magnet wound with coated conductors for rotating gantry for hadron cancer therapy,” *Supercond. Sci. Technol.*, vol. 29, no. 2, p. 024006, 2016.
- [9] S. Russenschuck, Ed., *1st International Roxie Users Meeting and Workshop ROXIE: routine for the optimization of magnet X-sections, inverse field calculation and coil end design*. Genève: CERN, 1999.

- [10] S. Kurz and S. Russenschuck, “Numerical simulation of superconducting accelerator magnets,” *IEEE Trans. Appl. Supercond.*, vol. 12, no. 1, pp. 1442–1447, 2002.
- [11] L. Prigozhin, “The bean model in superconductivity: Variational formulation and numerical solution,” *J. Comput. Phys.*, vol. 129, no. 1, pp. 190–200, 1996.
- [12] ———, “Analysis of critical-state problems in type-II superconductivity,” *IEEE Trans. Appl. Supercond.*, vol. 7, no. 4, pp. 3866–3873, 1997.
- [13] ———, “Solution of thin film magnetization problems in type-II superconductivity,” *J. Comput. Phys.*, vol. 144, no. 1, pp. 180–193, 1998.
- [14] L. Prigozhin and V. Sokolovsky, “Computing AC losses in stacks of high-temperature superconducting tapes,” *Supercond. Sci. Technol.*, vol. 24, p. 075012, 2011.
- [15] E. Pardo, F. Gömöry, J. Šouc, and J. Ceballos, “Current distribution and ac loss for a superconducting rectangular strip with in-phase alternating current and applied field,” *Supercond. Sci. Technol.*, vol. 20, no. 4, pp. 351–364, 2007.
- [16] E. Pardo, “Modeling of coated conductor pancake coils with a large number of turns,” *Supercond. Sci. Technol.*, vol. 21, p. 065014, 2008.
- [17] E. Pardo, J. Šouc, and L. Frolek, “Electromagnetic modelling of superconductors with a smooth current-voltage relation: variational principle and coils from a few turns to large magnets,” *Supercond. Sci. Technol.*, vol. 28, p. 044003, 2015.
- [18] A. Sanchez, N. D. Valle, E. Pardo, D.-X. Chen, and C. Navau, “Magnetic levitation of superconducting bars,” *J. Appl. Phys.*, vol. 99, no. 113904, 2006.
- [19] G. Via, N. Del-Valle, A. Sanchez, and C. Navau, “Simultaneous magnetic and transport currents in thin film superconductors within the critical-state approximation,” *Supercond. Sci. Technol.*, vol. 28, no. 1, p. 014003, 2015.
- [20] J. Ruuskanen, A. Stenvall, and V. Lahtinen, “Utilizing triangular mesh with MMEV to study hysteresis losses of round superconductors obeying critical state model,” *IEEE Trans. Appl. Supercond.*, vol. 25, no. 3, p. 8200405, 2014, 10.1109/TASC.2014.2365408.
- [21] Y. Zhang, Y. Song, L. Wang, and X. Liu, “Simulation of superconducting tapes and coils with convex quadratic programming method,” *Supercond. Sci. Technol.*, vol. 28, no. 8, p. 085002, 2015.

- [22] J. van Nugteren, B. van Nugteren, P. Gao, L. Bottura, M. Dhallé, W. Goldacker, A. Kario, H. ten Kate, G. Kirby, E. Krooshoop *et al.*, “Measurement and numerical evaluation of AC losses in a ReBCO Roebel cable at 4.5 k,” *IEEE Trans. Appl. Supercond.*, vol. 26, no. 3, pp. 1–7, 2016.
- [23] A. Bossavit, “Numerical modelling of superconductors in three dimensions: a model and a finite element method,” *IEEE Trans. Magn.*, vol. 30, no. 5, pp. 3363–3366, 1994.
- [24] C. M. Elliott and Y. Kashima, “A finite-element analysis of critical-state models for type-II superconductivity in 3D,” *IMA journal of numerical analysis*, vol. 27, pp. 293–331, 2006.
- [25] Y. Kashima, “On the double critical-state model for type-II superconductivity in 3D,” *ESAIM: Mathematical Modelling and Numerical Analysis*, vol. 42, no. 3, pp. 333–374, 2008.
- [26] F. Grilli, R. Brambilla, F. Sirois, A. Stenvall, and S. Memiaghe, “Development of a three-dimensional finite-element model for high-temperature superconductors based on the H -formulation,” *Cryogenics*, vol. 53, pp. 142–147, 2013.
- [27] V. M. R. Zermeno and F. Grilli, “3D modeling and simulation of 2G HTS stacks and coils,” *Supercond. Sci. Technol.*, vol. 27, p. 044025, 2014.
- [28] G. Escamez, F. Sirois, V. Lahtinen, A. Stenvall, A. Badel, P. Tixador, B. Ramdane, G. Meunier, R. Perrin-Bit, and C. E. Bruzek, “3-d numerical modeling of ac losses in multifilamentary mgb 2 wires,” *IEEE Trans. Appl. Supercond.*, vol. 26, no. 3, pp. 1–7, 2016.
- [29] A. Stenvall, V. Lahtinen, and M. Lyly, “An H-formulation-based three-dimensional hysteresis loss modelling tool in a simulation including time varying applied field and transport current: the fundamental problem and its solution,” *Supercond. Sci. Technol.*, vol. 27, no. 10, p. 104004, 2014.
- [30] G. Lousberg, M. Ausloos, C. Geuzaine, P. Dular, P. Vanderbemden, and B. Vanderheyden, “Numerical simulation of the magnetization of high-temperature superconductors: a 3d finite element method using a single time-step iteration,” *Supercond. Sci. Technol.*, vol. 22, p. 055005, 2009.
- [31] J. F. Fagnard, M. Morita, S. Nariki, H. Teshima, H. Caps, B. Vanderheyden, and P. Vanderbemden, “Magnetic moment and local magnetic induction of superconducting/ferromagnetic structures subjected

- to crossed fields: experiments on gdbcu and modeling,” *Supercond. Sci. Technol.*, vol. 29, 2016.
- [32] A. M. Campbell, “A direct method for obtaining the critical state in two and three dimensions,” *Supercond. Sci. Technol.*, vol. 22, p. 034005, 2009.
- [33] F. Grilli, S. Stavrev, Y. Le Floch, M. Costa-Bouzo, E. Vinot, I. Klutsch, G. Meunier, P. Tixador, and B. Dutoit, “Finite-element method modeling of superconductors: from 2-D to 3-D,” *IEEE Trans. Appl. Supercond.*, vol. 15, no. 1, pp. 17–25, 2005.
- [34] V. Vlasko-Vlasov, A. Koshelev, A. Glatz, C. Phillips, U. Welp, and K. Kwok, “Flux cutting in high- T_c superconductors,” *Phys. Rev. B*, 2015.
- [35] V. Mishev, M. Zehetmayer, D. X. Fischer, M. Nakajima, and H. E. M. Eisterer, “Interaction of vortices in anisotropic superconductors with isotropic defects,” *Supercond. Sci. Technol.*, vol. 28, no. 102001, p. 9, 2015.
- [36] J. H. Durrell, A. R. Dennis, J. Jaroszynski, M. D. Ainslie, K. G. B. Palmer, Y. H. Shi, A. C. Campbell, J. Hull, M. Strasik, E. E. Hellstrom, and D. A. Cardwell, “A trapped field of 17.6t in melt-processed, bulk gd-ba-cu-o reinforced with shrink-fit steel,” *Supercond. Sci. Technol.*, vol. 27, p. 5, 2014.
- [37] M. Tinkham, *Introduction to superconductivity*. New York: McGraw-Hill, Inc., 1996.
- [38] Fujikura, <http://www.fujikura.com/solutions/superconductingwire/>.
- [39] D. C. Larbalestier, J. Jiang, U. P. Trociewitz, F. Kametami, C. Scheuerlein, M. Dalban-Canassy, M. Matras, P. Chen, N. C. craig, P. J. Lee, and E. E. Hellstrom, “Isotropic round-wire multifilament cuprate superconductor for generation of magnetic fields above 30 T,” *Nature Materials*, vol. 13, pp. 375–381, 2014.
- [40] K. Kim, K. R. Bhattarai, J. Y. Jang, Y. J. Hwang, K. Kim, S. Yoon, S. Lee, and S. Hahn, “Design and performance estimation of a 35 T 40 mm no-insulation all-REBCO user magnet,” *Supercond. Sci. Technol.*, vol. 30, no. 065008, 2017.
- [41] D. Park, J. Bascunan, P. Michael, J. Lee, S. Hahn, and Y. Iwasa, “Construction and test results of coils 2 and 3 of a 3-nested-coil 800-MHz REBCO insert for the MIT 1.3-GHz LTS/HTS NMR Magnet,” *IEEE Trans. Appl. Supercond.*, vol. 28, no. 4300205, 2018.

- [42] J. Liu and Y. Li, “High-Field Insert With Bi- and Y-Based Tapes for 25-T All-Superconducting Magnet,” *IEEE Trans. Appl. Supercond.*, vol. 26, no. 4602705, 2016.
- [43] “Hybrid magnet 45t,” <https://nationalmaglab.org/about/around-the-lab/meet-the-magnets/meet-the-45-tesla-hybrid-magnet>.
- [44] T. Yanamoto, M. Izumi, K. Umemoto, T. Oryu, Y. Murase, and M. Kawamura, “Load test of 3-MW HTS motor for ship propulsion,” *IEEE Trans. Appl. Supercond.*, vol. 27, no. 5204305, 2017.
- [45] B. Gamble, G. Snitchler, and T. MacDonald, “Full power test of a 36.5 MW HTS propulsion motor,” *IEEE Trans. Appl. Supercond.*, vol. 21, no. 3, pp. 1083–1088, 2011.
- [46] P. J. Masson, M. Breschi, T. Pascal, and C. Luongo, “Design of HTS axial flux motor for aircraft propulsion,” *IEEE Trans. Appl. Supercond.*, vol. 17, 2007.
- [47] P. J. Masson, K. Ratelle, P. A. Delobel, A. Lipardi, and C. Lorin, “Development of a 3D sizing model for all-superconducting machines for turbo-electric aircraft propulsion,” *IEEE Trans. Appl. Supercond.*, vol. 23, no. 3, p. 3600805, 2013.
- [48] J. Jeong, D. An, J. Hong, H. Kim, and Y. Jo, “Design of a 10-MW-Class HTS homopolar generator for wind turbines,” *IEEE Trans. Appl. Supercond.*, vol. 27, no. 5202804, 2017.
- [49] A. Abrahamsen, N. Mijatovic, E. Seiler, T. Zirngibl, C. Træholt, P. Nørgård, N. Pedersen, N. Andersen, and J. Østergaard, “Superconducting wind turbine generators,” *Supercond. Sci. Technol.*, vol. 23, p. 034019, 2010.
- [50] SUPRAPOWER-EU project. Superconducting light generator for large offshore wind turbines. <http://www.suprapower-fp7.eu/>.
- [51] S. Hellmann, M. Abplanalp, L. Hofstetter, and M. Noe, “Manufacturing of a 1-MVA-Class superconducting fault current limiting transformer with recovery-under-load capabilities,” *IEEE Trans. Appl. Supercond.*, vol. 27, no. 5500305, 2017.
- [52] N. Glasson, M. Staines, N. Allpress, M. Pannu, J. Tanchon, E. Pardo, R. Badcock, and R. Buckley, “Test results and conclusions from a 1 MVA superconducting transformer featuring 2G HTS roebel cable,” *IEEE Trans. Appl. Supercond.*, vol. 27, no. 5500205, 2017.
- [53] S. Schwenterly, B. McConnell, J. Demko, A. Fadnek, J. Hsu, F. List, M. Walker, D. Hazelton, F. Murray, J. Rice, C. Trautwein, X. Shi,

- R. Farrell, J. Bascunan, R. Hintz, S. Mehta, N. Aversa, J. Ebert, B. Bednar, D. Neder, A. McIlheran, P. Michel, J. Nemec, E. Pleva, A. Swenton, N. Swets, R. Longsworth, R. Longworth, R. Johnson, R. Jones, J. Nelson, R. Degeneff, and S. Salon, "Performance of a 1-MVA HTS demonstration transformer," *IEEE Trans. Appl. Supercond.*, vol. 9, pp. 680–684, 1999.
- [54] S. Mehta, "US effort on HTS power transformers," *Physica C*, vol. 471, pp. 1364–1366, 2011.
- [55] T. Pascal, A. Badel, G. Auran, and G. Pereira, "Superconducting fault current limiter for ship grid simulation and demonstration," *IEEE Trans. Appl. Supercond.*, vol. 27, no. 5601705, 2017.
- [56] Y. Xin, W. Gong, Y. Sun, J. Cui, H. Hong, X. Niu, H. Wang, L. Wang, Q. Li, J. Zhang, Z. Wei, L. Liu, H. Yang, and X. Zhu, "Factory and field tests of a 220 kV/300 MVA statured iron-core superconducting fault current limiter," *IEEE Trans. Appl. Supercond.*, vol. 23, no. 5602305, 2013.
- [57] A. Morandi, "State of the art of superconducting fault current limiters and their application to the electric power system," *Physica C*, vol. 484, pp. 242–247, 2013.
- [58] J. Šouc, F. Gömöry, and M. Vojenčiak, "Coated conductor arrangement for reduced AC losses in a resistive-type superconducting fault current limiter," *Supercond. Sci. Technol.*, vol. 25, p. 014005, 2012.
- [59] J. Kozak, M. Majka, T. Blazejczyk, and P. Berowski, "Tests of the 15-kV class coreless superconducting fault current limiter," *Supercond. Sci. Technol.*, vol. 26, no. 5600804, 2016.
- [60] E. Volkov, V. Vysotsky, and V. Firsov, "First russian long length HTS power cable," *Physica C-Superc. and its apl.*, vol. 482, pp. 87–91, 2012.
- [61] M. Yagi, J. Liu, S. Mukoyama, T. Mitsunashi, J. Teng, N. Hayakawa, W. Wang, A. Ishiyama, N. Amemiya, T. Hasegawa, T. Saitoh, O. Maruyama, and T. Ohkuma, "Experimental results of 275-kV 3-kA REBCO HTS power cable," *IEEE Trans. Appl. Supercond.*, vol. 25, no. 5401405, 2015.
- [62] J. Minervini, M. Parizh, and M. Schippers, "Recent advances in superconducting magnets for mri and hadron radiotherapy: an introduction to 'focus on superconducting magnets for hadron therapy and mri'," *Supercond. Sci. Technol.*, vol. 31, no. 030301, p. 4, 2018, <https://doi.org/10.1088/1361-6668/aaa826>.

- [63] “Cern,” <https://home.cern/about/accelerators>.
- [64] “Iter,” <https://www.iter.org/>.
- [65] V. Chepikov, N. Mineev, P. Degtyarenko, S. Lee, V. Petrykin, A. Ovcharov, A. Vasiliev, A. Kaul, V. Amelichev, A. Kamenev, A. Molodyk, and S. Samoilenkov, “Introduction of BaSnO₃ and BaZrO₃ artificial pinning centres into 2G HTS wires based on PLD GdBCO films. Phase I of the industrial R&D programme at SuperOx,” *Supercond. Sci. Technol.*, vol. 30, no. 124001, 2017.
- [66] Y. Iijima, Y. Adachi, S. Fujita, M. Igarashi, K. Kakimoto, M. Ohsugi, N. Nakamura, S. Hanyu, R. Kikutake, M. Daibo, M. Nagata, F. Tateno, and M. Itoh, “Development for mass production of homogeneous RE123 coated conductors by hot-wall PLD process on IBAD template technique,” *IEEE Trans. Appl. Supercond.*, vol. 25, no. 6604104, 2015.
- [67] J. Lee, B. Mean, T. Kim, Y. Kim, K. Cheon, T. Kim, D. Park, D. Song, H. Kim, W. Chung, H. Lee, and S. Moon, “Vision inspection methods for uniformity enhancement in long-length 2g hts wire production,” *IEEE Trans. Appl. Supercond.*, vol. 24, no. 6900505, 2014.
- [68] L. Rossi, X. Hu, F. Kametani, D. Abraimov, A. Polyanskii, J. Jaroszynski, and D. Larbalestier, “Sample and length-dependent variability of 77 and 4.2 K properties in nominally identical RE123 coated conductors,” *Supercond. Sci. Technol.*, vol. 29, no. 054006, 2016.
- [69] A. Xu, Y. Zhang, M. Gharahcheshmeh, L. Delgado, N. Khatri, Y. Liu, E. Galstyan, and V. Selvamanickam, “Relevant pinning for ab-plane J(c) enhancement of MOCVD REBCO coated conductors,” *IEEE Trans. Appl. Supercond.*, vol. 27, no. 4201005, 2017.
- [70] J. Lin, X. Liu, C. Cui, C. Bai, Y. Lu, F. Fan, Y. Guo, Z. Liu, and C. Cai, “A review of thickness-induced evolutions of microstructure and superconducting performance of REBa₂Cu₃O_{7-δ} coated conductor,” *Advances in Manufacturing.*, vol. 5, pp. 165–176, 2017.
- [71] S. Miura, Y. Tsuchiya, Y. Yoshida, Y. Ichino, S. Awaji, K. Matsumoto, A. Ibi, and T. Izumi, “Strong flux pinning at 4.2 K in SmBa₂Cu₃O_y coated conductors with BaHfO₃ nanorods controlled by low growth temperature,” *Supercond. Sci. Technol.*, vol. 30, no. 084009, 2017.
- [72] F. Grilli, V. M. R. Zermeno, E. Pardo, M. Vojenciak, J. Brand, A. Kario, and W. Goldacker, “Self-field effects and AC losses in pancake coils assembled from coated conductor roebel cables,” *IEEE Trans. Appl. Supercond.*, vol. 24, no. 3, p. 4801005, 2014.

- [73] H. Rogalla and P. H. Kes, Eds., *100 years of superconductivity*. New York: CRC Press, 2012.
- [74] S. Jin, R. C. Sherwood, R. B. van Dover, T. H. Tiefel, and D. W. Johnson, "Fabrication of dense $\text{Ba}_2\text{YCu}_3\text{O}_{7-\delta}$ superconductor wire by molten oxide processing," *Appl. Phys. Lett.*, vol. 51, 1987.
- [75] J. G. Bednorz and K. A. Müller, "Possible high-TC superconductivity in the BA-LA-CU-O system," *Physica B*, vol. 64, pp. 189–193, 1986, doi: 10.1007/BF01303701.
- [76] U. P. Trociewitz, J. Schwartz, K. Marken, H. Miao, M. Meinezs, and B. Czabaj, "Enhancement of texture and critical current density in $\text{Bi}_2\text{Sr}_2\text{Ca}_1\text{Cu}_2\text{O}_8$ superconducting tapes through magnetic field processing," *FL USA report*, vol. 297, 2005.
- [77] C. Michel, M. Hervieu, M. M. Borel, A. Grandin, F. Deslandes, J. Provost, and B. Raveau, "Superconductivity in the bi-sr-cu-o system," *Physics B*, vol. 68, p. 421, 1987.
- [78] K. Heine, J. Tenbrink, and M. Thoner, "High-field critical current densities in $\text{Bi}_2\text{Sr}_2\text{Ca}_1\text{Cu}_2\text{O}_{8+x}/\text{Ag}$ wires," *Appl. Phys. Lett.*, vol. 55, p. 2441, 1989.
- [79] J. Nagamatsu and N. Nakagawa, "Superconductivity at 39 K in magnesium diboride," *Nature*, vol. 410, pp. 63–64, 2009.
- [80] V. Braccini and A. Malagoli, "Improvement of magnetic field behavior of ex-situ processed magnesium diboride tapes," *IEEE Trans. Appl. Supercond.*, vol. 17, pp. 2766–2769, 2007.
- [81] B. Brunner, P. Kovac, M. Reissner, I. Husek, T. Melisek, and E. Pardo, "Critical current density and pinning behaviour of mono-core MgB_2 wires prepared by internal magnesium diffusion and in-situ powder-in-tube method," *Physica C-Superc. and its appl.*, vol. 505, pp. 39–43, 2014, doi: 10.1016/j.physc.2014.07.003.
- [82] J. Kováč, J. Šouc, P. Kováč, and I. Hušek, "Magnetization AC losses in MgB_2 wires made by IMD process," *Supercond. Sci. Technol.*, vol. 28, no. 1, p. 015013, 2015.
- [83] E. Brandt, "Susceptibility of superconductor disks and rings with and without flux creep," *Phys. Rev. B*, vol. 55, no. 21, p. 14513, 1997.
- [84] G. Blatter, M. V. Feigelman, V. B. Geshkenbein, A. I. Larkin, and V. M. Vinokur, "Vortices in high-temperature superconductors," *Rev. Mod. Phys.*, vol. 66, p. 1125, 1994.

- [85] C. Dekker, W. Eidelloth, and R. H. Koch, "Measurement of the exponent- μ in the low-temperature phase of $\text{YBa}_2\text{Cu}_3\text{O}_{7-\delta}$ films in a magnetic-field - direct evidence for a vortex-glass phase," *Phys. Rev. Lett.*, vol. 68, no. 22, pp. 3347–3350, 1992, doi: 10.1103/PhysRevLett.68.3347.
- [86] C. Bean, "Magnetization of high-field superconductors," *Rev. Mod. Phys.*, vol. 36, no. 1, pp. 31–38, 1964.
- [87] E. Zeldov, J. R. Clem, M. McElfresh, and M. Darwin, "Magnetization and transport currents in thin superconducting films," *Phys. Rev. B*, vol. 49, no. 14, pp. 9802–9822, 1994.
- [88] A. Bossavit, "Numerical modelling of superconductors in three dimensions: a model and a finite element method."
- [89] C. P. Bean, "Magnetization of hard superconductors," *Phys. Rev. Lett.*, vol. 8, no. 6, pp. 250–253, 1962.
- [90] F. Grilli, E. Pardo, A. Stenvall, D. Nguyen, W. Yuan, and F. Gomory, "Computation of losses in HTS under the action of varying magnetic fields and currents," *IEEE Trans. Appl. Supercond.*, vol. 24, no. 8200433, 2014.
- [91] M. R. Halse, "AC face field losses in a type II superconductor," *J. Phys. D: Appl. Phys.*, vol. 3, pp. 717–720, 1970.
- [92] E. Brandt and M. Indenbom, "Type-II-superconductor strip with current in a perpendicular magnetic field," *Phys. Rev. B*, vol. 48, no. 17, pp. 12893–12906, 1993.
- [93] Y. B. Kim, C. F. Hempstead, and A. R. Strnad, "Critical persistent currents in hard superconductors," *Phys. Rev. Lett.*, vol. 9, no. 7, pp. 306–309, 1962.
- [94] Y. B. KIM, C. F. Hempstead, and A. R. Strnad, "Magnetization and critical supercurrents," *Phys. Rev.*, vol. 129, no. 2, pp. 528–536, 1963, doi:https://doi.org/10.1103/PhysRev.129.528.
- [95] A. Badía-Majós and C. López, "Modelling current voltage characteristics of practical superconductors," *Supercond. Sci. Technol.*, vol. 28, no. 2, p. 024003, 2015.
- [96] V. Lahtinen, M. Lyly, A. Stenvall, and T. Tarhasaari, "Comparison of three eddy current formulations for superconductor hysteresis loss modelling," *Supercond. Sci. Technol.*, vol. 25, no. 11, p. 115001, 2012.

- [97] W. H. Press, S. A. Teukolsky, W. T. Vetterling, and B. P. Flannery, *Numerical Recipes in C*. New York: CAMBRIDGE UNIVERSITY PRESS, 1988.
- [98] A. Badía and C. López, “Critical state theory for nonparallel flux line lattices in type-II superconductors,” *Phys. Rev. Lett.*, vol. 87, no. 12, p. 127004, 2001.
- [99] A. Badía-Majós and C. López, “Electromagnetics close beyond the critical state: thermodynamic prospect,” *Supercond. Sci. Technol.*, vol. 25, no. 10, p. 104004, 2012.
- [100] E. Pardo, “Modeling of screening currents in coated conductor magnets containing up to 40000 turns,” *Supercond. Sci. Technol.*, vol. 29, no. 085004, p. 12pp, 2016, doi:10.1088/0953-2048/29/8/085004.
- [101] M. Kapolka, V. M. R. Zermeno, S. Zou, A. Morandi, P. L. Ribani, E. Pardo, and F. Grilli, “Three-dimensional modeling of the magnetization of superconducting rectangular-based bulks and tape stacks,” *IEEE Trans. Appl. Supercond.*, vol. 28, no. 8201206, 2018, doi: 10.1109/TASC.2018.2801322.
- [102] C++ tutorial, available online at: <http://www.cplusplus.com/doc/tutorial/variables/>.
- [103] OpenMP tutorial, available online at: <https://bisqwit.iki.fi/story/howto/openmp/>.
- [104] BoostMPI tutorial, available online at: <http://www.boost.org/doc/libs/1-64-0/doc/html/mpi.html>.
- [105] F. Grilli, “How filaments can reduce ac losses in hts coated conductors: a review,” *Supercond. Sci. Technol.*, vol. 29, no. 083002, p. 15, 2016, doi:10.1088/0953-2048/29/8/083002.
- [106] J. Šouc, F. Gömöry, and M. Vojenčiak, “Calibration free method for measurement of the ac magnetization loss,” *Supercond. Sci. Technol.*, vol. 18, no. 5, p. 592, 2005.
- [107] J. Kováč, J. Šouc, P. Kováč, I. Hušek, and F. Gömöry, “Experimental study of magnetization AC loss in MgB₂ wires and cables with non-magnetic sheath,” *Physica C*, vol. 495, pp. 182–186, 2013.
- [108] J. Kovac, J. Souc, and P. Kovac, “Experimental study of the ac magnetization loss in mgb2 superconducting wires at different temperatures,” *Physica C*, vol. 475, pp. 1–4, 2012, <https://doi.org/10.1016/j.physc.2012.01.006>.

- [109] D. Namburi, Y. Shi, K. Palmer, A. Dennis, J. Durrell, and D. Cardwell, "An improved top seeded infiltration growth method for the fabrication of YBaCuO bulk superconductors," *J. Euro. Cer. Soc.*, vol. 36, pp. 615–624, 2016.
- [110] M. D. Ainslie and F. Fujishiro, "Modelling of bulk superconductor magnetization," *Supercond. Sci. Technol.*, vol. 28, 2015.
- [111] J. Srpcic, D. Zhou, K. Huang, Y. Shi, A. Dennis, M. D. Ainslie, A. M. C. R. Bause, M. Boll, M. Filipenko, D. A. Cardwell, and J. H. Durrell, "Demagnetization study of pulse-field magnetized bulk superconductors," *IEEE Trans. Appl. Supercond.*, vol. 28, no. 6801305, 2018.
- [112] Multi-7U, available online at: <http://www.arepoc.sk/?p=29>.
- [113] D.-X. Chen and R. B. Goldfarb, "Kim model for magnetization of type-II superconductors," *J. Appl. Phys.*, vol. 66, no. 6, pp. 2489–2500, 1989.
- [114] W. Norris, "Calculation of hysteresis losses in hard superconductors carrying ac: isolated conductors and edges of thin sheets," *J. Phys. D: Appl. Phys.*, vol. 3, pp. 489–507, 1970.
- [115] J. Clem and A. Sanchez, "Hysteretic ac losses and susceptibility of thin superconducting disks," *Phys. Rev. B*, vol. 50, no. 13, p. 9355, 1994.
- [116] C. Navau, A. Sanchez, N. Del-Valle, and D. X. Chen, "Alternating current susceptibility calculations for thin-film superconductors with regions of different critical-current densities," *J. Appl. Phys.*, vol. 103, p. 113907, 2008.
- [117] J. W. Barrett and L. Prigozhin, "Electric field formulation for thin film magnetization problems," *Supercond. Sci. Technol.*, vol. 25, no. 10, p. 104002, 2012.
- [118] M. Solovyov, M. Vojenciak, and F. Gömör, "Magnetic field mapping above the superconducting tape with Ni-covered edges," *IEEE Trans. Appl. Supercond.*, vol. 19, no. 3, pp. 3049–3052, 2009.
- [119] J. Yoo, S. Lee, Y. Jung, J. Lee, D. Youm, R. K. Ko, and S. Oh, "Calculations of ac current losses and ac magnetic losses from the scanning hall probe measurements for a coated conductor," *Physica C-Superc. and its apl.*, vol. 468, pp. 160–168, 2008, doi: 10.1016/j.physc.2007.11.002.
- [120] C. Jooss, J. Albrecht, H. Kuhn, S. Leonhardt, and H. Kronmüller, "Magneto-optical studies of current distributions in high- T_c superconductors," *Rep. Prog. Phys.*, vol. 65, pp. 651–788, 2002.

- [121] Z. Jiang, M. Staines, N. J. Long, R. A. Badcock, C. Bumby, E. Talantsev, K. Hamilton, R. G. Buckley, and N. Amemiya, "The scaling of transport AC losses in Roebel cables with varying strand parameters," *Supercond. Sci. Technol.*, vol. 27, no. 7, p. 075007, 2014.
- [122] J. Šouc, E. Pardo, M. Vojenčiak, and F. Gömöry, "Theoretical and experimental study of ac loss in high temperature superconductor single pancake coils," *Supercond. Sci. Technol.*, vol. 22, p. 015006, 2009.
- [123] E. Pardo and F. Grilli, "Numerical simulations of the angular dependence of magnetization ac losses: coated conductors, roebel cables and double pancake coils," *Supercond. Sci. Technol.*, vol. 25, p. 014008, 2012.
- [124] M. Kapolka, J. Srpčić, D. Zhou, M. Ainslie, E. Pardo, and A. Dennis, "Demagnetization of cubic gd-ba-cu-o bulk superconductor by cross-fields: measurements and 3d modelling," *IEEE Trans. Appl. Supercond.*, vol. 28, no. 6801405, 2018, doi: 10.1109/TASC.2018.2808401.
- [125] A. Badia-Majos and C. Lopez, "Critical state model in superconducting parallelepipeds," *Appl. Phys. Lett.*, vol. 86, no. 202510, 2005, <https://doi.org/10.1063/1.1931829>.
- [126] E. Pardo and M. Kapolka, "3D magnetization currents, magnetization loop, and saturation field in superconducting rectangular prisms," *Supercond. Sci. Technol.*, vol. 30, no. 064007, p. 11, 2017.
- [127] "Proc. 5th int. workshop numer. model. hts, bologna, italy, jun. 15-17, 2016." available at <https://events.unibo.it/htsmodelling2016/>.
- [128] "Hts modelling workgroup," [Online]. Available: <http://www.htsmodelling.com/>.
- [129] F. Sirois and F. Grilli, "Potential and limits of numerical modelling for supporting the development of HTS devices," *Supercond. Sci. Technol.*, vol. 28, no. 043002, 2015, doi: 10.1088/0953-2048/28/4/043002.
- [130] F. Grilli, "Numerical modeling of hts applications," *IEEE Trans. Appl. Supercond.*, vol. 26, no. 0500408, 2016, doi:10.1109/TASC.2016.2520083.
- [131] F. Grilli, M. Costa Bouzo, Y. Yang, C. Beduz, and B. Dutoit, "Finite element method analysis of the coupling effect between superconducting filaments of different aspect ratio," *Supercond. Sci. Technol.*, vol. 16, no. 10, p. 1228, 2003.

- [132] S. Farinon, G. Iannone, P. Fabbriatore, and U. Gambardella, “2D and 3D numerical modeling of experimental magnetization cycles in disks and spheres,” *Supercond. Sci. Technol.*, vol. 27, no. 10, p. 104005, 2014.
- [133] E. Pardo, M. Kapolka, J. Kovac, J. Souc, F. Grilli, and A. Pique, “Three-dimensional modeling and measurement of coupling ac loss in soldered tapes and striated coated conductors,” *IEEE Trans. Appl. Supercond.*, vol. 26, no. 3, pp. 1–7, 2016.
- [134] A. Patel, S. C. Hopkins, and B. A. Glowacki, “Trapped fields up to 2 T in a 12 mm square stack of commercial superconducting tape using pulsed field magnetization,” *Supercond. Sci. Technol.*, vol. 26, no. 032001, 13, dOI: 10.1088/0953-2048/26/3/032001.
- [135] F. Grilli, R. Brambilla, and L. Martini, “Modeling high-temperature superconducting tapes by means of edge finite elements,” *IEEE Trans. Appl. Supercond.*, vol. 17, no. 2, pp. 3155–3158, 2007.
- [136] E. Pardo, J. Šouc, and J. Kováč, “AC loss in ReBCO pancake coils and stacks of them: modelling and measurement,” *Supercond. Sci. Technol.*, vol. 25, p. 035003, 2012.
- [137] R. Brambilla, F. Grilli, and L. Martini, “Development of an edge-element model for AC loss computation of high-temperature superconductors,” *Supercond. Sci. Technol.*, vol. 20, no. 1, pp. 16–24, 2007.
- [138] V. M. R. Zermeno, F. Grilli, and F. Sirois, “A full 3D time-dependent electromagnetic model for Roebel cables,” *Supercond. Sci. Technol.*, vol. 26, no. 5, p. 052001, 2013.
- [139] A. Cristofolini, M. Fabbri, A. Morandi, F. Negrini, and P. L. Ribani, “Current distribution in a composite superconducting system by means of an equivalent circuit model based on a smooth E-J equivalent material characteristic,” *Physica C-Superc. and its apl.*, vol. 372, no. PII S0921-4534(02)01123-1, pp. 1771–1776, 2002, dOI: 10.1016/S0921-4534(02)01123-1.
- [140] R. Albanese and G. Rubinacci, “Finite element methods for the solution of 3d eddy current problems,” *Advances in Im. Elec. Phys.*, vol. 102, pp. 1–86, 1997, [https://doi.org/10.1016/S1076-5670\(08\)70121-6](https://doi.org/10.1016/S1076-5670(08)70121-6).
- [141] D. Namburi, Y. Shi, K. Palmer, A. Dennis, J. Durrell, and D. Cardwell, “A novel, two-step top seeded infiltration and growth process for the fabrication of single grain, bulk (re)bco superconductors,” *Supercond. Sci. Technol.*, vol. 29, p. 11, 2016.

- [142] P. Vanderbemden, S. Dorbolo, N. Hari-Babu, A. Ntatsis, and D. C. A. Campbell, "Behavior of bulk melt-textured ybco single domains subjected to crossed magnetic fields," *IEEE Trans. Appl. Supercond.*, vol. 13, pp. 3746–3749, 2003.
- [143] P. Vanderbemden, Z. Hong, T. Coombs, M. Ausloos, N. Hari Babu, D. Cardwell, and A. Campbell, "Remagnetization of bulk high-temperature superconductors subjected to crossed and rotating magnetic fields," *Supercond. Sci. Technol.*, vol. 20, p. S174, 2007.
- [144] A. Campbell, M. Baghdadi, A. Pafel, D. Zhou, K. Y. Huang, Y. Shi, and T. Coombs, "Demagnetisation by crossed fields in superconductors," *Supercond. Sci. Technol.*, vol. 30, 2017.
- [145] M. Zhang and T. Coombs, "3D modeling of high- T_c superconductors by finite element software," *Supercond. Sci. Technol.*, vol. 25, p. 015009, 2012.
- [146] M. D. Ainslie, H. Fujishiro, T. Ujiie, J. Zou, A. R. Dennis, Y.-H. Shi, and D. A. Cardwell, "Modelling and comparison of trapped fields in (re)bcO bulk superconductors for activation using pulsed field magnetization," *Supercond. Sci. Technol.*, vol. 27, no. 065008, p. 9, 2014.
- [147] K. P. Thakur, A. Raj, E. H. Brandt, and P. Sastry, "Frequency dependent magnetization of superconductor strip," *Supercond. Sci. Technol.*, vol. 24, no. 095501, 2011, doi: 10.1088/0953-2048/24/9/095501.
- [148] —, "Frequency dependent magnetization of superconductor strip," *Supercond. Sci. Technol.*, vol. 24, no. 045006, 2011, doi: 10.1088/0953-2048/24/4/045006.
- [149] M. Sander and F. Grilli, "FEM-calculations on the frequency dependence of hysteretic losses in coated conductors," *J. Phys. Conference Series*, vol. 234, no. 022030, 2010, doi: 10.1088/1742-6596/234/2/022030.
- [150] J. Clem, "Flux-line-cutting losses in type-II superconductors," *Phys. Rev. B*, vol. 26, no. 5, p. 2463, 1982.
- [151] J. Clem, M. Weigand, J. H. Durrell, and A. M. Campbell, "Theory and experiment testing flux-line cutting physics," *Supercond. Sci. Technol.*, vol. 24, p. 062002, 2011.
- [152] J. Clem and A. Perez-Gonzalez, "Flux-line-cutting and flux-pinning losses in type-II superconductors in rotating magnetic fields," *Phys. Rev. B*, vol. 30, no. 9, p. 5041, 1984.

- [153] E. H. Brandt and G. P. Mikitik, “Unusual critical states in type-II superconductors,” *Phys. Rev. B*, vol. 76, no. 064526, 2007.
- [154] C. Romero-Salazar and F. Pérez-Rodríguez, “Elliptic flux-line-cutting critical-state model,” *Appl. Phys. Lett.*, vol. 83, p. 5256, 2003.
- [155] N. Ayai, S. Kobayashi, M. Kikuchi, T. Ishida, J. Fujikami, K. Yamazaki, S. Yamade, K. Tatamidani, K. Hayashi, K. Sato, H. Kitaguchi, H. Kumakura, K. Osamura, J. Shimoyama, H. Kamijyo, and Y. Fukumoto, “Progress in performance of DI-BSCCO family,” *Physica C-Superc. and its apl.*, vol. 468, no. 15-20, pp. 1747–1752, 2008.
- [156] A. Goyal, D. Norton, D. Kroeger, D. Christen, M. Paranthaman, E. Specht, J. Budai, Q. He, B. Saffian, F. List, D. Lee, E. Hatfield, P. Martin, C. Klabunde, J. Mathis, and C. Park, “Conductors with controlled grain boundaries: An approach to the next generation, high temperature superconducting wire,” vol. 12, no. 11, pp. 2924–2940, 1997.
- [157] I. Pallecchi, M. E. A. Malagoli, and M. Putti, “Application potential of Fe-based superconductors,” *Supercond. Sci. Technol.*, vol. 28, no. 114005, 2015.
- [158] W. Yi, Q. Wu, and L. Sun, “Superconductivities of pressurized iron pnictide superconductors,” *Acta Physica Sinica.*, vol. 66, no. 037402, 2017.
- [159] Y. Ma, Q. Ji, K. Hu, B. Gao, W. Li, G. Mu, and X. Xie, “Strong anisotropy effect in an iron-based superconductor $\text{CaFeO: 882CoO: 118AsF}$,” *Supercond. Sci. Technol.*, vol. 30, no. 074003, 2017.
- [160] J. Hecher, S. Ishida, D. Song, H. Ogino, A. Iyo, H. Eisaki, M. Nakajima, D. Kagerbauer, and M. Eisterer, “Direct observation of in-plane anisotropy of the superconducting critical current density in $\text{Ba}(\text{Fe}_{1-x}\text{Co}_x)_2\text{As}_2$ crystals,” *Phys. Rev. B*, vol. 97, no. 014511, 2018.
- [161] A high-temperature superconducting (HTS) wire critical current database. https://figshare.com/collections/A_high_temperature_superconducting_HTS_wire_critical_current_database/2861821.
- [162] E. Pardo, M. Vojenciak, F. Gomory, and J. Souc, “Low-magnetic-field dependence and anisotropy of the critical current density in coated conductors,” *Supercond. Sci. Technol.*, vol. 24, no. 065007, p. 10, 2011.
- [163] V. Zermeno, S. Quaiyum, and F. Grilli, “Open-source codes for computing the critical current of superconducting devices,” *IEEE Trans. Appl. Supercond.*, vol. 26, no. 4901607, 2016.

- [164] J. H. Durrell, S. H. Mennema, C. Jooss, G. Gibson, Z. H. Barber, H. W. Zandbergen, and J. E. Evetts, “Flux line lattice structure and behavior in antiphase boundary free vicinal YBa₂Cu₃O₇-delta thin films,” *J. Appl. Phys.*, vol. 93, pp. 9869–9874, 2003, doi: 10.1063/1.1576298.
- [165] M. Lao, J. Hecher, M. Sieger, P. Pahlke, M. B. R. Huhne, and M. Eisterer, “Planar current anisotropy and field dependence of J_c in coated conductors assessed by scanning hall probe microscopy,” *Supercond. Sci. Technol.*, vol. 30, no. 024004, p. 9, 2017.
- [166] C. Navau, N. Del-Valle, and A. Sanchez, “Macroscopic modeling of magnetization and levitation of hard type-II superconductors: The critical-state model,” *IEEE Trans. Appl. Supercond.*, vol. 23, no. 1, p. 8201023, 2013.
- [167] O. Ciftja, “Coulomb self-energy of a uniformly charged three-dimensional cube,” *Physics Letters A*, vol. 375, no. 3, pp. 766–767, 2011.
- [168] —, “Coulomb self-energy and electrostatic potential of a uniformly charged square in two dimensions,” *Physics Letters A*, vol. 374, no. 7, pp. 981–983, 2010.
- [169] E. Pardo and M. Kapolka, “3D computation of non-linear eddy currents: variational method and superconducting cubic bulk,” *J. Comput. Phys.*, vol. 344, pp. 339–363, 2017.